ANALYSIS OF THE DRAO 26 M TELESCOPE ROTATION MEASURE SYNTHESIS SURVEY OF GALACTIC POLARISED EMISSION

by

Alec James McInnes Thomson, B.Sc. (UTas)

Submitted in fulfilment of the requirements
for the Degree of Bachelor of Science with Honours

School of Physical Sciences
University of Tasmania
November, 2015

I declare that this thesis contains no material which has been accepted for a degree or diploma by the University or any other institution, except by way of background information and duly acknowledged in the thesis, and that, to the best of my knowledge and belief, this thesis contains no material previously published or written by another person, except where due acknowledgement is made in the text of the thesis.

Signed: _____
Alec James McInnes Thomson

Date: _____

Signed: _____
Alec James McInnes Thomson

Date: _____

ABSTRACT

This thesis presents an analysis of the DRAO 26 m rotation measure synthesis survey. This survey applies the process of rotation measure synthesis as formulated by Burn (1966) and Brentjens and de Bruyn (2005). Rotation measure synthesis allows the computation of Faraday depth, which in turn makes it possible to study the magneto-ionic medium via the Faraday effect. The survey provides data on both polarised emission and the resultant Faraday depth across the whole sky down to a declination of $\delta = -30°$. Analysis here is restricted to the North and South Galactic Poles. This avoids the depolarisation effects present near the Galactic plane and also allows the analysis of the vertical magnetic field at the position of the sun. The Faraday depth for each line of sight in the survey was taken to be the position peak of the Faraday spectrum and the associated polarised emission was taken to be the height of the peak.

The North Galactic Pole was analysed as a square region surrounding $b = 90°$. This area was a stereographic projection of the pole with an angular size of ~ 1600 deg^2. A similar region was computed for the South Galactic Pole, centred on $b = -90°$. The maps produced for these regions were 201×201 pixels in size and the resultant angular size for each pixel was $0.04\,\mathrm{deg}^2$.

Analysis of the Faraday depth in the North Galactic Pole has revealed that many of the high magnitude detections are spurious. This is indicated by a result of Sun et al. (2015) that errors in Faraday depth are associated with low polarised emission and are much higher than theoretically expected. This being the case, the best method of averaging Faraday depth was found to be a weighted average, where the weight used was the reciprocal of the error in Faraday depth squared for each line of sight. In the North Galactic Pole this method gave an average Faraday depth of $0.1 \pm 0.6\,\mathrm{rad\,m^{-2}}$. This is the same result as obtained in the extra-Galactic source survey by Mao et al. (2010), with $3\,\sigma$ confidence. The implication of this result is that there is no mean vertical magnetic field detected at the position of the sun. This result is incompatible with the theoretical dipole and quadrupole models of the Galactic magnetic field. A trend in the Faraday depth was, however, found in this survey. This trend corresponds with a magnetic field magnitude of $\sim 1\,\mu$G and implies a field reversal across the North Galactic Pole. Whether the reversal occurs in the horizontal or vertical field has not been determined. The magnitude of the magnetic field detected is dependent on the distance to the emission. As data on the distance to the emission was not analysed, assumptions on the distance had to be made in order to compute the magnetic field magnitudes.

Due to the declination range of the survey approximately half of the data for the South Galactic pole was not present. Additionally, strong scanning effects were identified and had to be excluded from analysis. The remaining Faraday depth data was associated with relatively high polarised emission; especially compared to the North Galactic Pole. Applying the same weighted average method as in the North Galactic Pole, an average Faraday depth of $-3.1 \pm 0.2\,\mathrm{rad\,m^{-2}}$ was found for the South Galactic Pole. This is in strong disagreement with the result found in extra-Galactic surveys. The implication of this result is that the Faraday depth detected in this survey is local. For the region of the pole that was available in this survey, this corresponds with a mean magnetic field magnitude of $\sim 1\,\mu$G. Any trends across the pole could not be analysed in this survey due to the lack of coverage below a declination of $\delta = -30°$.

Finally, the angular structure of both polarised emission and Faraday depth was quantified using the two-dimensional autocorrelation function. This was done in the South Galactic Pole, North Galactic Pole and surrounding Northern Galactic intermediate latitudes. The angular structure found was used to find a more reliable number of independent samples in the North and South Galactic Pole regions. This enabled the error analysis of both of these regions to be updated. Using these updated errors the average Faraday depth in the North and South Galactic Poles was found to be $0.1 \pm 0.5\,\mathrm{rad\,m^{-2}}$ and $-3.1 \pm 1\,\mathrm{rad\,m^{-2}}$ respectively.

Analysis in this project was conducted primarily with MathWorks MATLAB. Additionally, ANTF Miriad was used for data manipulation. ANTF Kvis and SAOImage Ds9 were also used for image analysis.

ACKNOWLEDGEMENTS

Firstly, thank you to my supervisor John Dickey. John introduced me to this project in 2014 and has guided me through with sound advice ever since.

Thank you to the GMIMS members Tom Landecker, Xiaohui Sun, Ettore Carretti and Maik Wolleben. They not only provided the data for this project, but have also provided invaluable advice and feedback over this year.

Thanks to my fellow occupants of the Honours office; Jonny Rogers, Tiege McCarthy, Lucas Hyland and Annabelle Austin. Without your moral and MATLAB support I wouldn't have made it through this long year.

I would like to thank the School of Physical Sciences for providing me with the Radio Astronomy Honours Scholarship. The financial support this provided went a long way during this year and allowed me to focus on my studies rather than my finances.

Last, but not least, I would like to thank my parents, Rachel and Douglas Thomson. The love, advice, cooking and proof-reading you gave me this year made the completion of this project possible.

TABLE OF CONTENTS

LIST OF TABLES

LIST OF FIGURES

Chapter 1

INTRODUCTION

1.1 Faraday Rotation

Michael Faraday was one of the great experimentalist scientists of the 19$^{\text{th}}$ Century. Despite a poor upbringing and subsequent lack of formal education, Faraday's work was some of the most impactful of his time; laying the experimental groundwork for theorists such as James Clerk Maxwell to develop the current understanding of electromagnetic (EM) phenomena. One of the many experiments conducted by Faraday was that on the interaction between light, materials, and electric and magnetic fields. In 1845 Faraday had already found that both light passing through certain materials, such as tourmaline crystal, and light reflecting from a surface, acted to polarise a given light source. He then wanted to determine what effect, if any, electric and magnetic fields might have on a polarised beam. A diagram of his experimental set-up is shown in Figure 1.1. Faraday found that a linearly polarised beam travelling parallel to a magnetic field rotated the angle of polarisation about the beam path (Johnson, 2008).

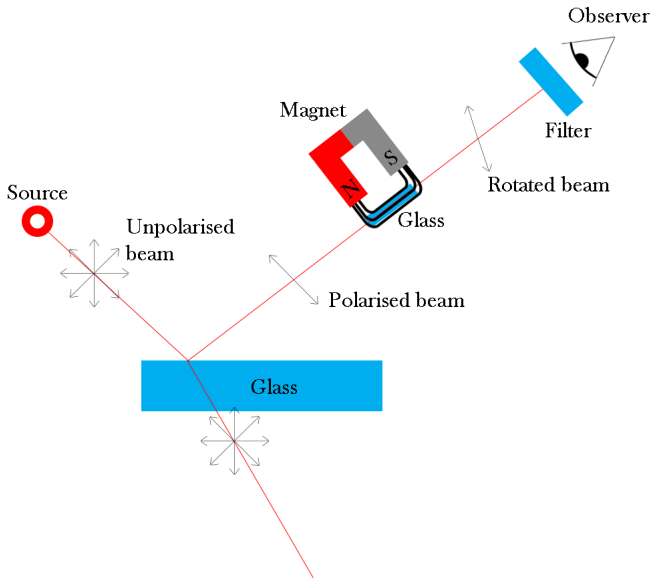

Figure 1.1: Faradays experimental set-up. Image credit to Gbur (2009).

We now have a theoretical understanding of this phenomenon by way of Maxwell's Equations and the result that light is an EM wave. Consider the E-field component of an EM wave linearly plane polarised and propagating in the $+z$ direction:

$$\mathbf{E}(z,t) = E_{0x}\cos(kz - \omega t)\hat{\mathbf{x}} \tag{1.1}$$

Here k is the wavenumber, ω the angular frequency of the wave and E_{0x} the amplitude of the E-field component. This can be decomposed into the superposition of two circularly polarised waves of opposite handedness and equal amplitude. Consider the superposition of a right circularly polarised (RCP) wave $\mathbf{E_R}$ and a left circularly polarised (LCP) wave $\mathbf{E_L}$:

$$\begin{aligned}
\mathbf{E_R} &= E_{0c}\left(\cos\left(kz-\omega t\right)\hat{\mathbf{x}} + \sin\left(kz-\omega t\right)\hat{\mathbf{y}}\right) \\
\mathbf{E_L} &= E_{0c}\left(\cos\left(kz-\omega t\right)\hat{\mathbf{x}} - \sin\left(kz-\omega t\right)\hat{\mathbf{y}}\right) \\
\mathbf{E_R}+\mathbf{E_L} &= E_{0c}(\cos\left(kz-\omega t\right)\hat{\mathbf{x}} + \sin\left(kz-\omega t\right)\hat{\mathbf{y}} \ldots \\
&\quad + \cos\left(kz-\omega t\right)\hat{\mathbf{x}} - \sin\left(kz-\omega t\right)\hat{\mathbf{y}}) \\
&= 2E_{0c}\cos\left(kz-\omega t\right)\hat{\mathbf{x}}
\end{aligned}$$

Now if we put $2E_{0c} = E_{0x}$, we get:

$$\mathbf{E}(z,t) = \mathbf{E_R} + \mathbf{E_L} \tag{1.2}$$

Here the wavenumber for each circularly polarised wave was taken to have the same value and this resulted in a total electric field wave ($\mathbf{E}(z,t)$) oscillating in the $\hat{\mathbf{x}}$ direction. If, however, there is a phase difference between $\mathbf{E_R}$ and $\mathbf{E_L}$ the direction that the resultant wave oscillates in will change. This is because the $\hat{\mathbf{y}}$ terms will no longer cancel. It is important, then, to consider what will cause a phase difference between the circularly polarised waves.

In an astrophysical circumstance we need only consider the effect of a magneto-ionic medium on a polarised wave; i.e. the rotating effect of electron density and a magnetic field.

Following the derivation outlined by both Harwit (2006) and Kraus (1966); consider an electron moving at velocity $\mathbf{v}$, perpendicular to some magnetic field vector $\mathbf{B}$. The force on the electron from the field is given by the Lorenz force:

$$\mathbf{F} = e(\mathbf{v}\times\mathbf{B}) \tag{1.3}$$

Where e is the charge on the electron. Consider also that the electron is interacting with a circularly polarised EM wave. The E-field term of the wave, thus, will also influence the motion of the electron. As such, the electron will gyrate by obeying the following force equation:

$$e\mathbf{E} \pm eB\omega\mathbf{r} = -m_e\omega^2\mathbf{r} \tag{1.4}$$

Where $\mathbf{E}$ is the E-field vector, ω is the angular frequency of the EM wave, $B = ||\mathbf{B}||$, m_e is the mass of the electron and $\mathbf{r}$ is the direction of propagation of the wave. Note that the sign of the second term on the right hand side is determined by the handedness of the polarisation; RCP gives a negative sign and vice versa. Rearranging Equation 1.4 for $\mathbf{r}$:

$$\mathbf{r} = -\frac{e}{m_e}\frac{\mathbf{E}}{\left(\omega^2 \pm \frac{eB\omega}{m_e}\right)} \tag{1.5}$$

This relationship describes the displacement of electrons due to the gyrations. Such a displacement gives rise to a polarisation field. Where $\mathbf{P}$ is the electric dipole moment per volume:

$$\mathbf{P} \equiv \frac{(\varepsilon - 1)\mathbf{E}}{4\pi} = n_e e \mathbf{r} \tag{1.6}$$

Substituting for $\mathbf{r}$ from Equation 1.5 and solving for the dielectric constant ε yields:

$$\varepsilon = 1 - \frac{4\pi n_e e^2}{m_e \omega \left(\omega \pm \frac{eB\omega}{m_e}\right)} \tag{1.7}$$

To simplify, define the plasma frequency ω_0 and the gyrofrequency ω_g:

$$\omega_0 = e\sqrt{\frac{n_e}{\varepsilon_0 m_e}} \tag{1.8}$$

$$\omega_g = \frac{e}{m_e} B \tag{1.9}$$

Where ε_0 is the permittivity of free space. This gives the dielectric constant as:

$$\varepsilon = 1 - \frac{4\pi\varepsilon_0\omega_0^2}{m_e\omega\left(\omega \pm \omega_g\right)} \tag{1.10}$$

Now consider the refractive index of medium:

$$n \equiv \frac{c}{v} = \sqrt{\frac{\varepsilon}{\varepsilon_0}} \tag{1.11}$$

Where v is the magnitude of the phase velocity in the medium and c is the speed of light in a vacuum. Thus, we have the relationship:

$$v \propto \varepsilon^{-\frac{1}{2}} \tag{1.12}$$

Now, since RCP will select the negative sign and LCP the positive, there will be a speed lag between the two waves. Thus, the two waves will now no longer be in phase. It is this phase lag that causes the Faraday rotation effect. To quantitatively appreciate this consider an RCP and an LCP wave traveling through a magneto-ionic medium, where the direction of propagation is parallel to the B-field. In this case the wavenumber is given by (from Kraus (1966)):

$$k \equiv \frac{2\pi}{\lambda} = \omega\sqrt{\mu_0\left(\left(1 + \frac{\omega_0^2}{\omega_g^2 - \omega^2}\right)\varepsilon_0 \pm \frac{-i\omega_0^2\omega_g\varepsilon_0}{\omega\left(\omega_g^2 - \omega^2\right)}\right)} \tag{1.13}$$

The expressions in parenthesis arise from expressions of the general tensor form of the permittivity in a magneto-ionic medium. The complete general tensor forms are given in Kraus (1966).

The amount of angular rotation experienced by the RCP wave χ along an element path length dr is given by:

$$d\chi_R = k^- dr \tag{1.14}$$

Where k^- selects the negative term from the wavenumber expression. Similarly, for the other LCP we have:

$$d\chi_L = k^+ dr \tag{1.15}$$

Consider now the superposition of these waves, giving a resultant linearly polarised wave. In this frame the amount of angular rotation χ is now the rotation angle of the linear wave; i.e. the amount of rotation that has occurred since emission along the path length. Thus, the net rotation angle is given by:

$$d\chi = \frac{k^- - k^+}{2} dr \tag{1.16}$$

To simplify it is assumed that $\omega \gg \omega_g$ and $\omega \gg \omega_0$. This approximation gives:

$$d\chi = \frac{n_e e^3 \lambda^2}{4\pi^2 c^4 m_e^2} \mathbf{B} \cdot d\mathbf{r} \tag{1.17}$$

Integrating from the origin, i.e. the observer's position at $r = 0$, out to some distance $r = d$ gives:

$$\chi = \frac{e^3 \lambda^2}{4\pi^2 c^4 m_e^2} \int_0^d n_e \mathbf{B} \cdot d\mathbf{r} \tag{1.18}$$

The Faraday depth (ϕ) is now defined so as to eliminate the wavelength dependence on the rotation:

$$\phi = \frac{\chi}{\lambda^2} \tag{1.19}$$

Finally, evaluating n_e in cm^{-3}, $\mathbf{B}$ in μG, and $\mathbf{r}$ in pc gives:

$$\phi(\mathbf{r}) = 0.81 \int_0^d n_e \mathbf{B} \cdot d\mathbf{r} \,\mathrm{rad\,m}^{-2} \tag{1.20}$$

Thus, by measuring how the polarisation angle changes with wavelength and by substituting a model for the electron density, the magnetic field along the line of sight can be calculated. Techniques using this phenomenon have allowed the accurate measurement of cosmic magnetic fields; a topic which still has a great deal of problems to solve.

1.2 Rotation Measure Synthesis

The mechanism for non-thermal emission from a magneto-ionic medium is synchrotron emission. That is, the radiation produced by relativistic particles orbiting about a magnetic field. Such radiation is expected to be highly polarised. For synchrotron radiation produced in a uniformly magnetised plasma with isotropic velocity distributions, the degree of polarisation is given by Burn (1966):

$$||p|| = \frac{3\gamma + 3}{3\gamma + 7} \tag{1.21}$$

Where γ is the spectral index of the relativistic electron energy distribution. From this understanding alone one would not expect any wavelength dependence on the polarised fraction observed. Observations, however, found that the polarisation fraction usually decreased strongly with increasing wavelength; this effect is known as depolarisation. Burn (1966) tackled the problem of depolarisation from a number of possible sources. Most notable was his study of depolarisation by Faraday rotation.

The rotation measure (RM) of the magneto-ionic medium is defined as the change of observed polarisation angle with wavelength squared:

$$RM = \frac{d\chi(\lambda^2)}{d\lambda^2} \tag{1.22}$$

Where the observed angle of polarisation is:

$$\chi = \frac{1}{2}\arctan\left(\frac{U}{Q}\right) \tag{1.23}$$

Where U and Q are the observed surface brightnesses for the respective linear Stokes parameters, as defined in Kraus (1966). For some small amount of rotation, RM can be used to estimate the Faraday depth, ϕ. It is worth noting that in many texts these two terms are often interchangeably; here the definitions as used by Brentjens and de Bruyn (2005) will be used. These definitions are given by Equation 1.22 and Equation 1.19 for RM and ϕ, respectively.

The problem of depolarisation arises from two primary sources, both of which are discussed by Burn (1966). Bandwidth depolarisation is the result in an observation of decreased polarisation across different wavelengths. With respect to Faraday rotation, it occurs when the rotation effect is strong enough to create an ambiguity in the measurement of χ of $n\pi$ radians for a given wavelength ($n = 0, 1, 2, 3, \dots$). Beam depolarisation occurs when polarised fluctuations are present within an observed beam. If radiation is emitted from different areas within an unresolved region with opposing linear polarisation, the observed emission will be depolarised. If either case occurs the method of computing rotation measure as shown above becomes unreliable.

Burn showed there was a way to overcome this problem. He introduced the Faraday dispersion function $F(\phi)$, which is the flux of linearly polarised radiation for a given Faraday depth. This function is defined by the Fourier transform:

$$P(\lambda^2) = \int_{-\infty}^{+\infty} F(\phi) e^{2i\phi\lambda^2} d\phi \tag{1.24}$$

Where P is the complex surface brightness, sampled in intervals of λ^2, written in terms of the Stokes parameter I:

$$P = ||p||Ie^{2i\chi} \tag{1.25}$$

Alternatively we can write:

$$P = pI = Q + iU \tag{1.26}$$

Note that the polarised flux density P should not be confused with the polarisation field $\mathbf{P}$ from Section 1. To find the Faraday dispersion function one might naively just invert the Fourier transform:

$$F(\phi) = \frac{1}{\pi} \int_{-\infty}^{+\infty} P(\lambda^2) e^{-2i\phi\lambda^2} d\lambda^2 \tag{1.27}$$

The calculation of this function is known as rotation measure synthesis. This technique allows the problem of depolarisation to be reversed and thus studies can be conducted of an observed magneto-ionic medium. A problem with this becomes immediately apparent. It is not possible to sample every single possible wavelength continuously and it is nonsensical to consider negative wavelengths. Burn attempted to address this problem by way of a simplifying assumption. If there is only a single source along the line of sight with no intrinsic Faraday rotation, then the measured angle of polarisation is given by:

$$\chi = \chi_0 + \phi\lambda^2 \tag{1.28}$$

Where χ_0 is the initial angle of polarisation at the source and is assumed to be constant under these conditions. Burn argued that under this regime the Equation 1.27 simplifies to:

$$F(\phi) = \frac{2}{\pi} \int_{0}^{+\infty} Re\left\{ P(\lambda^2) e^{-2i\phi\lambda^2} \right\} d\lambda^2 \tag{1.29}$$

This function still does not address the problem of observable bandwidths. At the time of writing, Burn concluded that insufficient data existed to begin to attempt this technique. The other problem here is that assuming only a single source along the line of sight and that the source has no intrinsic Faraday rotation is not generally true for a large number of observations.

Brentjens and de Bruyn (2005) addressed both of these concerns building on the work of Burn (1966) and provided a framework for experimentalists to make use of this technique. They defined the weight function $W(\lambda^2)$. This function has a non-zero value for all wavelengths observed in a given experiment, but is zero for all other values including the range of $\lambda^2 < 0$. The observed polarised flux density $\widetilde{P}$ is then given by:

$$\widetilde{P}(\lambda^2) = W(\lambda^2)P(\lambda^2) \tag{1.30}$$

Substituting this into the definition of the Faraday dispersion function, Equation 1.24, yields:

$$\widetilde{P}(\lambda^2) = W(\lambda^2)\int_{-\infty}^{+\infty} F(\phi)e^{2i\phi\lambda^2}d\phi \tag{1.31}$$

This equation can now be parameterised by substituting $\lambda^2 = \pi u$, for some arbitrary u, which gives:

$$\widetilde{P}(\pi u) = W(\pi u)\int_{-\infty}^{+\infty} F(\phi)e^{2\phi i\pi u}d\phi \tag{1.32}$$

Brentjens and de Bruyn now define the Rotation Measure Transfer Function (RMTF), $R(\phi)$ as:

$$R(\phi) = \frac{\int_{-\infty}^{+\infty} W(\pi u)e^{-2\phi i\pi u}du}{\int_{-\infty}^{+\infty} W(\pi u)du} \tag{1.33}$$

This function is normalised by setting $R(0) = 1$.

Hence, inverting (see Equation A.2) the definition of the RMTF, Equation 1.33, will yield:

$$W(\pi u) = \left(\int_{-\infty}^{+\infty} W(\pi u)du\right)\int_{-\infty}^{+\infty} R(\phi)e^{2\phi i\pi u}d\phi \tag{1.34}$$

Combining Equation 1.34 with Equation 1.32 gives:

$$\widetilde{P}(\pi u) = \int_{-\infty}^{+\infty} W(\pi u)du\int_{-\infty}^{+\infty} R(\phi)e^{2\phi i\pi u}d\phi\int_{-\infty}^{+\infty} F(\phi)e^{2\phi i\pi u}d\phi \tag{1.35}$$

Now applying the second from the Convolution Theorem (Equation A.5) gives:

$$F(\phi) * R(\phi) = \frac{\int_{-\infty}^{+\infty} \widetilde{P}(\pi u)e^{2\phi i\pi u}du}{\int_{-\infty}^{+\infty} W(\pi u)du} \tag{1.36}$$

Now substituting $\lambda^2 = \pi u$ back into Equation 1.36 yields:

$$\widetilde{F}(\phi) = F(\phi) * R(\phi) = K\int_{-\infty}^{+\infty} \widetilde{P}(\lambda^2)e^{-2i\phi\lambda^2}d\lambda^2 \tag{1.37}$$

$$R(\phi) = K \int_{-\infty}^{+\infty} W(\lambda^2) e^{-2i\phi\lambda^2} d\lambda^2 \tag{1.38}$$

Where

$$K = \left(\int_{-\infty}^{+\infty} W(\lambda^2) d\lambda^2 \right)^{-1} \tag{1.39}$$

$\widetilde{F}(\phi)$ can be thought of as the approximate reconstruction of $F(\phi)$ for some observed bandwidth. Strictly, though, $\widetilde{F}(\phi)$ is the convolution of $F(\phi)$ with the RMTF after filtering though the weight function. There are two resulting factors from this which bear significant weight for observational work:

1. The better the λ^2 space sampling the more accurate the reconstruction of $F(\phi)$ will be. A poorly sampled λ^2 space will result in spurious flux appearing in the measured $\widetilde{F}(\phi)$. This is a systematic error, however, and with correct modelling of the RMTF cleaning algorithms can discard spurious flux from observed data.

2. The more broad the range of λ^2, the higher the resolution will be in Faraday depth space.

The action of Equations 1.37, 1.38 and 1.39 is to take the polarisation vector at each sampled λ^2 and derotate the vectors back to same angle as at $\lambda^2 = 0$. This essentially 'undoes' the problem of depolarisation and removes the ambiguity of rotations about $n\pi$ radians.

Rotating back to $\lambda^2 = 0$ does not have to be the general case. In fact, Brentjens and de Bruyn argued that it is not optimal to do so. They showed by using one of their own data sets that using $\lambda^2 = 0$ resulted in a rapidly varying RMTF which in turn made measurement of polarisation angles difficult. To derotate to some arbitrary wavelength λ_0 the dispersion function becomes:

$$\widetilde{F}(\phi) = K \int_{-\infty}^{+\infty} \widetilde{P}(\lambda^2) e^{-2i\phi(\lambda^2 - \lambda_0^2)} d\lambda^2 \tag{1.40}$$

$$R(\phi) = K \int_{-\infty}^{+\infty} W(\lambda^2) e^{-2i\phi(\lambda^2 - \lambda_0^2)} d\lambda^2 \tag{1.41}$$

The question remains then: what is the optimal value to choose for λ_0? Brentjens and de Bruyn argued that in the ideal case the peak of the RMTF should be parallel to the polarisation vector at $\lambda = \lambda_0$. Doing this results in variations of the imaginary component of the RMTF being reduced to as close to zero as possible. It is these variations which cause spurious flux to appear in the reconstructed function $\widetilde{F}(\phi)$, so reducing them is highly desirable. To accomplish this, Brentjens

and de Bruyn set the derivative of the imaginary component of the RMTF to zero at $\phi = 0$:

$$\begin{aligned}
\frac{\partial Im(R(\phi))}{\partial \phi}\Big|_{\phi=0} &= 0 \\
-K\frac{\partial}{\partial \phi}\int_{-\infty}^{+\infty} W(\lambda^2)\sin\left(-2\phi(\lambda^2-\lambda_0^2)\right)d\lambda^2\Big|_{\phi=0} &= 0 \\
-K\int_{-\infty}^{+\infty} W(\lambda^2)2(\lambda^2-\lambda_0^2)\cos\left(-2\phi(\lambda^2-\lambda_0^2)\right)d\lambda^2\Big|_{\phi=0} &= 0 \\
\int_{-\infty}^{+\infty} W(\lambda^2)(\lambda^2-\lambda_0^2)d\lambda^2 &= 0
\end{aligned}$$

$$\therefore \lambda_0^2 = \frac{\int_{-\infty}^{+\infty} W(\lambda^2)(\lambda^2)d\lambda^2}{\int_{-\infty}^{+\infty} W(\lambda^2)d\lambda^2} \tag{1.42}$$

The result is that λ_0^2 should be the weighted average of observed λ^2 space.

Practically, most telescopes are not set up to observe λ^2 space, rather they observe in frequency bands. Brentjens and de Bruyn addressed the typical case where a correlator will have channels of equal bandwidth $\Delta\nu$, centred around frequency ν_c for each channel. For the sake of simplicity they assumed a 'top hat' bandpass for each channel (see Figure 1.2).

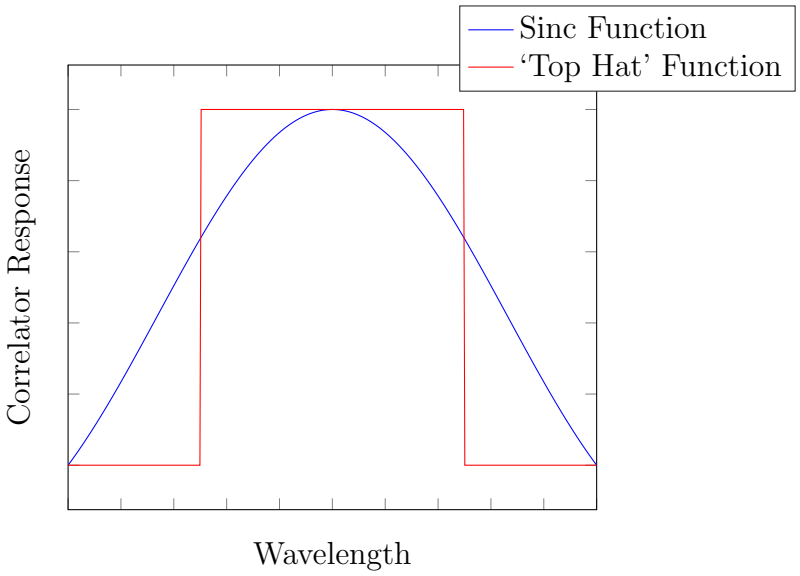

Figure 1.2: Response of a correlator with a 'Top Hat' function and a more realistic Sinc function.

Under this assumption we have, for each channel:

$$\lambda_c^2 \approx \frac{c^2}{\nu_c^2}\left(1+\frac{3}{4}\left(\frac{\Delta\nu}{\nu_c}\right)^2\right) \tag{1.43}$$

And

$$\Delta\lambda^2 \approx \frac{2c^2\Delta\nu^2}{\nu_c^3}\left(1+\frac{1}{2}\left(\frac{\Delta\nu}{\nu_c}\right)^2\right) \tag{1.44}$$

Brentjens and de Bruyn noted that a bandpass in general will not strictly be a 'Top Hat', but instead sinc, Hanning or Kaiser-Bessel function (see Figure 1.2). The difference between the more general case and the 'Top Hat' becomes insignificant if we assume $\Delta\nu \ll \nu_c$, i.e. a narrow bandpass. Finally, if we have $\phi\Delta\lambda^2 \ll 1$, the Fourier integrals in Equations 1.40 and 1.41 can be approximated by:

$$\widetilde{F}(\phi) \approx K\sum_{i=1}^{N}\widetilde{P}_i e^{-2i\phi(\lambda_i^2-\lambda_0^2)} \tag{1.45}$$

$$R(\phi) \approx K\sum_{i=1}^{N} w_i e^{-2i\phi(\lambda_i^2-\lambda_0^2)} \tag{1.46}$$

$$K = \left(\sum_{i=1}^{N} w_i\right)^{-1} \tag{1.47}$$

Where N is the total number of channels, $\lambda_i = \lambda_c$ for channel i, $\widetilde{P}_i = \widetilde{P}(\lambda_i^2) = w_i P(\lambda_i^2)$ and $w_i = W(\lambda_i^2)$. Using these equations, rotation measure synthesis can be applied to observational data. In order to apply rotation measure synthesis observations must be made in the radio spectrum, using a correlator with a high frequency resolution of linear polarised emissions (stokes Q and U), contiguously across as broad a bandwidth as possible. Using, then, the approximate Fourier transforms above the flux density for each value of Faraday depth, within the range determined by the RMTF. Thus, Faraday depth can be found in circumstances where depolarisation made simply using RM impossible.

1.3 B-field Calculation

Once a value for Faraday depth is found using the rotation measure synthesis technique consideration can be made of the magnetic field causing the rotation effect. Mao et al. (2010) provided a concise method of determining a magnetic field from rotation measure. Again, consider Equation 1.20. To solve for the magnetic field term, B, the electron density term, n_e, must be known. There

are two methods for evaluating this term; dispersion measure (DM) and emission measure (EM). Dispersion measure is defined as the integral along the line of sight of electron density:

$$DM = \int_0^d n_e dr = \langle n_e \rangle d \tag{1.48}$$

Where $\langle n_e \rangle$ is the average electron density along the line of sight and d is the distance out along the line of sight. Dispersion measure is determined by observing the time delay from pulsar emissions across a finite bandwidth. Emissions of higher frequency emitted from a pulsar interact less with an ionic medium relative to photons of a lower frequency. Thus, a time delay occurs between pulses in different observed frequencies. Dispersion measure can then be calculated by:

$$DM = \frac{t_2 - t_1}{\left(\frac{1}{\nu_1^2} - \frac{1}{\nu_2^2}\right)} \,\mathrm{pc\,cm^{-3}} \tag{1.49}$$

Where $t_2 - t_1$ is the time delay in lots of 4.15 ms between frequencies ν_1 and ν_2 in GHz (Germany et al., 2015). Pulsars in the Milky Way tend to cluster in the plane of the disk (see Figure 1.3) making dispersion measure useful for n_e near the Galactic plane.

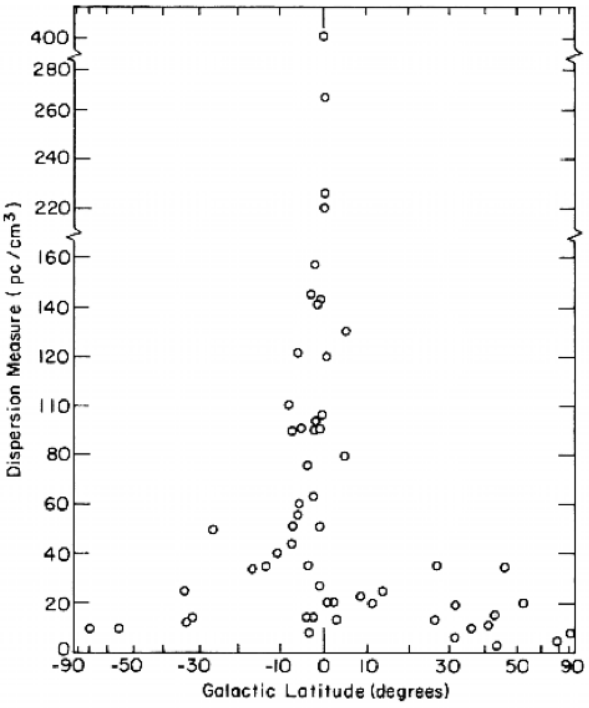

Figure 1.3: Galactic latitude of 63 pulsars known by 1972 (Harwit, 2006).

Emission measure is defined similarly to dispersion measure, but instead gives the line integral of n_e^2 along the line of sight:

$$EM = \int_0^d n_e^2 dr = \langle n_e^2 \rangle d \tag{1.50}$$

Where $\langle n_e^2 \rangle$ is the average squared electron density along the line of sight. Reynolds (1991) showed that emission measure can be calculated using observations of the Balmer series line of hydrogen $H\alpha$. Reynolds gave:

$$EM = 2.75 T^{0.9} I_\alpha \,\mathrm{pc\,cm^{-6}} \tag{1.51}$$

Where T is the electron temperature in 10^4 K and I_α is the intensity of $H\alpha$ emission in Rayleighs. There are two major surveys of $H\alpha$ emission currently in use: Wisconsin H-Alpha Mapper (WHAM) and The Southern H-Alpha Sky Survey Atlas (SHASSA). WHAM is a whole sky survey of $H\alpha$ emission down to a declination of $\delta = -30°$ and maps emission within $\sim \pm 100\,\mathrm{km\,s^{-1}}$ of the local standard of rest (LSR). Similarly, SHASSA provides a whole sky map up to a declination of $\delta = +15°$ and thus provides coverage for the Southern Hemisphere component missing from the WHAM survey.

In order to determine Galactic magnetic field values Mao et al. (2010) defined the following heliocentric coordinate system (See Figure 4). Centred on the solar position the z-axis is perpendicular to the Galactic plane, with positive z pointing to the North Galactic pole ($b = 90°$). The x- and y-axes lie in the Galactic plane and define a right handed coordinate system with the positive x-axis pointing to the Galactic centre (GC) (See Figure 1.4). The magnetic field as determined from Faraday rotation lies parallel to the line sight, thus:

$$\mathbf{B} = B_x \hat{\mathbf{x}} + B_y \hat{\mathbf{y}} + B_z \hat{\mathbf{z}} \tag{1.52}$$

The horizontal component of the field B_H is the hypotenuse of the right angled triangle with sides B_x and B_y. The angle from the x-axis towards y is l_0, hence:

$$\mathbf{B} = B_H \cos l_0 \hat{\mathbf{x}} + B_H \sin l_0 \hat{\mathbf{y}} + B_z \hat{\mathbf{z}} \tag{1.53}$$

Mao et al. then assumed that the distribution of thermal electrons decreases exponentially from the disk:

$$n_e(z) = n_{e0} e^{-\frac{|z|}{H_0}} \tag{1.54}$$

Where n_{e0} is the average electron density in the disk and H_0 is the scale height of the electron distribution. They noted, however, that the value of the scale height is yet to be agreed upon. Mao et al. investigated the magnetic field at high Galactic latitudes. As such they considered l_0, B_z and B_H to be constant for regions near

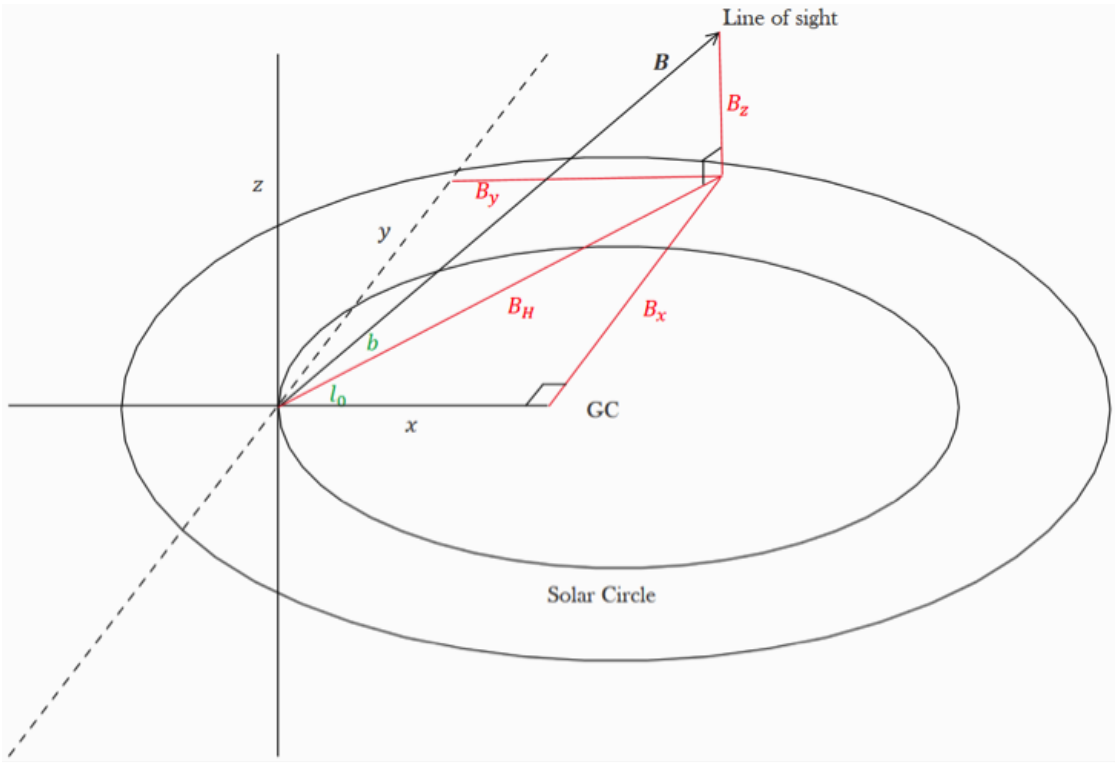

Figure 1.4: Heliocentric Galactic coordinate system.

the North and South Galactic poles. Under these assumptions substituting these two equations into Equation 1.20 yields:

$$\phi(l,b) = 0.81 n_{e0} H_0 \left(a B_z - \frac{B_H \cos(l - l_0)}{\tan|b|} \right) \tag{1.55}$$

Where $a = +1$ for the South Galactic pole and $a = -1$ for the North Galactic pole. Now, by averaging Faraday depth around all values of l in a region near each pole eliminates the contribution from the horizontal term ($\int_0^{2\pi} \cos(l - l_0) dl = 0, \forall l_0 \in \mathbb{R}$). Thus, the vertical component of the magnetic field can be found:

$$B_z \approx \frac{\langle \phi \rangle}{0.81 a n_{e0} H_0} \tag{1.56}$$

Where $\langle \phi \rangle$ is the Faraday depth averaged around l. Mao et al. then suggested that the vertical component term can be found by performing a least-squares fit of the model given by the equation for $\phi(l,b)$ to measured ϕ and B_z values.

Investigation of high latitude magnetic fields has two primary advantages. Firstly it allows the assumptions made by Mao et al. (2010) to apply and thus simplifies the modelling of the field. Secondly, it allows a great deal of testing to be done of theoretical models of the Milky Way's magnetic field.

1.4 Theoretical B-Field Structure in the Milky Way

The structure and scale of magnetic fields in the Milky Way are yet to be conclusively determined. Whilst work has begun on observations of the Galactic magnetic field (Mao et al., 2010, 2012) more observations and modelling are required before a decisive model of the Galactic magnetic field is determined. In the absence of such observations, however, theoretical models can be derived in combination with observations of magnetic fields in galaxies other than the Milky Way.

Haverkorn and Heesen (2012) present a concise summary of both the observed conditions relating to the Galactic magnetic field, as well as the expected theoretical structure of the field. Large scale (mean) magnetic fields in galaxies are known to be driven by dynamo action. A dynamo is a self-sustaining magnetic field driven by the motion of charged particles. Fundamentally it arises as a consequence of the induction equation:

$$\frac{\partial \mathbf{B}}{\partial t} = \nabla \times (\mathbf{v} \times \mathbf{B}) + \eta \nabla^2 \mathbf{B} \tag{1.57}$$

$$\eta = \frac{1}{\mu_0 \sigma_0} \tag{1.58}$$

Where $\mathbf{v}$ is the velocity vector of the charged particles and where η is the magnetic diffusivity which is given by μ_0 the permeability of free space and σ_0 the electrical conductivity of the given material. The simplest and most widely used dynamo model used in the case of cosmic magnetic fields is known as the α-Ω dynamo. The 'α' term of this model accounts for turbulent motions in the ionised medium, and the Ω term accounts for differential rotation through the medium. Each of these terms are essentially models for the '$\mathbf{v}$' term in the induction equation. Haverkorn and Heesen noted that whilst this model is thought to act in the sun, further alterations to the model are required before the α-Ω dynamo can be applied to a galactic field.

For a galactic disk with differential rotation, the mean galactic field solution is of a quadrupolar configuration, where the field is mirrored about the galactic disk plane. For a structure such as the Galactic halo a model of a weakly rotating spherical medium produces a dipolar mean field. In practice there are two features which would allow observations to determine which configuration is present in the Milky Way; the vertical and azimuthal components of the mean field. For a quadrupole configuration, the azimuthal components remain the same above and below the Galactic plane, whilst the vertical component switches direction (see Figure 1.5 - left). For a dipolar configuration, however, the azimuthal component would reverse its direction above and below the Galactic plane, but the vertical component would not (see Figure 1.5 - right).

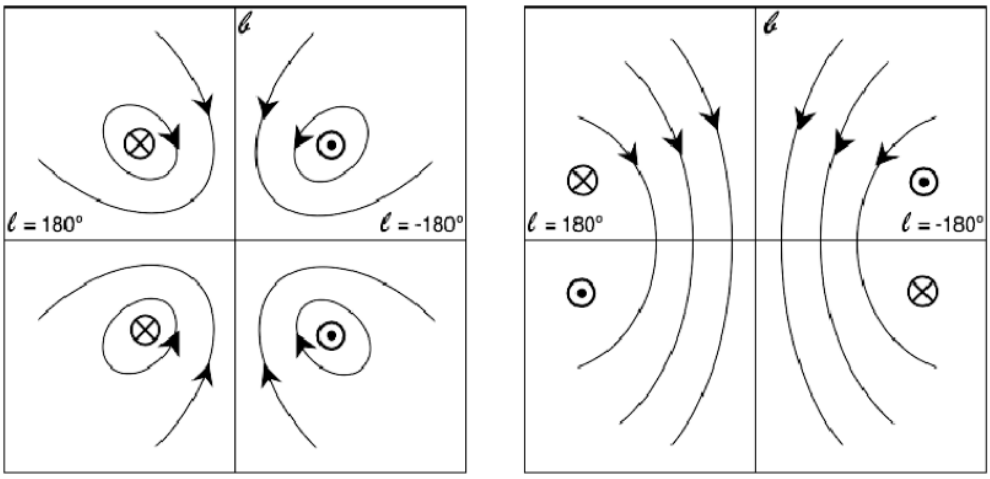

Figure 1.5: "Quadrupole (left) and dipole (right) large-scale magnetic field configurations of the Milky Way as a function of Galactic longitude and latitude. Magnetic field towards the viewer is denoted by a dot, field away from the observer as a cross." Haverkorn and Heesen (2012)

Haverkorn and Heesen (2012) also discussed another possible field structure observed in several galaxies. In the haloes of many edge-on galaxies, a mean field configuration with an 'X' shape is observed. This 'X' shape describes the field lines pointing radially outward from the galactic centre. The origin of this structure is yet to be reliably determined, but it is thought to be driven by galactic winds and the outflow of ionised gas. It is possible that the magnetic field is being dragged out along ionised outflows caused by star formation regions.

1.5 Extra-Galactic Source Rotation Measure Studies

To date the majority of work to model the magnetic field of the Milky Way by way of Faraday rotation has been done using extra-Galactic radio sources (EGRS). Beck and Wielebinski (2013) summarised in their review paper much of the work that has been done using EGRS. They noted that care must be taken in computing the Faraday depth of EGRS. Consider if a given source is some radio galaxy. The Faraday depth as measured on Earth will be the combined effect of local rotation (i.e. within the Milky Way), intergalactic rotation and rotation occurring within the radio galaxy itself. As such the extragalatic contributions from both intergalactic space and the radio galaxy must be separated from Galactic contributions before work is done on computing magnetic fields in the Milky Way. Rotation measure synthesis is an excellent method of accomplishing such a distinction.

Oppermann et al. (2015) have analysed one of largest collections of extragalactic Faraday depths with the purpose of computing the extragalatic contribution to Faraday rotation. They combined several existing catalogues of Faraday depths including the NRAO VLA Sky Survey (NVSS) (Taylor et al. (2009)) and the catalogue produced by Mao et al. (2012). The resultant catalogue contains 41632 sources. Oppermann et al. set about categorising and analysing this data pool and this produced several very useful results. They have provided estimates for the extra-galatic Faraday rotation contribution for much of the sky, although they noted that the Southern Hemisphere coverage is unfortunately lacking. Conversely, they also provide estimates of the Galactic foreground contribution, which would provide an excellent source of comparison for any other studies of Galactic Faraday rotation.

With respect to computing B-field information in the Milky Way, some the most important results have been found by Mao et al. (2010) and Mao et al. (2012). Mao et al. (2010) presented a study of the vertical magnetic field in the polar caps ($|b| \geq 77°$). They studied > 1000 EGRS using the Westerbork Radio Synthesis Telescope and the Australia Telescope Compact Array. Performing rotation measure synthesis they obtained a median Faraday depth of $\phi = 0.0 \pm 0.5\,\mathrm{rad\,m^{-2}}$ around the North Galactic pole and $\phi = +6.3 \pm 0.7\,\mathrm{rad\,m^{-2}}$ around the South Galactic pole. Their conclusion from this result was that there was "no coherent vertical magnetic field in the Milky Way" at the position of the sun. Furthermore, they also argued that if this property were true of the Milky Way's field globally, the lack of vertical field symmetry rules out pure dipolar and quadrupolar field models.

Mao et al. (2010) gave a study of the Faraday depths of 641 EGRS in the Galactic plane within $|b| \leq 30°$ and $100° < l < 117°$ using the VLA. For their low latitude ($|b| < 15°$) measurements they found that the Faraday depth was distributed symmetrically around the Galactic plane. They found this measurement would be consistent with an even parity disk field in the Perseus arm. In their higher latitude observations ($15° < |b| < 30°$) they found median Faraday depths of $\phi = -15 \pm 4$ rad m^{-2} and $\phi = -62 \pm 5\,\mathrm{rad\,m^{-2}}$ in the Northern and Southern Galactic hemispheres, respectively. Again, assuming that if this is indicative of overall Galactic magnetic structure, they concluded that the halo magnetic field does not reverse direction across the disk. They proposed that this structure could be indicative of a spiral halo magnetic field similar to the type observed in galaxy M51.

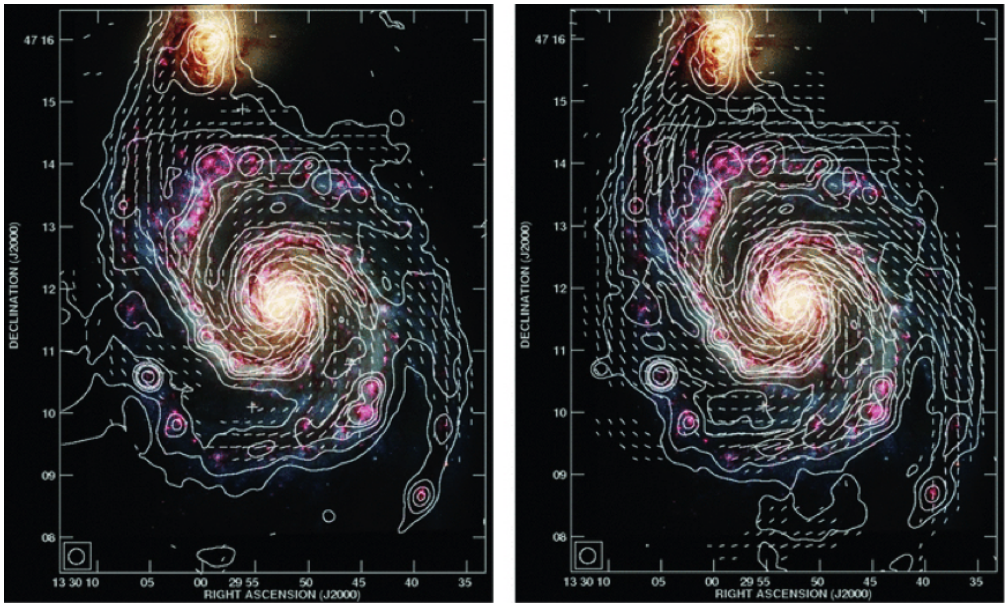

Figure 1.6: Hubble image of M51 with B-field vectors overlaid from polarised emission. Fletcher et al. (2011)

1.6 Continuum Rotation Measure Studies - GMIMS

Whilst extragalactic sources are an excellent means of probing the Galactic magnetic field, their point-like nature means they are not as suited to the study of fine Faraday depth structure as diffuse continuum measurements. As such, study of the polarised Galactic diffuse synchrotron emission would allow for high detail studies to be made on the Galactic magneto-ionic medium. With this in mind Wolleben et al. (2009) presented the Global Magneto-Ionic Medium Survey (GMIMS). This project aims to provide a whole sky map of diffuse polarised emission from 300 MHz to 1.8 GHz using single dish telescopes. Specifically, GMIMS will provide calibrated whole sky cubes of Stokes Q, U and I. The project will aim for a frequency resolution of at least 1 MHz and an angular resolution of $30' - 60'$. Such a study has only recently become possible with the development and implementation of wide-band receivers in radio telescopes. The major contributing telescopes to GMIMS are the Dominion Radio Astrophysical Observatory (DRAO) 26 m and the Parkes 64 m telescope covering the Northern and Southern Hemispheres, respectively. GMIMS is the first survey of its kind providing whole sky, large-scale, polarised emission data from single dish telescopes. This survey provides a superb data set for the application of rotation measure synthesis techniques.

Chapter 2

Data Set and Uncertainty

2.1 DRAO 26 m Rotation Measure Synthesis Survey

2.1.1 Introduction

The DRAO 26 m rotation measure synthesis survey was first published in Wolleben et al. (2010). This survey used the DRAO 26 m Telescope to produce a continuum, whole-sky map of polarised intensity (PI) (Stokes Q and U) from 1277 to 1762 MHz in 2048 frequency channels. The half-power beam width is quoted as between 40 and 30 arcmin. The purpose of this data was to enable the use of rotation measure synthesis (RMS) and thus allow the study of the magneto-ionic medium as observed in continuum polarised emission. Hence, the Fourier transform of this data was also produced giving the Faraday depth dispersion function (as described in Section 1.2) for each line of sight. The survey gives Northern sky coverage from a declination of $\delta = +90°$ down to $\delta = -30°$.

The final reduced version of the survey was released in September 2015. The major improvements between the initial and final data releases are twofold; firstly, spurious detections in polarised intensity have been thoroughly flagged and removed from analysis; and secondly, the Fourier spectrum as produced by RMS has been deeply 'cleaned' by deconvolution. The data is presented in the form of several three-dimensional Flexible Image Transport System (FITS) data 'cubes'. This included the following as functions of frequency: Stokes Q, Stokes U, Stokes Q and U ($\sqrt{Q^2 + U^2}$) (PI) in both Galactic and Equatorial coordinates. Also included were RMS cubes as functions of Faraday depth (ϕ) in Galactic and Equatorial coordinates. These RMS cubes give the intensity of the cleaned Faraday dispersion function, characterised by polarised brightness temperature (T_b) in Kelvin (K), for each line of sight on the sky, with a range of $\phi = -350\,\mathrm{rad\,m^{-2}}$ to $\phi = +350\,\mathrm{rad\,m^{-2}}$. The spatial sample spacing in all the cubes for both the Galactic and Equatorial is 0.5° per pixel, the frequency resolution is 23.6816 kHz per channel. The bandwidth observed resulted in a Faraday depth channel width of $5\,\mathrm{rad\,m^{-2}}$.

2.1.2 Polarised intensity

The spurious detections in polarised intensity can, of course, come from a wide number of sources; most notable, though, is the Global Positioning System (GPS) L1 satellite band at around 1.58 GHz (Misra and Enge, 2011). The flagging around such bands is clearly seen in Figures 2.1 and 2.2. Figure 2.1 shows a line profile through the PI cube at $b = 49°$ and $l = 27°$ showing strong flagging around the GPS L1 band. Figure 2.2 is a slice of the PI cube, which shows a map of polarised intensity at a frequency near to GPS L1 of 1575 MHz. The resulting maps appear heavily flagged around this frequency band.

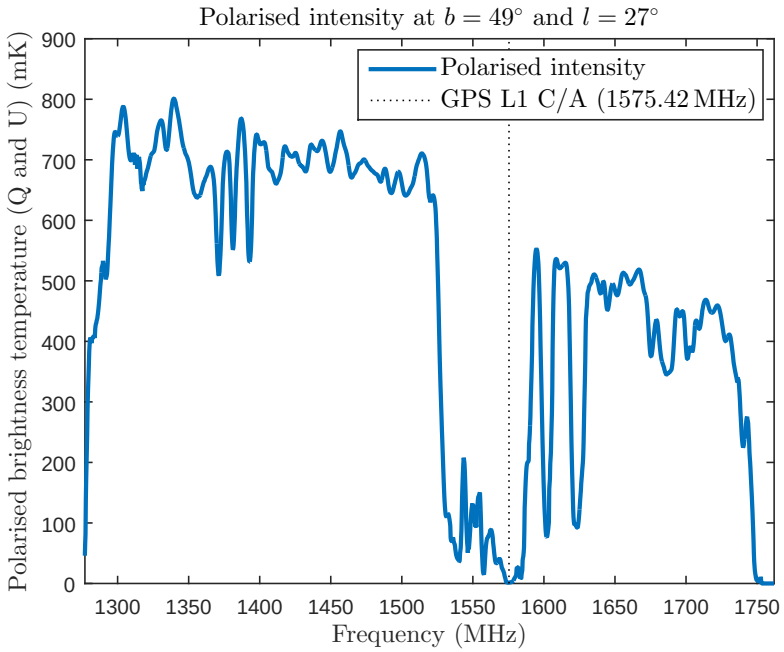

Figure 2.1: Smoothed PI profile at latitude 49° and longitude 27° with GPS L1 band indicated.

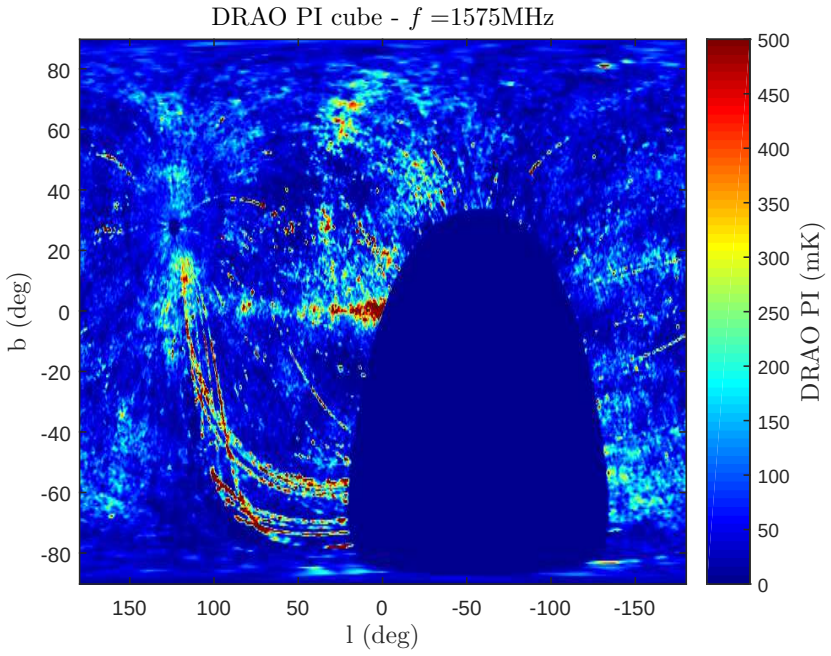

Figure 2.2: Smoothed PI map in galactic coordinates at a frequency of 1575 MHz.

As it is not possible to show the entirety of each cube in printed form, consider instead the following two maps in Figures 2.3 and 2.4. These maps are slices from the PI cubes at 1519 MHz (the median frequency) in Galactic and Equatorial coordinates, respectively. Figure 2.4 provides a less distorted view of the Galactic poles, which will come into consideration later. Bear in mind that the North Galactic Pole (NGP) is centred on $l = 0°$ and $b = 90°$ in Galactic coordinates which corresponds in turn to $\delta \approx 27°$ and $\alpha \approx 193°$ in Equatorial coordinates. Similarly, the South Galactic pole is centred on $l = 0°$ and $b = -90°$ in Galactic coordinates and $\delta \approx -27°$ and $\alpha \approx 13°$ in Equatorial coordinates. The polarised intensity shown in these frequency slices is typical of the cube overall. The two most dominant structures in polarised intensity are the North Polar Spur (NPS) and the Fan Region (FR). The NPS is centred around $l \approx 20°$ and extends in latitude from the Galactic plane up to about $b \approx 80°$. The FR appears near the Galactic plane, extending above and below by about 20° in latitude and is centred around $l \approx 140°$. As the NPS and FR are the brightest regions in the polarised sky, and therefore the most obvious for study, analysis has already been conducted on each region by Sun et al. (2015) and Hill et al. (2015) respectively.

An additional feature worth attention is the apparent depolarisation that is present in low latitudes. Recall from Section 1.3 that emission measure (EM) gives the line integral of electron density squared and can be measured from $H\alpha$ intensity. Figure 2.5 is a Northern sky map of $H\alpha$ emission from the WHAM survey (see Section 1.3). Comparing this to the DRAO polarised intensity, which is shown in Figure 2.6, with the same projection, it demonstrates clear anti-correlation around the Galactic plane. That is, there is a lack of polarised emission in regions that contain bright $H\alpha$ emission. For these regions, at the very least, it is possible to conclude that depolarisation has occurred.

This depolarisation effect introduces a greater level of complexity to considerations of the Faraday depth. Additionally, the computation of vertical magnetic fields as outlined by Mao et al. (2010) requires consideration of Faraday depth at the Galactic poles, not at lower latitudes. As such, in-depth analysis of Faraday depth in the data will only be carried out in the North and South Galactic pole.

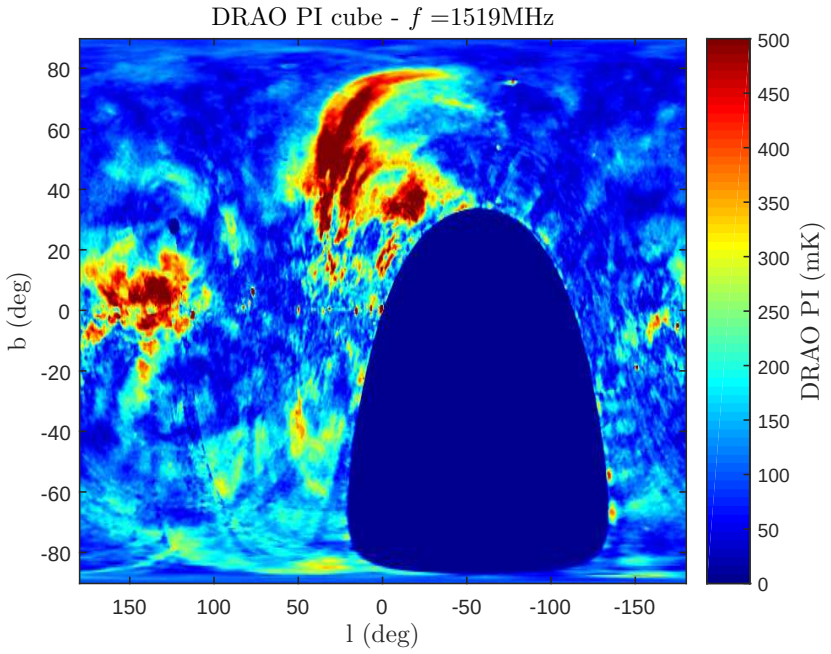

Figure 2.3: Smoothed PI map in Galactic coordinates at a frequency of 1519 MHz.

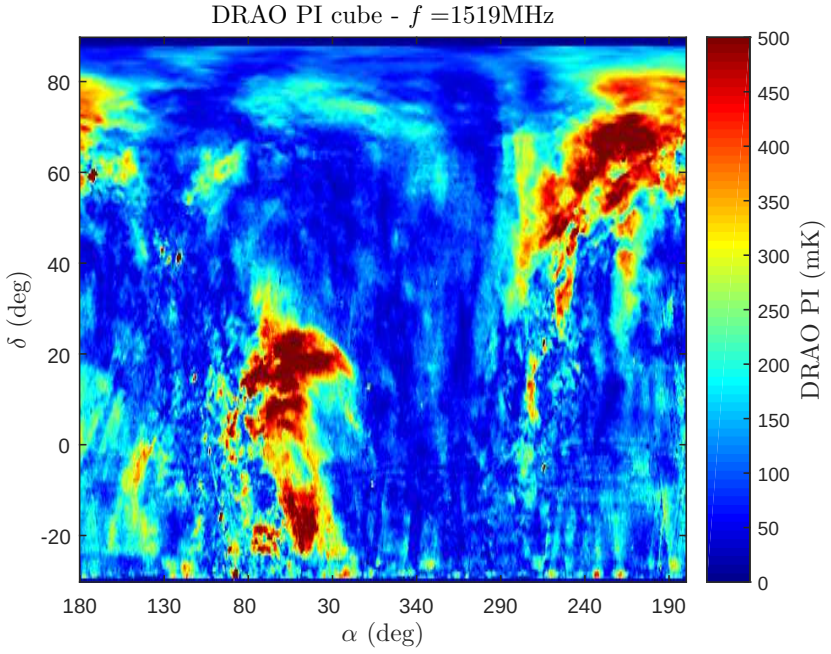

Figure 2.4: Smoothed PI map in Equatorial coordinates at a frequency of 1519 MHz.

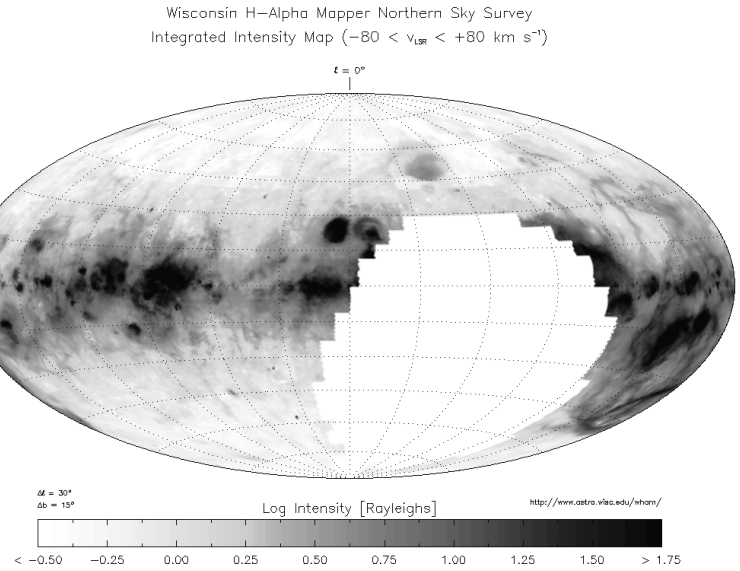

Figure 2.5: $H\alpha$ intensity map from WHAM survey Haffner et al. (2001).

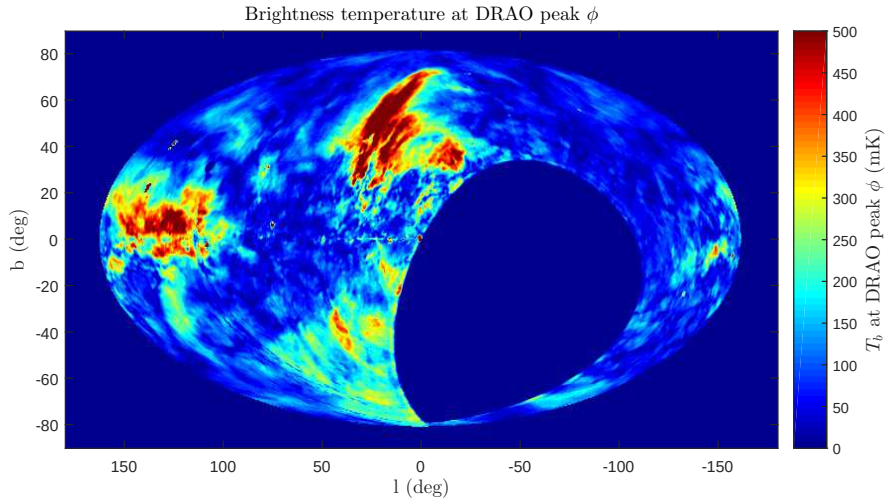

Figure 2.6: Smoothed PI map in Galactic coordinates at a frequency of 1519 MHz in Hammer-Aitoff projection.

2.1.3 Faraday depth

The RMS cubes, being the result of rotation measure synthesis, require additional consideration when being viewed. Consider the line profile shown in Figure 2.7.

This profile taken at $l = 145.5°$ and $b = 89.5°$ shows the typical spectrum that can be seen throughout most of the Faraday depth cube. That is, a narrow peaked spectrum with the peak being somewhere near $\phi = 0\,\mathrm{rad\,m^{-2}}$ and small side-lobes out at more extreme values of Faraday depth. What is important to realise about this spectrum is that the width of the peak is, in fact, synthetic. In that, it is set by the observational parameters and not by some process at work in the observed medium. Additionally, the side-lobes present are resultant from the RMS process and should not be considered 'real' detections. Both of these properties arise from the RMTF (as defined in Equation 1.33), which is convolved with the Faraday dispersion function in the implementation of RMS. After RMS has been completed the resultant spectra contain many side-lobes around the main peak. These side-lobes occur because λ^2-space cannot be sampled continuously. The side-lobes are reduced by deconvolution in the 'cleaning' process. This removes most of the side-lobes that are present and reveals the peak in the spectrum more clearly. The result of this is, though, that the width of the peak is now set by the width of the deconvolving function.

The salient point of this consideration is that the RMS cube can be reduced down to a map where the Faraday depth for each line of sight is given by the position of the peak in the Faraday spectrum. Additionally, the corresponding map of polarised brightness temperature (T_b) is given by the height of the peak on the Faraday spectrum for each line of sight.

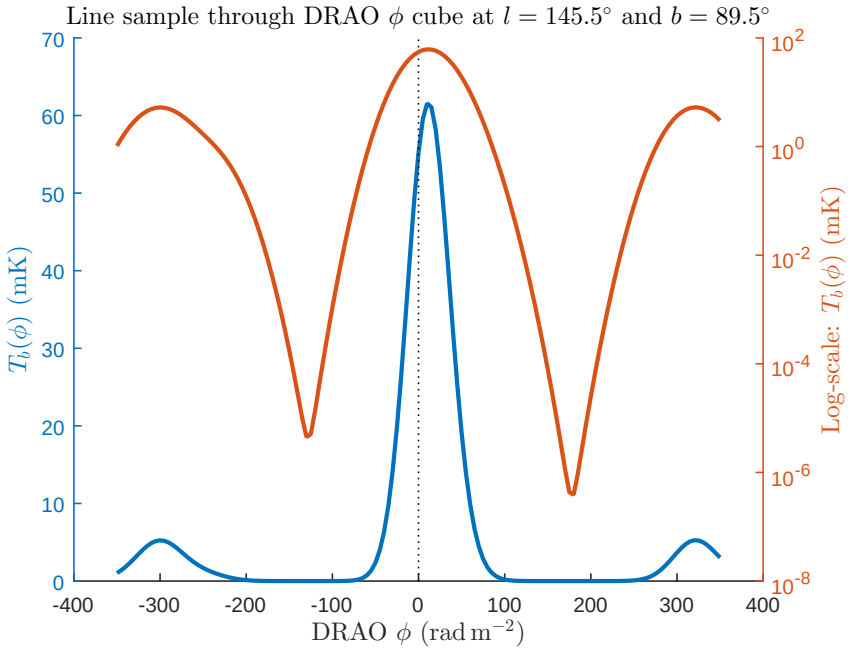

Figure 2.7: A typical line profile through Faraday depth cube.

Both Figures 2.8 and 2.9 are maps of Faraday depth in Galactic coordinates, as characterised by the peak of the Faraday spectrum for each line of sight. Figure 2.8 demonstrates that much of the Faraday depth is of low magnitude, with very little of the map showing a Faraday depth magnitude of $|\phi| > 100\,\mathrm{rad\,m^{-2}}$. The detail in Faraday depth is revealed when the limits in ϕ are brought down, as shown in Figure 2.9. Whilst some regions are saturated out by this range limiting, the detail that is revealed is very important for consideration; especially when compared to the polarised intensity.

The polarised intensity maps shown in Figure 2.10 give the height of the peak in the Faraday spectrum measured in polarised brightness temperature. The highest regions in this map appear to be point-like sources, thus the majority of the map appears dark in comparison and is not easy to read (see Figure B.1). To see the detail in the polarised brightness temperature, Figure 2.10 has a reduced range. Whilst this saturates regions like the NPS and FR, the detail in the map is much easier to read. Notably, this map appears very similar to the 'typical' map of polarised intensity shown in Figure 2.3, with many of the same structures present.

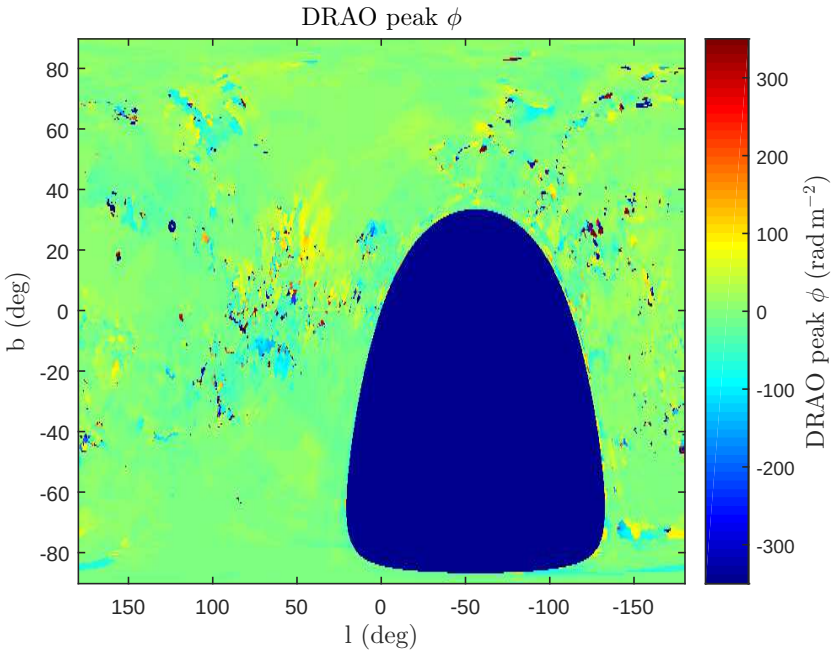

Figure 2.8: Map of peak Faraday depth in Galactic coordinates showing full range in ϕ.

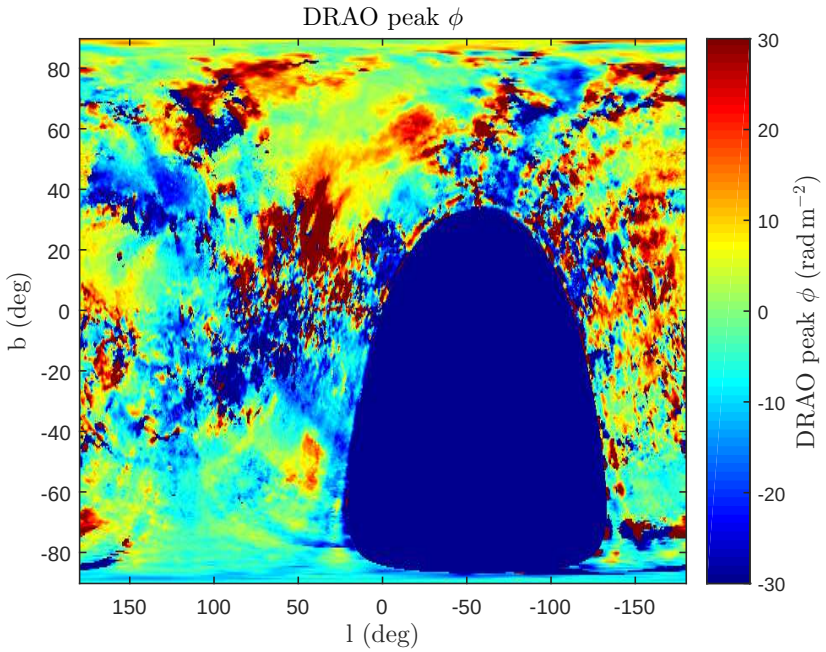

Figure 2.9: Map of peak Faraday depth in Galactic coordinates with range reduced in ϕ.

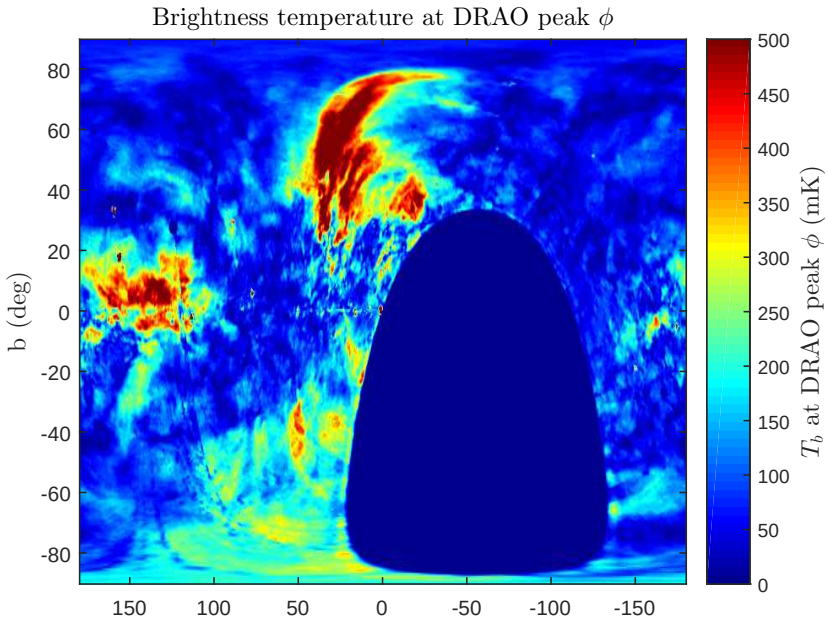

Figure 2.10: Polarised brightness temperature at peak in Faraday spectrum with range reduced.

2.1.4 Galactic Poles

The issue with these maps is that projection smears the North and South Galactic Poles across the top and bottom of the map respectively. For analysis to be conducted on the regions without having this significant distortion, the maps must be re-projected. The best method to view the poles is to apply a stereographic projection (see Section A.3). At the poles, in a stereographic projection, lines of constant latitude are concentric circles centred on the pole and lines of constant longitude are straight lines emanating radially from the pole. Each stereographic projection produced here is a 201 by 201 pixel map with an angular resolution of 0.2° per pixel, covering an angular area of 1600 deg^2 centred on each pole. The grid overlay in all the maps are contours of $l = 0^\circ$, 45°, 90°, 135°, 180°, 225°, 270°, 315°. The North Galactic Pole (NGP) has a contour grid of $b = 90^\circ$, 85°, 80°, 75°, 70°, 65° and in the South Galactic Pole (SGP) contours of $b = -90^\circ$, -85°, -80°, -75°, -70° ,-65° are overlayed.

2.1.4.1 North Galactic Pole

Figures 2.11 and 2.12 show the Faraday depth for each line of sight in the NGP with the same range limits as Figures 2.8 and 2.9 respectively. The stripe visible along the top right corner of the maps is a line along a right ascension of $\alpha \approx 180^\circ$ where data was not taken. Similar to the whole sky maps there are very few regions where the Faraday depth is of extreme magnitude. As such the detail in the Faraday depth structure is revealed in Figure 2.12 by reducing the range of ϕ shown.

Inspecting the polarised intensity map for this region in Figure 2.13 reveals that it is dominated by the tip of the NPS. The region containing the NPS is of significantly higher polarised intensity than the rest of the region and has a very well defined boundary. This makes it possible to distinguish the NPS from the rest of the polar region by thresholding the polarised brightness temperature. In this case it has been found that all emission with polarised brightness temperature $T_b \geq 200\,\mathrm{mK}$ is associated with the NPS only. This is shown in Figure 2.12 where the range in polarised brightness temperature has been reduced to $T_b \leq 200\,\mathrm{mK}$. This map reveals three other regions of higher polarised intensity and also demonstrates how remarkably sharp the edge of the NPS is.

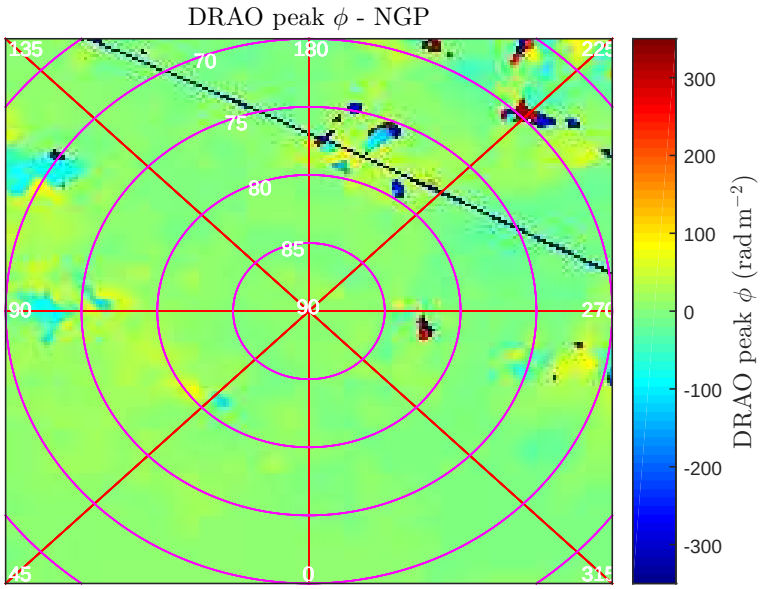

Figure 2.11: Map of peak Faraday depth in NGP showing full range in ϕ.

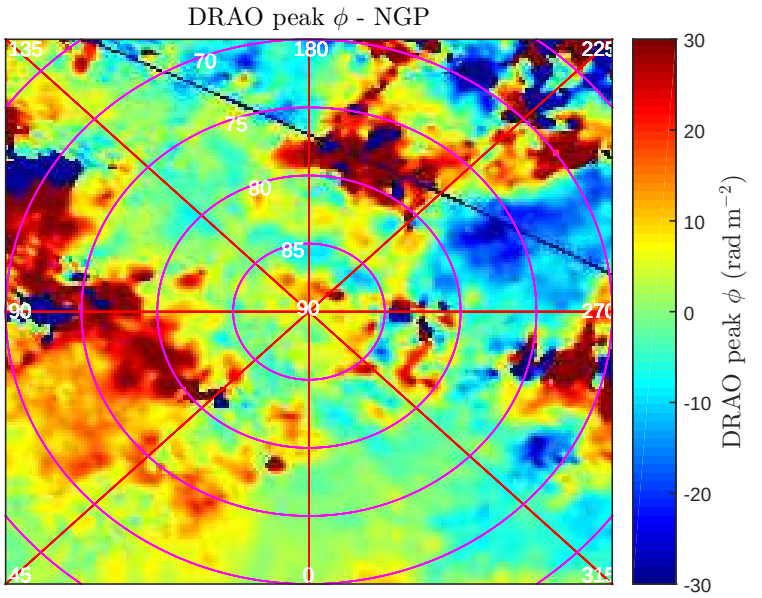

Figure 2.12: Map of peak Faraday depth in NGP with range reduced in ϕ.

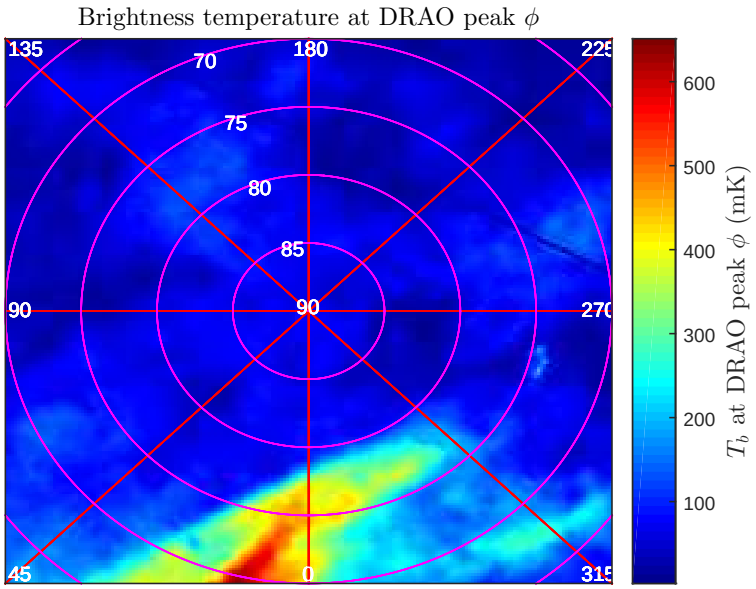

Figure 2.13: Polarised brightness temperature at peak in Faraday spectrum in the NGP.

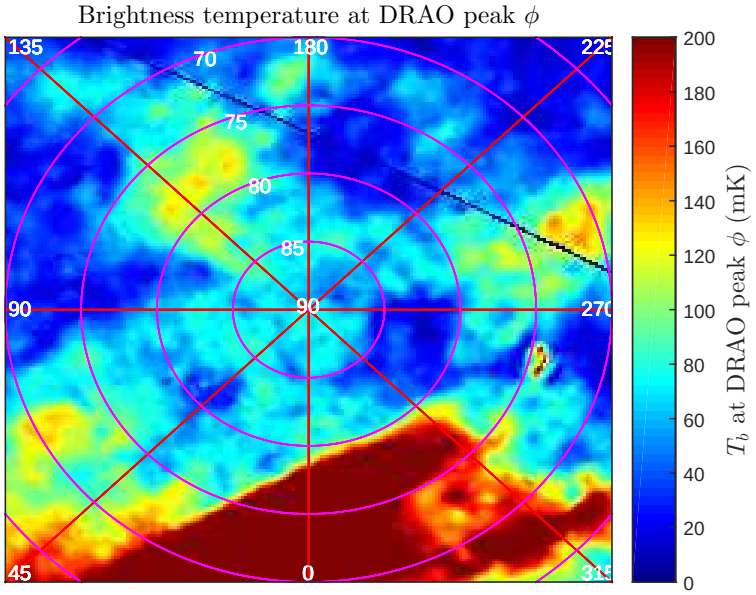

Figure 2.14: Polarised brightness temperature at peak in Faraday spectrum in the NGP with range reduced.

2.1.4.2 South Galactic Pole

Figures 2.15 and 2.16 show the Faraday depth for each line of sight, but now in the SGP. What is immediately obvious is that just under half the region is missing due to data not being taken below a declination of $\delta = -30°$. In addition, inspecting the detail visible in Figures 2.16 and 2.17 reveals a concerning trend. It would seem that scanning effects are still very present in the region, causing spurious detections. This is particularly clear in Figure 2.17, the map of polarised intensity in the SGP. There is an obvious line of clumps of polarised emission that follow the $\delta = -30°$ boundary, as well as strong stripes that run diagonally across the map. These scanning effects will need to be taken into consideration when analysis of the Faraday depth is made in this region.

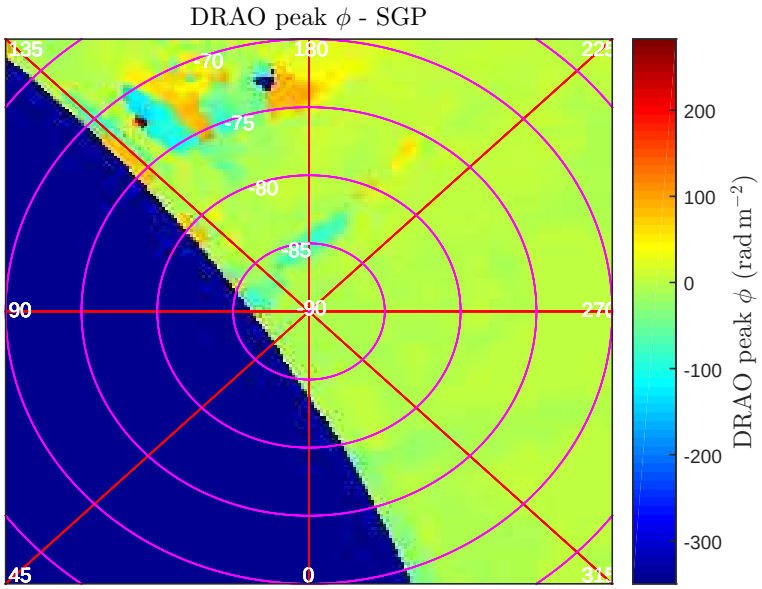

Figure 2.15: Map of peak Faraday depth in SGP showing full range in ϕ.

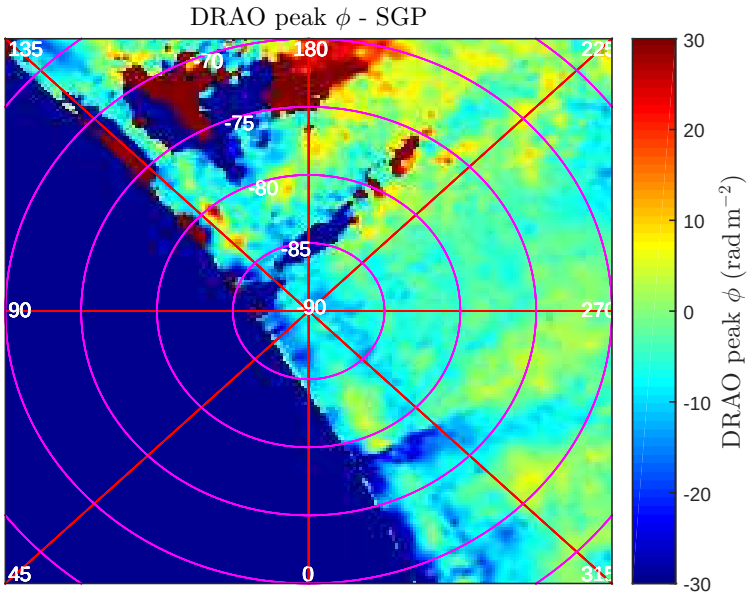

Figure 2.16: Map of peak Faraday depth in SGP with range reduced in ϕ.

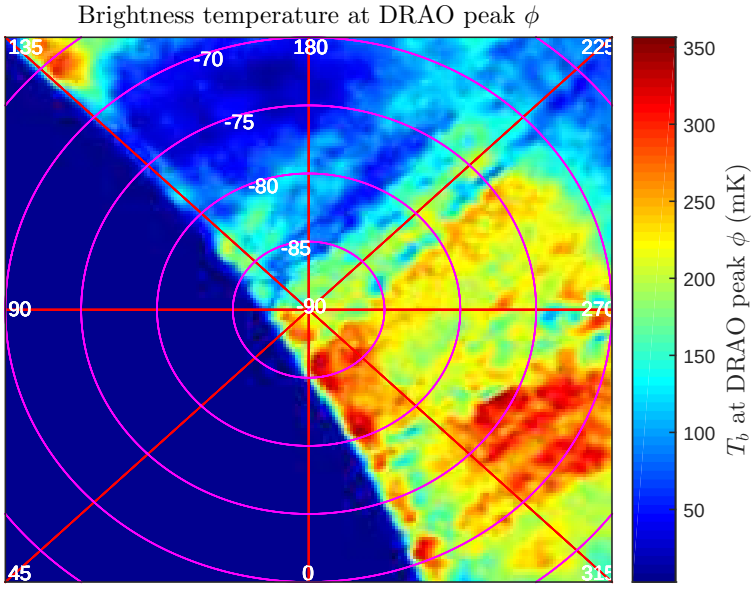

Figure 2.17: Polarised brightness temperature at peak in Faraday spectrum in the SGP.

2.2 Uncertainty in Faraday Depth

Before analysis can be conducted on any region, the uncertainty in Faraday depth must be understood. Sun (2013), following Condon (1997) and Brentjens and de Bruyn (2005), outlines the typical method used to determine the uncertainty in a given Faraday depth measurement ($\Delta\phi$) by way of Gaussian fitting. First, from the Stokes Q and U vs. frequency cubes a region free from obvious polarised emission structure is chosen. The standard deviation of polarised brightness temperature in this region (σ_i) is then computed and taken as the characteristic standard deviation for data. The standard deviation in the Fourier spectrum (σ) for a given line of sight is then:

$$\sigma = \frac{\sigma_i}{\sqrt{N}} \tag{2.1}$$

Where N is the number of samples in Faraday depth. The signal to noise ratio (SNR) is then given by:

$$SNR = \frac{\max\left(F(\phi)\right)}{\sigma} \tag{2.2}$$

Where $\max\left(F(\phi)\right)$ is the height of the peak in the Faraday spectrum. The standard deviation in the Faraday depth (σ_ϕ) for a given line of sight can then be approximated by a Gaussian fit:

$$\sigma_\phi \approx \frac{1}{2}\frac{\Theta}{SNR} \tag{2.3}$$

Where

$$\Theta = \frac{2\sqrt{3}}{\lambda^2_{\max} - \lambda^2_{\min}} \tag{2.4}$$

Here $\lambda_{\max}$ and $\lambda_{\min}$ are maximum and minimum wavelengths used to observe the polarised emissions, respectively. The uncertainty can then be quoted in the 99.7% confidence interval as:

$$\Delta\phi = 3\sigma_\phi \tag{2.5}$$

This standard approach has come under scrutiny, however, in Sun et al. (2015). In addition to their rotation measure (RM) analysis of the NPS, also using the DRAO 26 m rotation measure synthesis survey, Sun et al. (2015) produced "simulations to quantify RM errors". This entailed simulating a polarised source in the data of known Faraday depth and then putting it through the rotation measure synthesis process and calculating back the Faraday depth. This provided a value for the uncertainty in rotation measure (ΔRM) using the difference in the output and input RM, i.e.:

$$\Delta RM = RM_{\text{output}} - RM_{\text{input}}$$

Note that the 'rotation measure' referred to in Sun et al. (2015) is analogous to the Faraday depth (ϕ) referred to here. They then compared this uncertainty value

to the value that would be computed using the typical method of Gaussian fitting (given in Equation 2.3). Their result is shown in Figure 2.18, with the simulated uncertainty being much higher than the expected uncertainty.

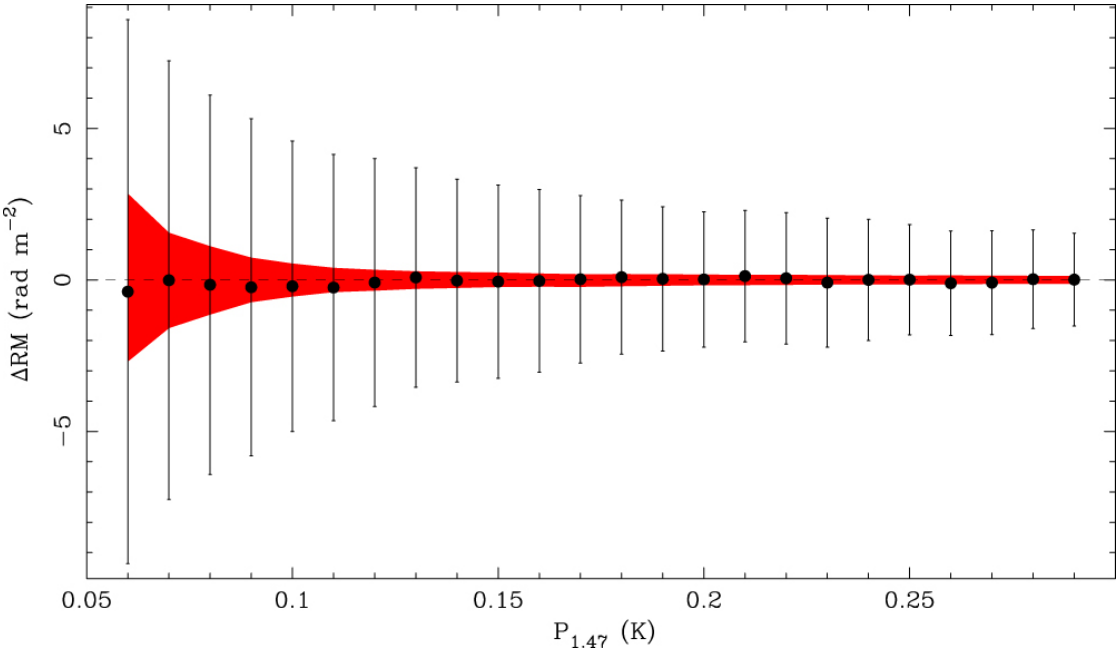

Figure 2.18: Sun et al. (2015): Result of comparison between uncertainty sources. Black error bars give the ΔRM from the simulated sources, the red region gives the ΔRM from Gaussian fitting.

The key result from this analysis is that there is a relationship between the polarised brightness temperature of a source and the uncertainty in Faraday depth. The resultant data from the simulation of uncertainty has been provided for use in this analysis. This data can be well fit by the following power law model:

$$\Delta\phi = (900 \pm 100) \times T_b^{(-1.15\pm0.03)} \tag{2.6}$$

Where $\Delta\phi$ is the uncertainty in the Faraday depth for a given line of sight and T_b is the polarised brightness temperature for that same line of sight. This fit has an adjusted $R^2 = 0.9957$ and the errors in the fit parameters are given with 95% confidence bounds. Figure 2.19 shows the plot of this fit against the data as well as the accompanying residuals of the fits. It is worth noting that the fits tends to underestimate the uncertainty in Faraday depth. As such, final use of the model may require the values to be increased to ensure errors are being treated appropriately.

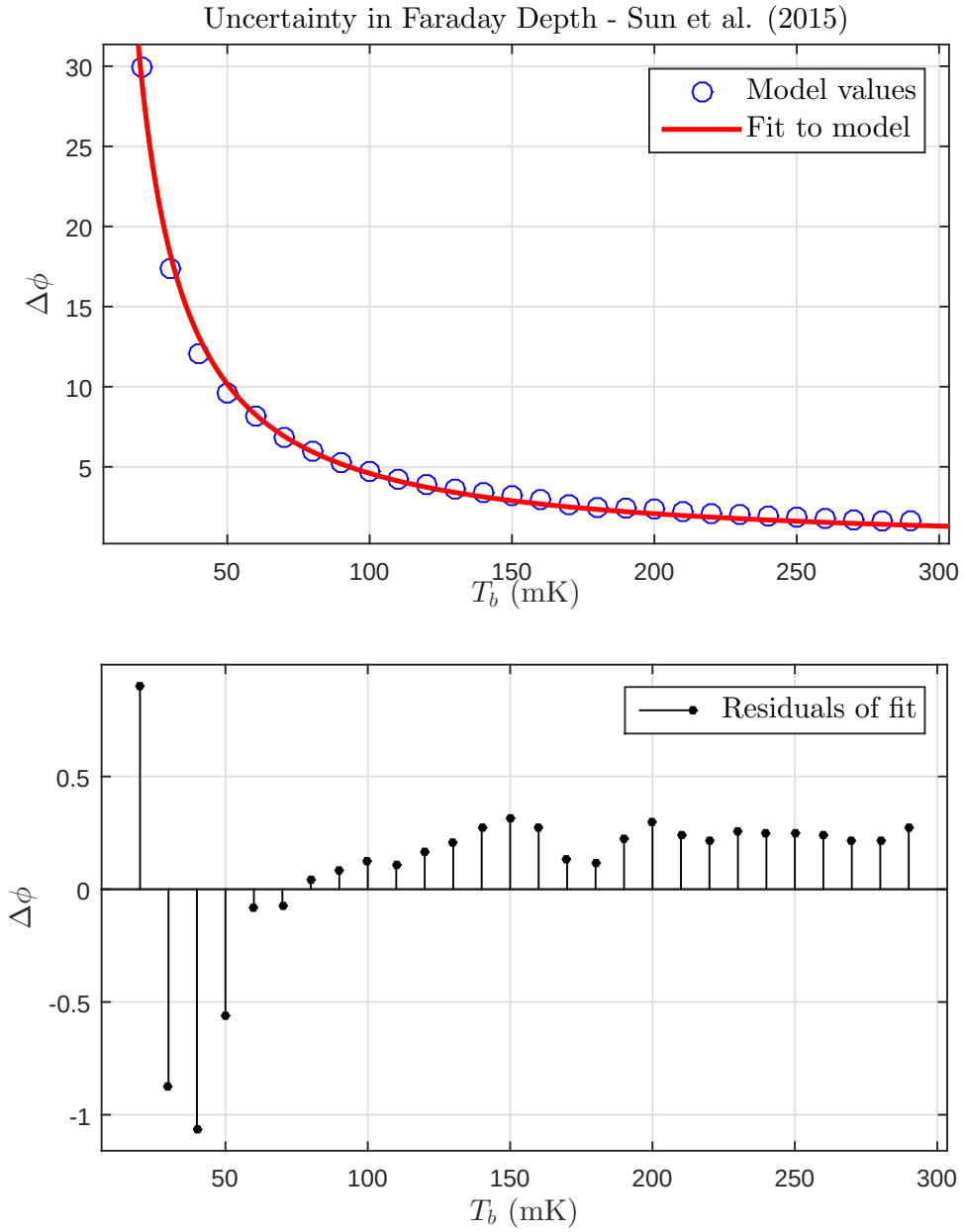

Figure 2.19: Upper: Uncertainty in Faraday depth from Sun et al. (2015) and power law fit. Lower: Residuals of power law fit.

As this is a power law relationship, it is far easier to view it on a 'log-log' scale as the power law will reduce a linear relation. This is provided in Figure 2.20. Finally, the Faraday depth (ϕ) can be determined by the values in the 'Peak ϕ' maps such as Figure 2.11. The uncertainty in that value can be determined by the power law relationship in Equation 2.6, sampling the polarised brightness temperature from

the T_b maps such as Figure 2.13.

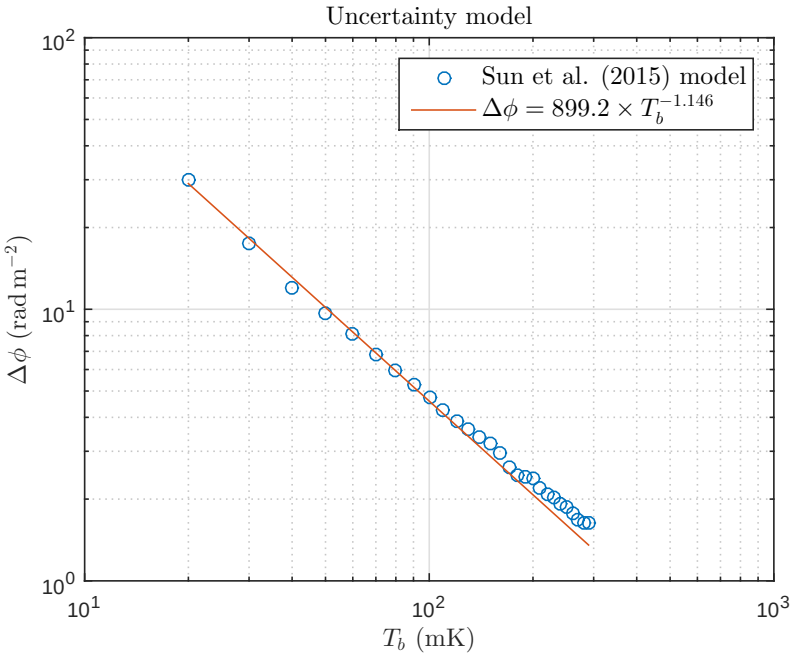

Figure 2.20: Uncertainty in Faraday depth from Sun et al. (2015) and power law fit on a 'log-log' scale.

Chapter 3

Faraday Depth Analysis

3.1 Averaging Faraday Depth

3.1.1 Introduction

In order to apply the method of vertical B-field computation outlined in Section 1.3 a mean Faraday depth is required for each polar region. Consideration should be made, however, of the structure present in the Faraday depth maps before a mean is computed. Comparison of the Faraday depth maps with their corresponding polarised intensity maps has revealed an important trend; especially considering the relationship between uncertainty in Faraday depth and polarised brightness temperature (shown in Equation 2.6). This trend is that the most extreme values of Faraday depth coincide with the lowest values of polarised brightness temperature. Given that low levels of polarised emissions are associated with greater uncertainty in Faraday depth, it is possible to conclude that these regions of large magnitude Faraday depth are spurious. This effect is demonstrated in Figure 3.1. The saturated black and white regions in this map are where high magnitude Faraday depth is present. All of these regions occur below 50 mK of polarised brightness temperature. Using Equation 2.6 this polarised brightness temperature corresponds to the uncertainty in Faraday depth being $\Delta\phi \geq 10\,\mathrm{rad\,m^{-2}}$. As such, in the process of computing a mean Faraday depth these regions need to be taken into consideration; i.e. excluded in some manner.

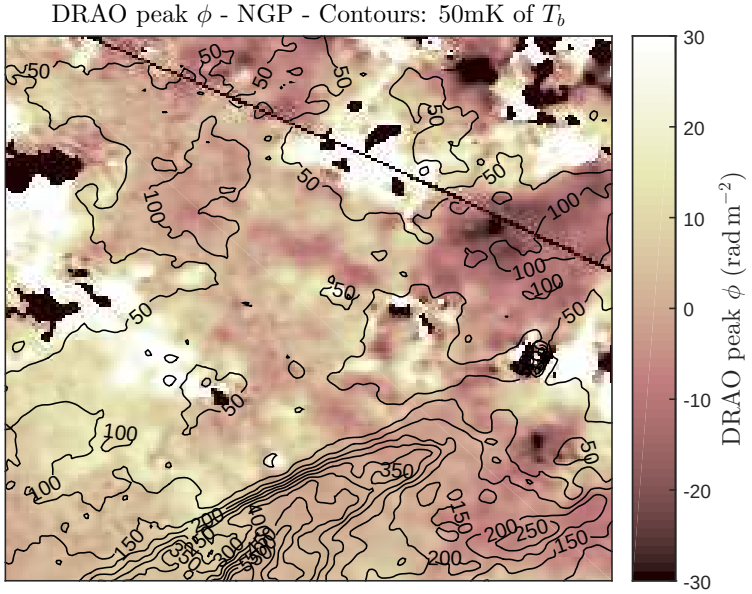

Figure 3.1: Faraday depth in the NGP with contours of polarised brightness temperature overlaid in 50 mK steps.

The most obvious method of excluding the spurious regions is to apply a threshold to the data, and discard data below that threshold. Using Equation 2.6 this thresholding can be done using levels of uncertainty in Faraday depth ($\Delta\phi$). A mean Faraday depth ($\phi_{\rm av}$) can then be computed for the remaining Faraday depth data, and the standard error in the mean is computed using:

$$SE_\phi = \frac{\sigma_\phi}{\sqrt{n}} \tag{3.1}$$

Where σ_ϕ is the standard deviation of Faraday depth in the sample. Care must be taken here, as n is strictly the number of independent samples in the mean. For the time being, the number of independent samples will be taken as the number of beam areas in the sample. This can be computed using the beam-size as quoted in Wolleben et al. (2010). Assuming an elliptical Gaussian profile, the angular size of the beam ($\Omega_{\rm beam}$) is given by Condon and Ransom (2007):

$$\Omega_{\rm beam} = \frac{\pi \times HPBW^2}{4\ln 2} \approx 1.13 \times HPBW^2 \tag{3.2}$$

Where $HPBW$ is the half-power beam width. Now, the number of independent samples (n) is given by:

$$n = \frac{k_{\rm sample}}{m} \tag{3.3}$$

Here, $k_{\rm sample}$ is the number of pixels in the sample and m is the number of pixels per beam in a given map. The number of pixels per beam is found using:

$$m = \frac{k_{\rm tot}}{\Omega_{\rm map}} \times \Omega_{\rm beam} = \frac{\Omega_{\rm beam}}{\Omega_{\rm pixel}} \tag{3.4}$$

Where $k_{\rm tot}$ is the total number of pixels in the map, $\Omega_{\rm map}$ is the angular area of the map and $\Omega_{\rm pixel}$ is the solid angle of a pixel in the map. For all of the maps in this analysis $\Omega_{\rm pixel} = 0.04\,deg^2$. Taking the upper limit of the $HPBW$ from Wolleben et al. (2010) as 40 arcmin, the number of pixels per beam in the maps under consideration is $m \approx 12.6$ pixels.

There is an alternative method to computing a mean in each region that still takes care of spurious values in Faraday depth. Namely, a method of weighted averaging. If the Faraday depth value of each pixel is weighted by its uncertainty as determined by Equation 2.6, then the weighted average should be an excellent indication of the mean Faraday depth in region. It is best to use the reciprocal squared of uncertainty for the weight of each pixel, that way the weight is consistent with the reciprocal of the variance of each line of sight and is also positive definite. The weighted mean is therefore given by:

$$\phi_{\rm av} = \frac{\sum_{i=1}^{k} \phi_i w_i}{\sum_{i=1}^{k} w_i} \tag{3.5}$$

Where ϕ_i is the Faraday depth for a given pixel and:

$$w_i = \frac{1}{(\Delta\phi_i)^2} \tag{3.6}$$

The standard error in a weighted mean is found using:

$$SE_\phi = \frac{1}{\sqrt{n-1}} \times RMS \tag{3.7}$$

Here, n is the same as defined above and RMS is the root mean square of the weighted average, which can be found by:

$$RMS = \sqrt{\frac{\sum_{i=1}^{k} \phi_i^2 w_i}{\sum_{i=1}^{k} w_i}} \tag{3.8}$$

These equations arise from consideration of error propagation (Maksimovic, 2003).

3.1.2 Faraday Depth in the North Galactic Pole

Three threshold levels of uncertainty were selected, below which data would not contribute to the calculation of a mean Faraday depth. These levels were:

1. No threshold
2. $\Delta\phi < 10\,\mathrm{rad\,m^{-2}}$
3. $\Delta\phi < 5\,\mathrm{rad\,m^{-2}}$

Additionally, a mean was found for the NGP both with and without the NPS. The effect of this thresholding can be demonstrated in a number ways. Firstly, consider the histograms shown in Figures 3.2 and 3.3. Figure 3.2 shows the distribution of Faraday depth values in the NGP; it has a strong peak around $\phi = 0\,\mathrm{rad\,m^{-2}}$ with minor side-lobes extending out to extreme magnitudes of Faraday depth. The presence of these values is likely associated with low level polarised emission which dominates the NGP and is shown in Figure 3.3. Bear in mind two things when considering the distribution of polarised emission. Firstly, regions with polarised brightness temperature less than 50 mK are certainly associated with spurious detections in Faraday depth. Secondly, polarised emission with brightness temperature $T_b > 200\,\mathrm{mK}$ are associated with the NPS only. The unfortunate result of this is that there is not a lot of polarised emission in the NGP that isn't associated with NPS that can be considered 'trustworthy' for use in Faraday depth analysis.

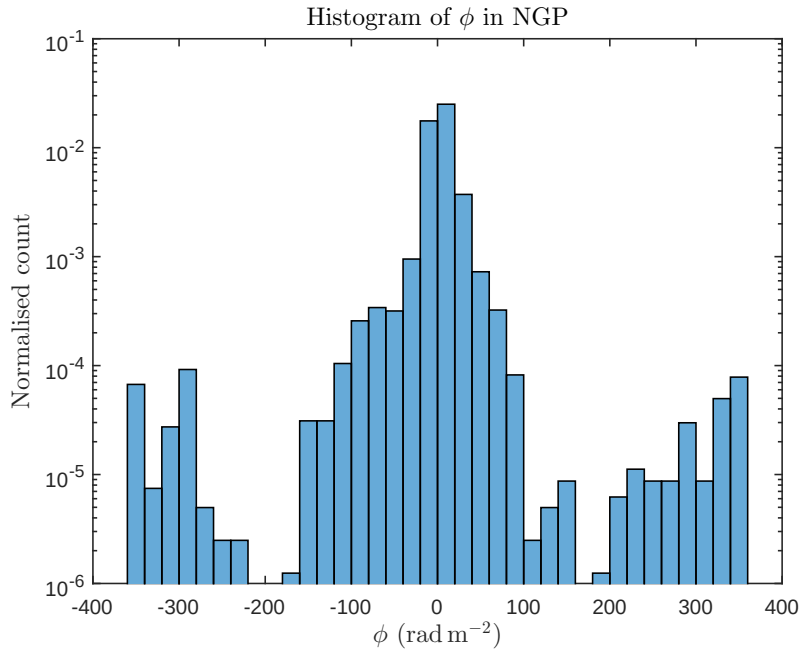

Figure 3.2: Histogram of Faraday depth in the NGP with logarithmic scale. Bin-widths are 20 rad m^{-2}

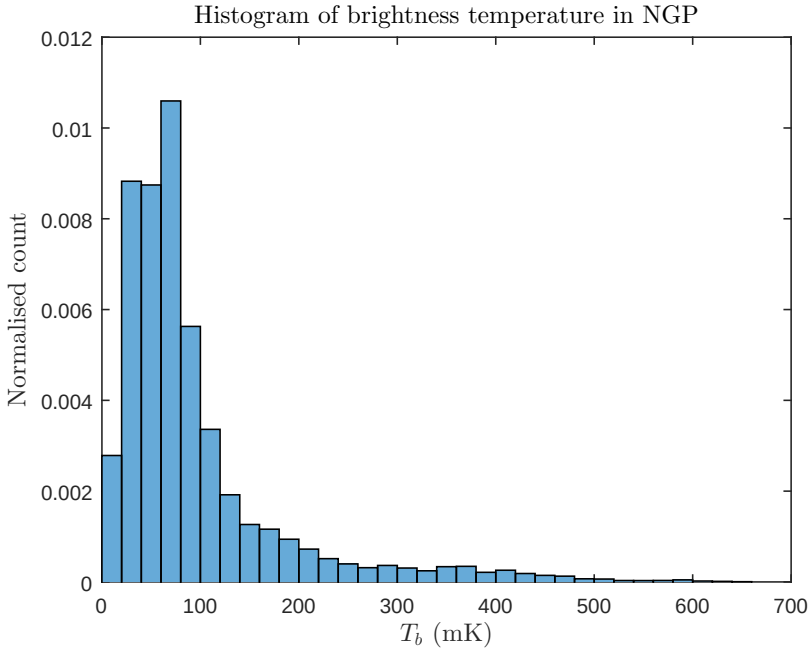

Figure 3.3: Histogram of polarised intensity in the NGP. Bin-widths are 20 mK

The impact of thresholding on the distribution of Faraday depth is shown in Figure 3.4. In this histogram, with each increase in threshold strength the side-lobes are reduced and the data becomes centralised around the peak. This is indicative that the method of thresholding is honing in on a common value.

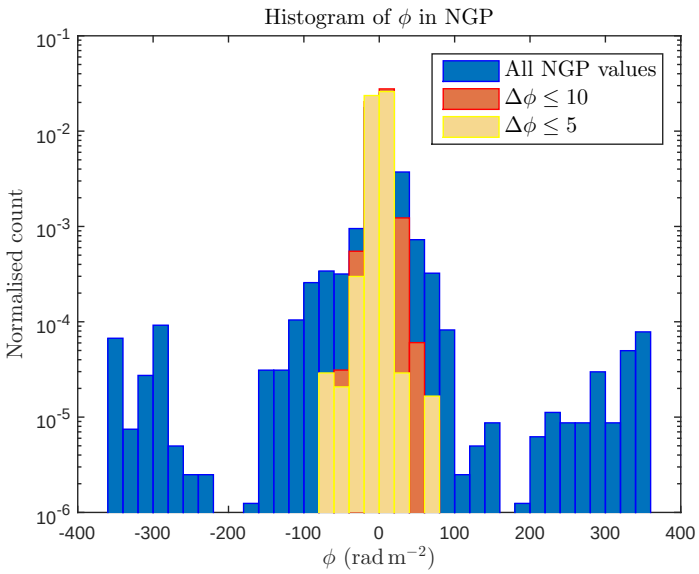

Figure 3.4: Histogram of Faraday depth in the NGP with thresholding. Bin-widths are $20\,\mathrm{rad\,m^{-2}}$

The effect of thresholding on the map of the NGP is shown in Figure 3.5. In Figures 3.5a and 3.5b it is possible to see that some extreme values of Faraday depth are still slipping past the threshold. Increasing the threshold (shown in Figures 3.5c/3.5d) excludes these spurious regions well, but there is a trade-off. As expected, there is very little data left at all not associated with the NPS. Averages for each of these maps, as well as maps without thresholding, are tabulated in Table 3.1.

What becomes apparent here is a trend in the Faraday depth across the sky. This is especially clear in Figure 3.5d. The trend is roughly positive in the bottom left of the map, zero in the centre and then negative in the top right. It is tempting, then, to perform a plane fit to this trend. To produce a fit map coordinates of x for horizontal pixels, y for vertical pixels and an origin at the bottom left corner of the map were used. The resultant plane fit is (with 95% confidence bounds):

$$\phi = (10.0 \pm 0.3) - (0.075 \pm 0.002)x - (0.053 \pm 0.003)y \tag{3.9}$$

How this relates to a possible B-field trend will be covered in Chapter 4. A map of this plane fit on the NGP is shown in Figure 3.6.

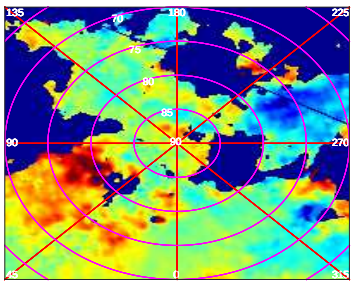

(a) $\Delta\phi < 10$

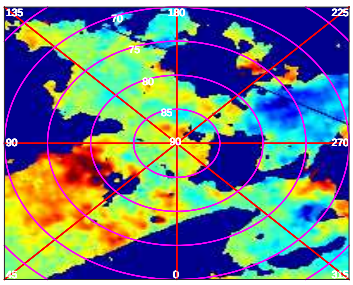

(b) $\Delta\phi < 10$ and NPS removed

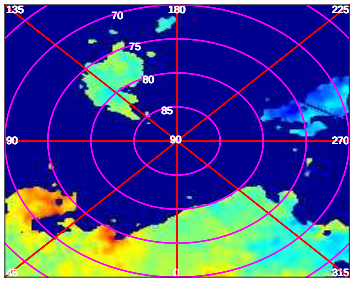

(c) $\Delta\phi < 5$

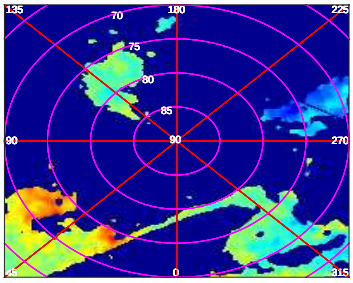

(d) $\Delta\phi < 5$ and NPS removed

Figure 3.5: Faraday depth maps in the NGP with thresholding. Range in all maps is $|\phi| \leq 30\,\mathrm{rad\,m^{-2}}$.

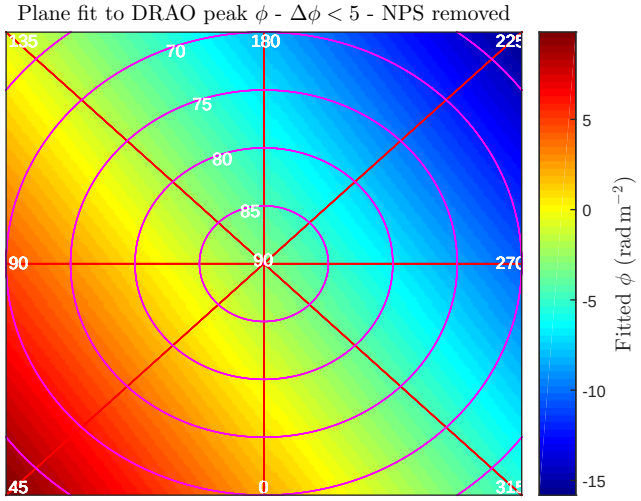

Figure 3.6: Map of plane fit to Faraday depth in the NGP.

Application of the weighted average method required extrapolation of the model given by Equation 2.6. This is demonstrated clearly in Figure 3.7. Here every value of polarised intensity has been sampled from the NGP region and passed through the power law fit of Equation 2.6. In the NGP there is polarised intensity both above and below what was modelled by Sun et al. (2015). In Figure 3.7 this can be seen where the fitted red line extends past the model values. It is therefore assumed that the model will hold true for these values.

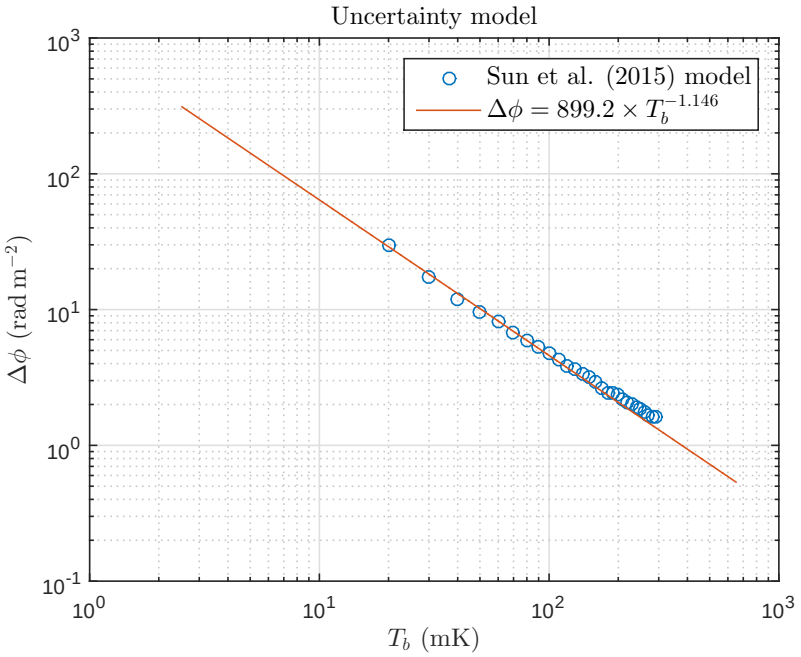

Figure 3.7: Model of uncertainty from Sun et al. (2015) sampling polarised intensity from the NGP.

Under this assumption Equations 3.5 and 3.6 were applied to the NGP region. The result of this, with the accompanying uncertainty is given in Table 3.1.

Method	ϕ_{av} with NPS (rad m^{-2})	ϕ_{av} without NPS (rad m^{-2})
No threshold	2 ± 2	3 ± 2
$\Delta\phi < 10$ rad m^{-2}	1.4 ± 0.6	1.4 ± 0.7
$\Delta\phi < 5$ rad m^{-2}	-0.2 ± 0.7	-1 ± 1
Weighted average	1.2 ± 0.3	0.1 ± 0.6

Table 3.1: Mean Faraday depth as found in the North Galactic Pole

The trend in the errors in Table 3.1 is a little confusing on first inspection. It would be expected that as the threshold is increased, the values left behind would be more consistent and therefore the error in the mean should go down. What is seen instead is that the error increases between the thresholds $\Delta\phi < 10\,\mathrm{rad\,m^{-2}}$ and $\Delta\phi < 5\,\mathrm{rad\,m^{-2}}$. The explanation for this arises from the fact that thresholding in the NGP removes so much data. As noted previously there is a trend across the NGP region. The mean in the region, however, is close to zero. With so little data remaining, this causes the standard error to increase. The low level of polarised emission in the NGP makes it difficult to apply thresholding. It is difficult to balance keeping enough data vs. removing spurious regions. This being the case, it appears that the best method of obtaining an average here is the weighted average technique. The values obtained here will be used to analyse the B-field in Chapter 4.

3.1.3 Faraday Depth in the South Galactic Pole

Before analysis of Faraday depth can be conducted on the SGP, the scanning effects present must be dealt with. This was done using a simple mask, where the most obviously striped data was removed from the region. Two masks were applied; the first removed data between declinations of $\delta = -30°$ and $\delta \approx -25°$; the second removed a column of the worst stripe near the pole. Maps of the SGP with the mask applied in Faraday depth and polarised intensity are given in Figures 3.8 and 3.9 respectively. This masking, in combination with the data that is already missing from the pole, means that $\sim 55\%$ of the data is missing from the region.

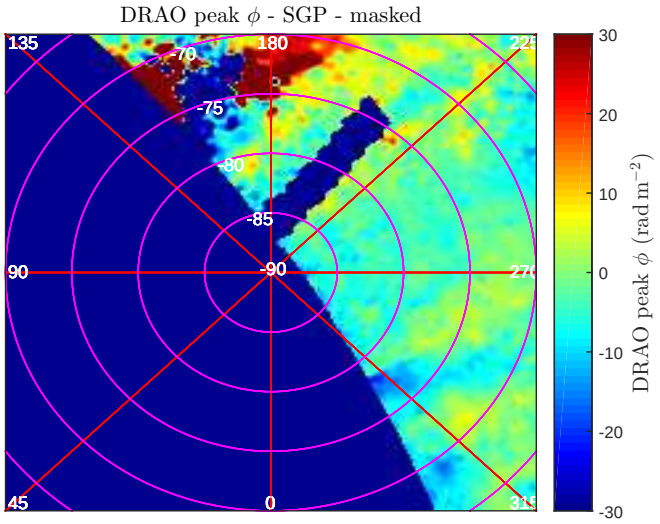

Figure 3.8: Map of Faraday depth in the SGP with masking applied.

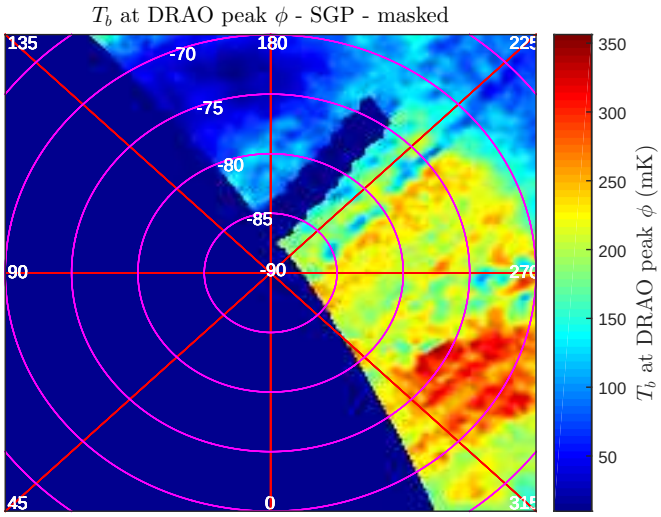

Figure 3.9: Map of polarised brightness temperature in the SGP with masking applied.

As a full view of the SGP would be required for analysis of trends in Faraday depth, only a mean value for the region will be investigated here. The same techniques of thresholding and weighting that were applied to the NGP were also applied to the NGP. The advantage in the SGP over the NGP is that polarised intensity is higher overall, as shown in Figure 3.11. Despite this, there is still some low level emission producing spurious Faraday depth detections. Here strongly negative Faraday depths appear in Figure 3.10, which are associated with the region of low level emission near $l \approx 180°$ seen in Figure 3.9.

The method of thresholding appears to be particularly effective here, as shown in Figure 3.12. As the polarised emission is brighter in the SGP, less data is being discarded by thresholding by uncertainty. This is also demonstrated in Figure 3.13. In these maps it can be seen that most of the remaining data is kept for analysis. The averages produced by thresholding are given in Table 3.2.

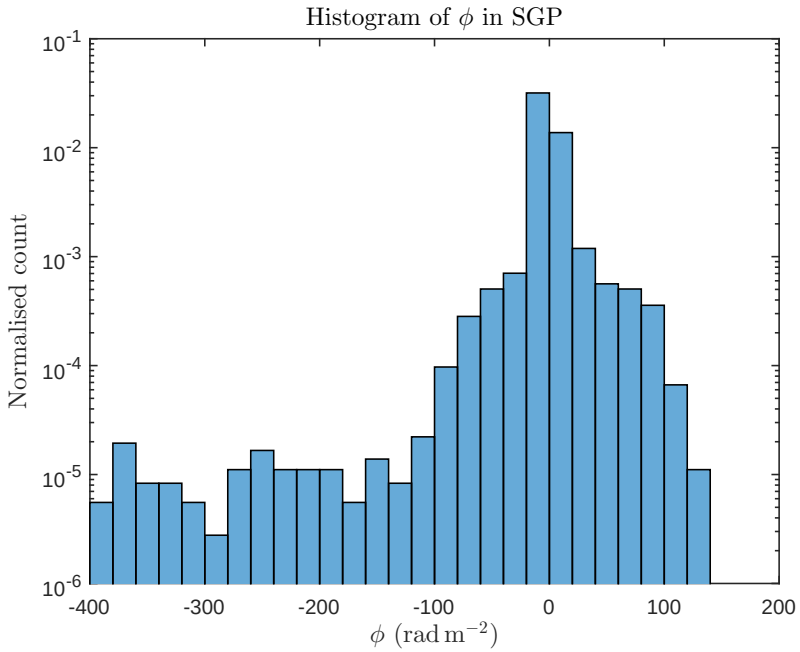

Figure 3.10: Histogram of Faraday depth in the SGP with masking. Bin-widths are 20 rad m^{-2}

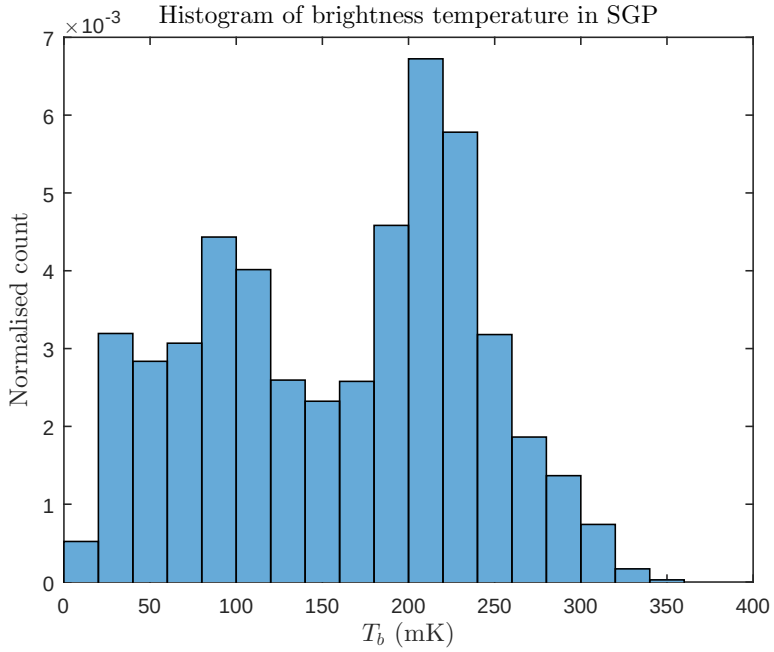

Figure 3.11: Histogram of polarised intensity in the SGP with masking. Bin-widths are 20 mK

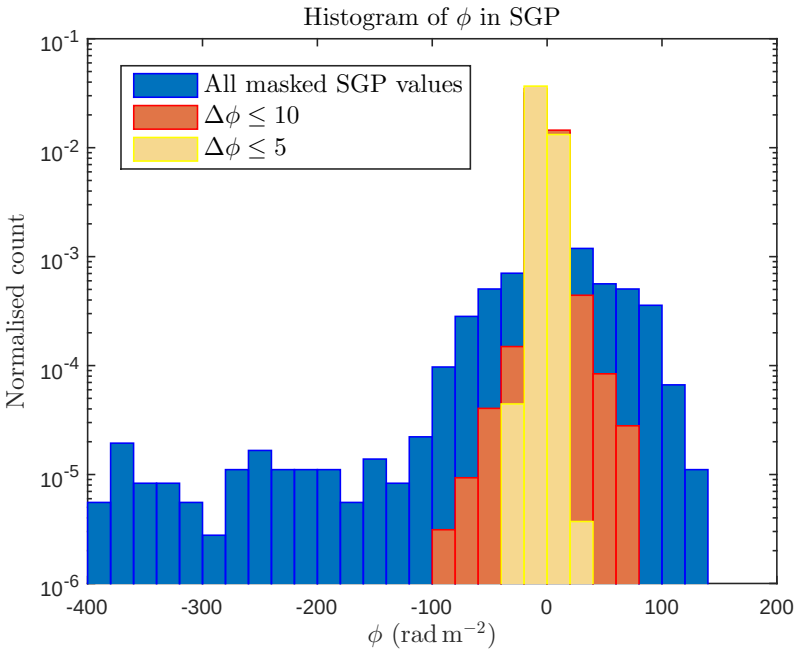

Figure 3.12: Histogram of Faraday depth in the SGP with masking and thresholding. Bin-widths are 20 rad m^{-2}.

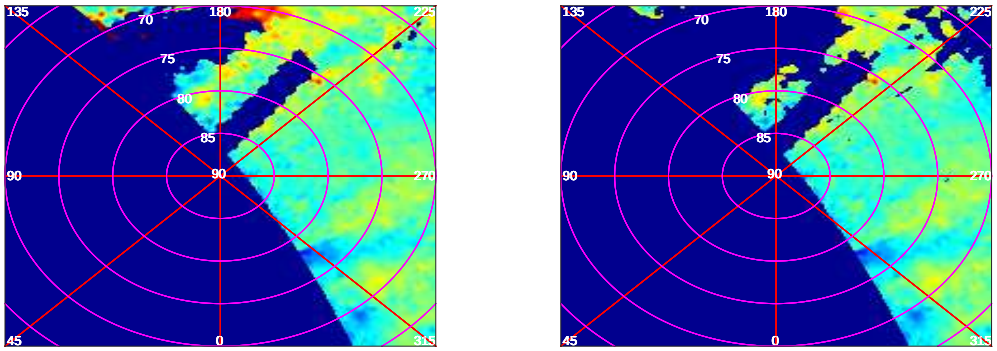

(a) $\Delta\phi < 10$ (b) $\Delta\phi < 5$

Figure 3.13: Faraday depth maps in the SGP with masking and thresholding. Range in both maps is $|\phi| \leq 30$ rad m^{-2}.

To apply a weighted average the model from Sun et al. (2015) must again be extrapolated. The extrapolation of the fit in shown in Figure 3.14. Assuming that the model holds out to these high and low values of polarised emission, weighted

averages were found for the SGP. The values found are given in Table 3.2 along with the appropriate errors.

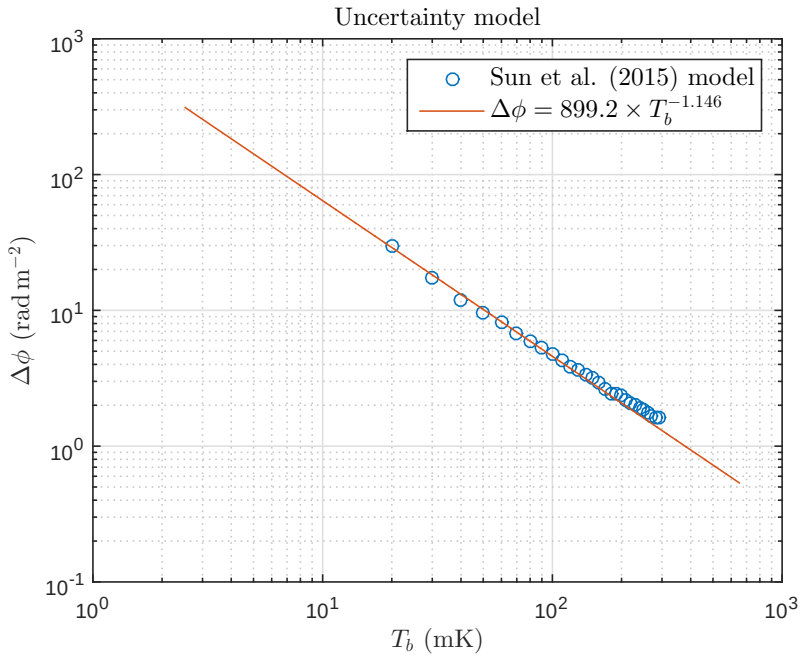

Figure 3.14: Model of uncertainty from Sun et al. (2015) sampling polarised intensity from the SGP.

Method	ϕ_{av} with mask (rad m^{-2})	ϕ_{av} without mask (rad m^{-2})
No threshold	-1 ± 2	-4 ± 2
$\Delta\phi < 10$ rad m^{-2}	-2.0 ± 0.6	-4 ± 1
$\Delta\phi < 5$ rad m^{-2}	-2.6 ± 0.4	-4.6 ± 0.7
Weighted average	-3.1 ± 0.5	-4.7 ± 0.6

Table 3.2: Mean Faraday depth as found in the South Galactic Pole

In this region the trend in the errors is what would be expected; as the thresholding increases, the errors go down. The average Faraday depth without masking has also been given here, but these values should be considered spurious. As with the NGP, the method which produces the most reliable average is to weight by uncertainty.

3.2 Comparison to Extra-Galactic Surveys

3.2.1 Introduction

Before the values of Faraday depth are used to compute magnetic field information, it is important to compare them to values obtained by alternative methods. The data best suited for this was presented in Mao et al. (2010), as discussed in Section 1.3. These data are two surveys of rotation measure (RM) in the North and South Galactic Poles using extra-Galactic sources. Using the l and b data provided with the RM values, the location of each source was found on the NGP and SGP DRAO Faraday depth maps. To do this it is assumed projection effects remain negligible; this is a reasonable assumption for high latitudes near the poles. Firstly, the polar map coordinates (r, θ) for a given (l, b) are found by:

$$\frac{r}{\text{pixels}} = \left(a\frac{b}{\text{deg}} + 90^\circ \right) \times \left(\frac{0.2}{\text{deg pixels}^{-1}} \right)^{-1} \tag{3.10}$$

Where $a = -1$ in the NGP and $a = +1$ in the SGP. Secondly:

$$\frac{\theta}{\text{rad}} = -\frac{l}{\text{deg}} \times \frac{\pi}{180^\circ} + \frac{3\pi}{2} \tag{3.11}$$

The Cartesian map coordinates (x, y) are simply given by:

$$x = \lfloor r\cos\theta + x_0 \rceil \tag{3.12}$$

and

$$y = \lfloor r\sin\theta + y_0 \rceil \tag{3.13}$$

Where (x_0, y_0) are the central pixel coordinates (101,101).

3.2.2 North Galactic Pole

Maps showing the Mao et al. (2010) RMs at their map coordinates in the NGP, as calculated above, are given in Figures 3.15 and 3.16. RMs that were excluded from analysis by Mao et al. (2010) were also excluded in these maps. The scatter of the RMs against the corresponding Faraday depth from the DRAO survey is given in Figure 3.17 with the accompanying histograms for each data set. The median uncertainty for the Mao et al. (2010) data is found from the error values they provided. This scatter plot reveals what was seen earlier; that the DRAO data contains some Faraday depth of high magnitudes that are certainly spurious. Before this is addressed directly, a different region can be analysed.

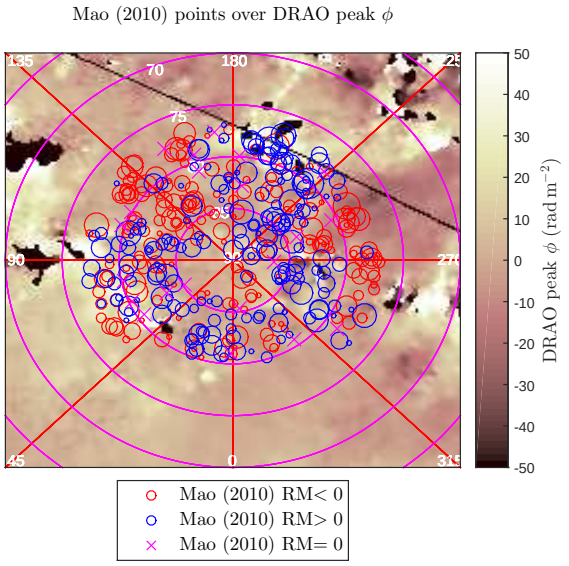

Figure 3.15: Map of Faraday depth in the NGP with Mao et al. (2010) *RM*s overlaid.

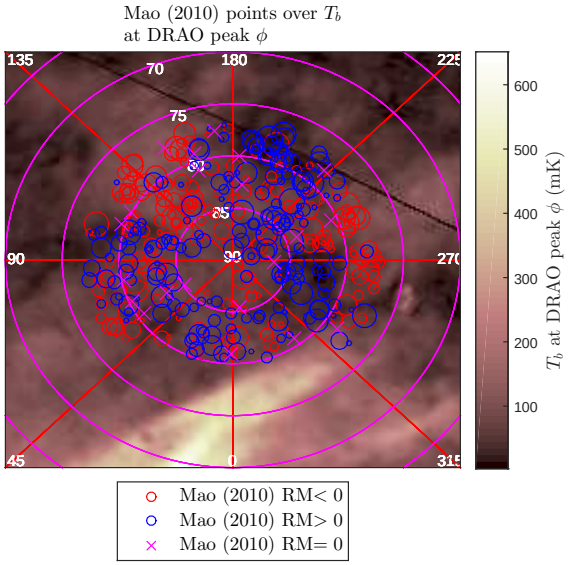

Figure 3.16: Map of polarised brightness temperature in the NGP with Mao et al. (2010) *RM*s overlaid.

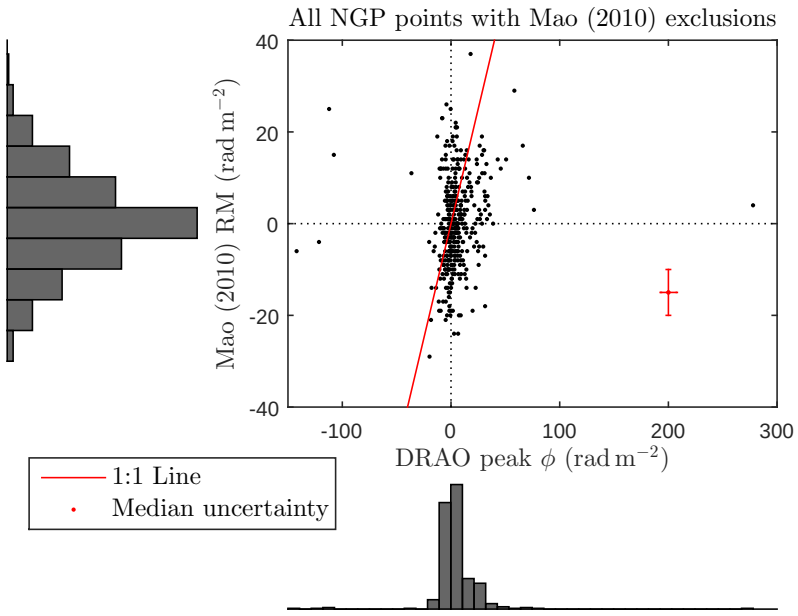

Figure 3.17: Scatter/histogram plot of Mao et al. (2010) *RM*s against their corresponding ϕ value from DRAO Faraday depth map in the NGP.

3.2.2.1 North Galactic Pole - North Polar Spur

Mao et al. (2010) identified *RM*s in their data that coincided with the NPS and excluded them from their analysis, but still included them in their data release. They can be used here, however, to compare with the Faraday depth values in the DRAO survey. This region provides a useful test for comparison as the NPS has such high polarised brightness that none of the Faraday depth is considered spurious. As before, maps of Faraday depth and polarised brightness temperature were computed showing the overlaid *RM*s. These are shown in Figures 3.18 and 3.19 respectively. Inspecting Figure 3.19 reveals that Mao et al. (2010) were possibly a little over cautious in their exclusions. There is a small cluster of *RM*s that do not appear to coincide with the NPS in the polarised emission data. This cluster is visible in Figure 3.17 as a secondary peak in the DRAO peak ϕ histogram. For the purposes of this analysis the *RM* given for $l = 314.34°$, $b = 77.42°$ was excluded as an outlier as it had rotation measure of $RM = 49 \pm 8\,\mathrm{rad\,m^{-2}}$.

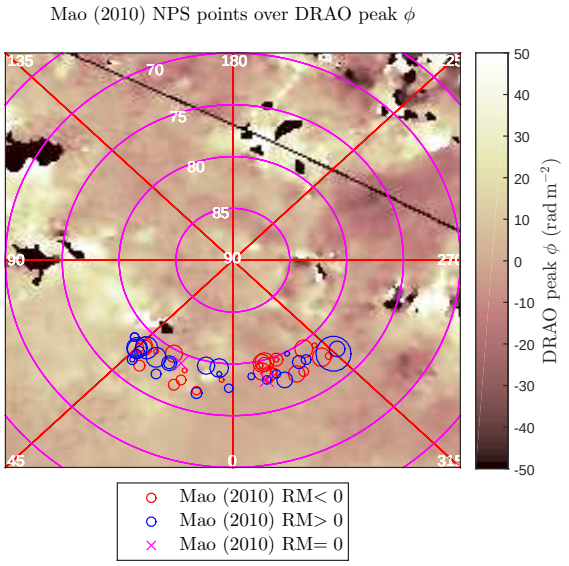

Figure 3.18: Map of Faraday depth in the NGP with Mao et al. (2010) *RM*s in the NPS overlaid.

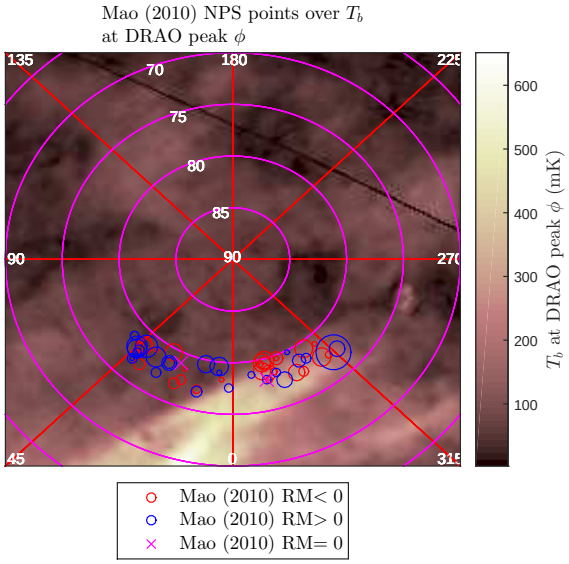

Figure 3.19: Map of polarised brightness temperature in the NGP with Mao et al. (2010) *RM*s in the NPS overlaid.

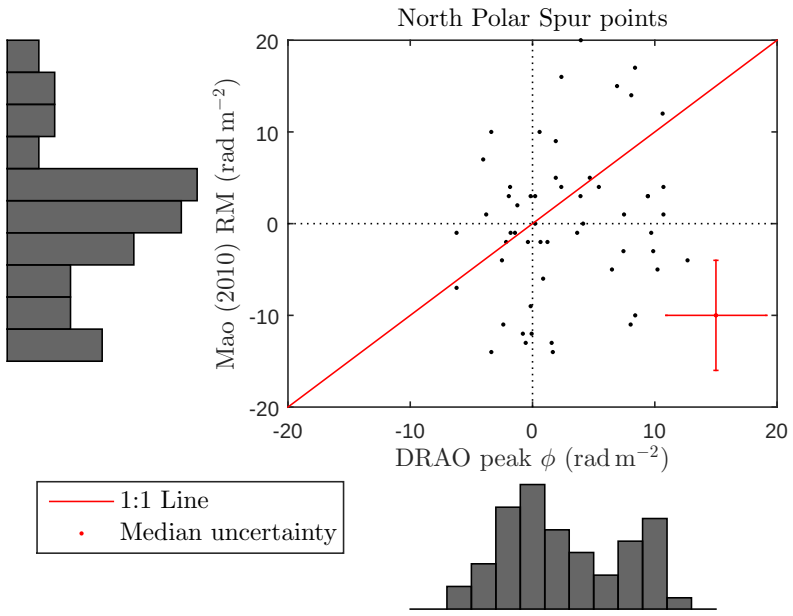

Figure 3.20: Scatter/histogram plot of Mao et al. (2010) *RM*s in the NPS against their corresponding ϕ value from DRAO Faraday depth map.

To exclude the *RM*s that fall outside of the NPS the threshold of uncertainty that was applied in the Faraday depth analysis can be used again. Applying the condition that $\Delta\phi < 5\,\mathrm{rad\,m^{-2}}$ restricts the data such that only the NPS is considered in this case. This can be confirmed by inspection of Figure 3.22, where all the *RM* points now lie clearly on the NPS. It can also be seen in Figure 3.23 that the secondary peak in the histogram of peak ϕ that was visible in Figure 3.20 is now gone.

Upon first inspection of the scatter shown in Figure 3.23 it is possible to think that the two data sets are totally unrelated. The two sets are certainly not correlated point-for-point, with a linear regression producing an $R^2 = 0.00015$, but they are not necessarily expected to be. This is because processes that causes variance in each data set are very different. In the extra-Galactic data, variance is due to the intrinsic rotation measure of the source, and any rotation that occurs out to that source, being different from point to point. In the continuum data variation arises due to fluctuations in diffuse polarised emission, with low polarised emissions producing large variations in Faraday depth. As such, in a given small region, if the two data sets are measuring the same value, a scatter around that value should be seen. Indeed this is what is shown in Figure 3.23; a scatter around a value near $0\,\mathrm{rad\,m^{-2}}$.

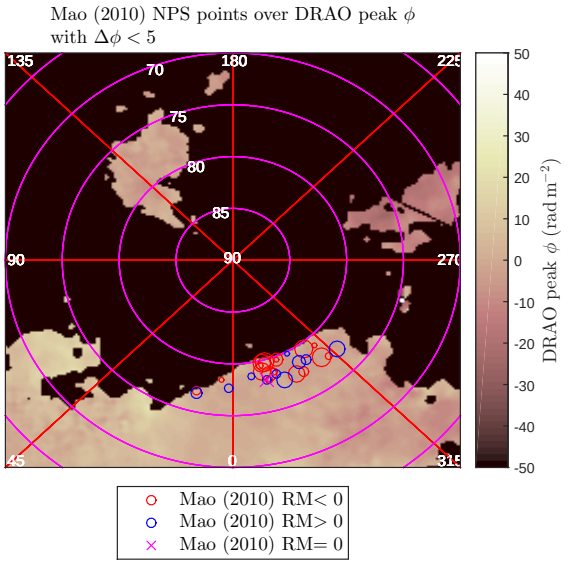

Figure 3.21: Map of Faraday depth in the NGP with Mao et al. (2010) *RM*s in the NPS overlaid.

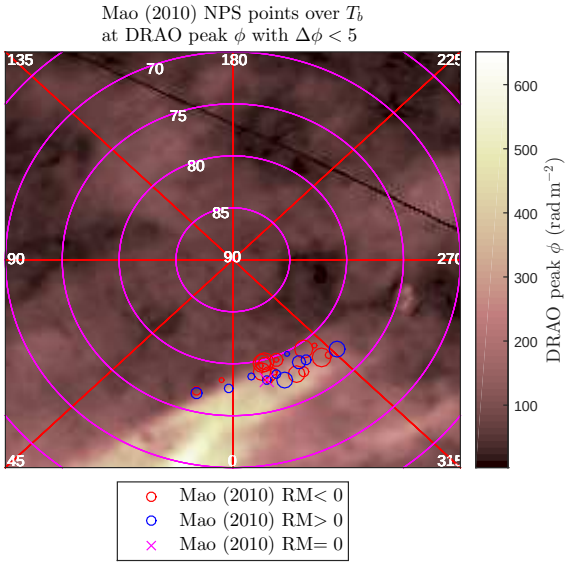

Figure 3.22: Map of polarised brightness temperature in the NGP with Mao et al. (2010) *RM*s in the NPS overlaid.

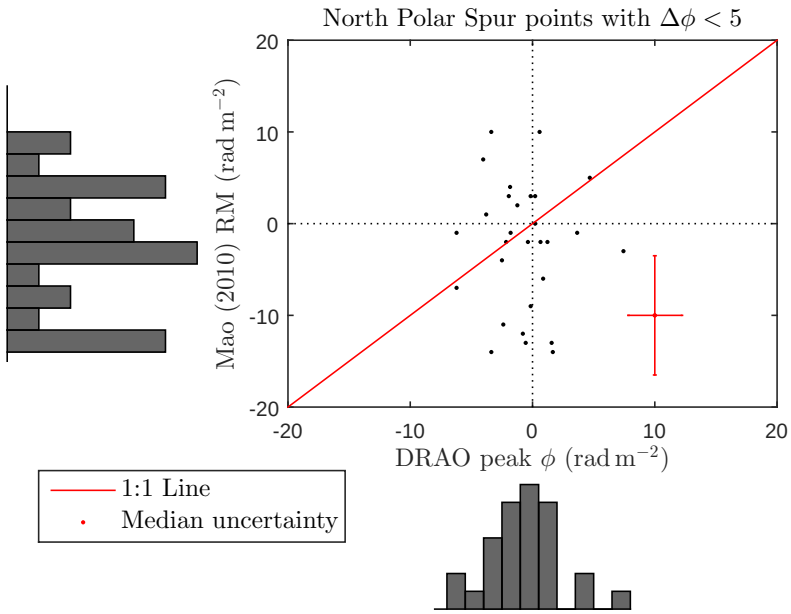

Figure 3.23: Scatter/histogram plot of Mao et al. (2010) *RM*s in the NPS against their corresponding ϕ value from DRAO Faraday depth map with $\Delta\phi < 5\,\mathrm{rad\,m^{-2}}$.

3.2.2.2 North Galactic Pole - Excluding North Polar Spur

Returning attention to the larger NGP region, the method of thresholding can be applied too. First, applying a threshold of $\Delta\phi < 10\,\mathrm{rad\,m^{-2}}$ (Figure 3.26) removes much of high magnitude scatter shown in Figure 3.17. The accompanying maps in Figures 3.24 and 3.25 show, however, that some of the points are still overlaid on spurious regions. This can also be seen in Figure 3.26, where the scatter above $\phi \approx 20\,\mathrm{rad\,m^{-2}}$ is certainly a side-lobe in the corresponding histogram.

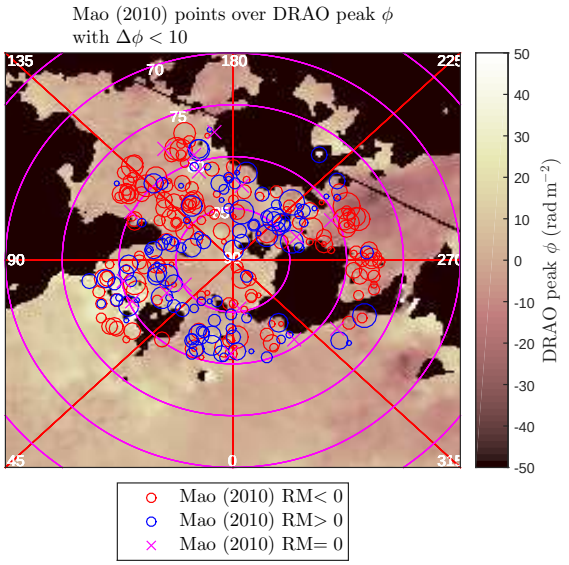

Figure 3.24: Map of Faraday depth in the NGP with $\Delta\phi < 10\,\mathrm{rad\,m^{-2}}$ and Mao et al. (2010) RMs overlaid.

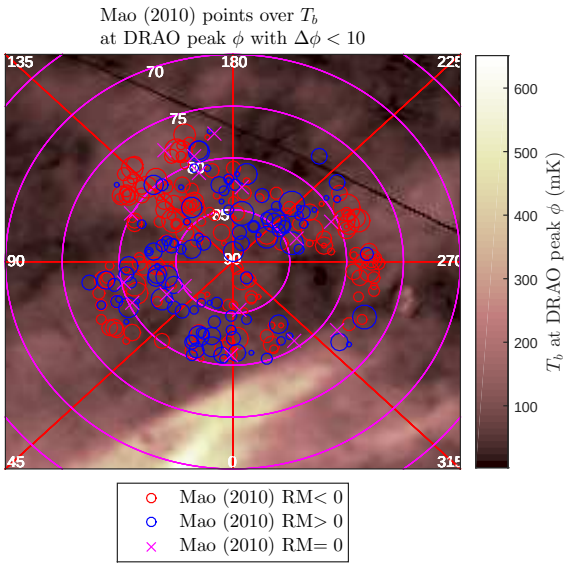

Figure 3.25: Map of polarised brightness temperature in the NGP with $\Delta\phi < 10\,\mathrm{rad\,m^{-2}}$ and Mao et al. (2010) RMs overlaid.

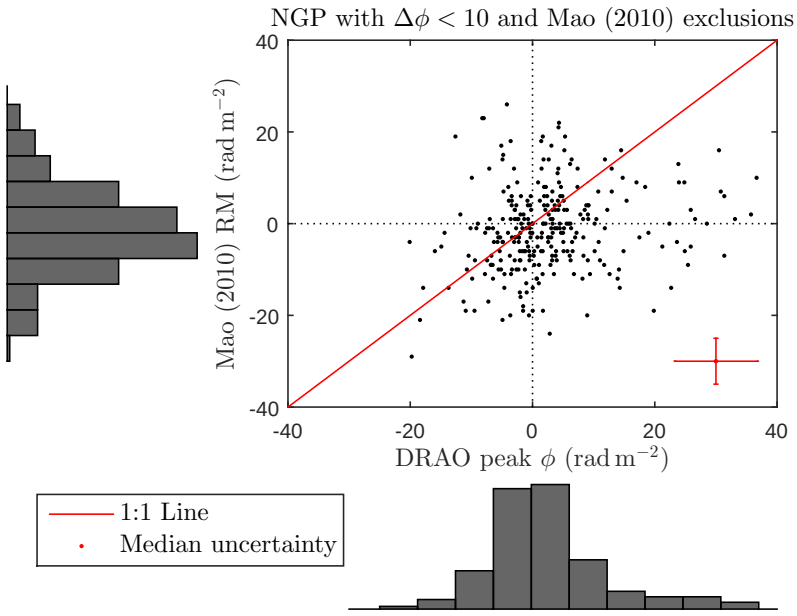

Figure 3.26: Scatter/histogram plot of Mao et al. (2010) *RM*s in the NGP against their corresponding ϕ value from DRAO Faraday depth map with $\Delta\phi < 10\,\mathrm{rad\,m^{-2}}$.

Applying a harder threshold of $\Delta\phi < 5\,\mathrm{rad\,m^{-2}}$ leaves only the regions that have the strongest polarised emission. Unfortunately, the Mao et al. (2010) data does not cover the full NGP region as shown in Figures 3.27 and 3.28. What Figure 3.27 shows, though, is that the regions that are primarily negative in ϕ are associated with negative detections in *RM*. This is demonstrated in Figure 3.29 as well, where the scatter appears to have much better correlation. In that negative *RM* is associated with negative ϕ. What is also clear is that the peak in each distribution is also in agreement.

The average value of rotation measure quoted in Mao et al. (2010) for the NGP is $0.0 \pm 0.5\,\mathrm{rad\,m^{-2}}$. The average Faraday depth found using a method of weighted averaging was found here to be $0.1 \pm 0.6\,\mathrm{rad\,m^{-2}}$. This, in conjunction with the point-for-point comparisons above, means that it is possible to conclude that the same value of Faraday depth has been detected for the North Galactic pole in the DRAO survey and the Mao et al. (2010) survey. This has important ramifications for considerations of the magnetic field in this region, which will be discussed in Chapter 4.

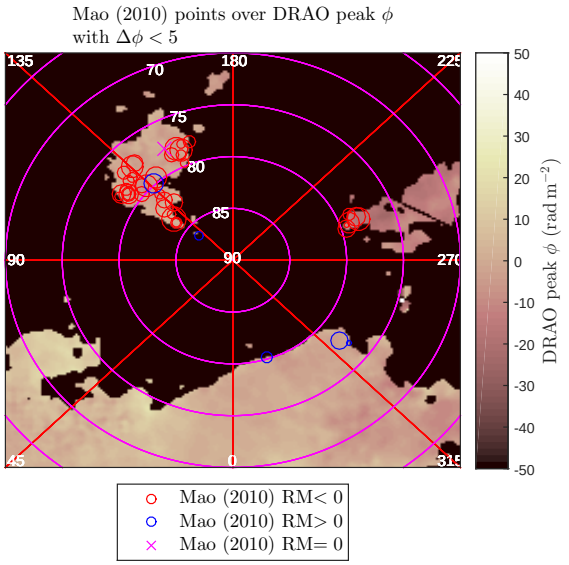

Figure 3.27: Map of Faraday depth in the NGP with $\Delta\phi < 5\,\mathrm{rad\,m^{-2}}$ and Mao et al. (2010) RMs overlaid.

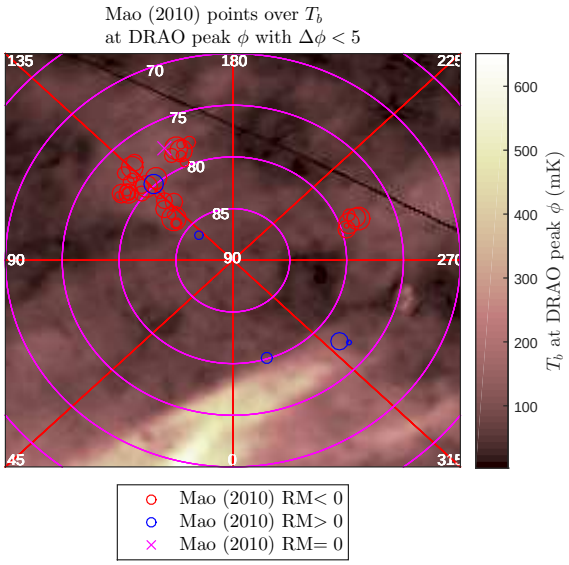

Figure 3.28: Map of polarised brightness temperature in the NGP with $\Delta\phi < 5\,\mathrm{rad\,m^{-2}}$ and Mao et al. (2010) RMs overlaid.

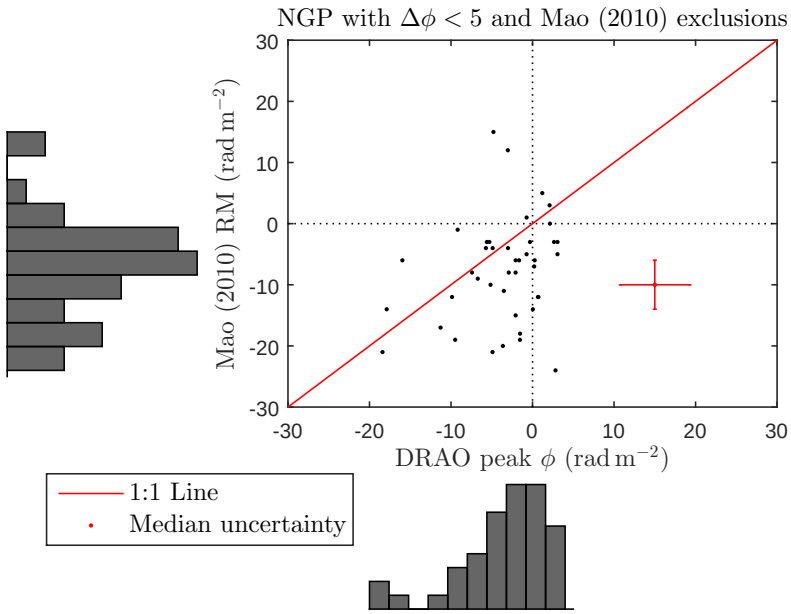

Figure 3.29: Scatter/histogram plot of Mao et al. (2010) *RM*s in the NGP against their corresponding ϕ value from DRAO Faraday depth map with $\Delta\phi < 5\,\mathrm{rad\,m^{-2}}$.

3.2.3 South Galactic Pole

The same comparative analysis that has been applied in the NGP can also be applied in the SGP. Again, the issue in this region is that so much data missing. Figures 3.30 and 3.31 show where *all* the Mao et al. (2010) *RM*s lie in the SGP. Comparing these maps with Figures 3.32 and 3.33 shows that a little under half of the Mao et al. (2010) points must be discarded from comparison in the SGP. Additionally, these maps show immediately that the majority of the *RM* values in this region are positive blue circles. This trend is seen in Figure 3.34 too; the histogram of *RM* is clearly peaked to positive values. The width in the peak of ϕ is very broad, meaning spurious values are certainly being shown. These values have been shown to be associated with striping and low polarised emission; each of these problems will be dealt with in turn.

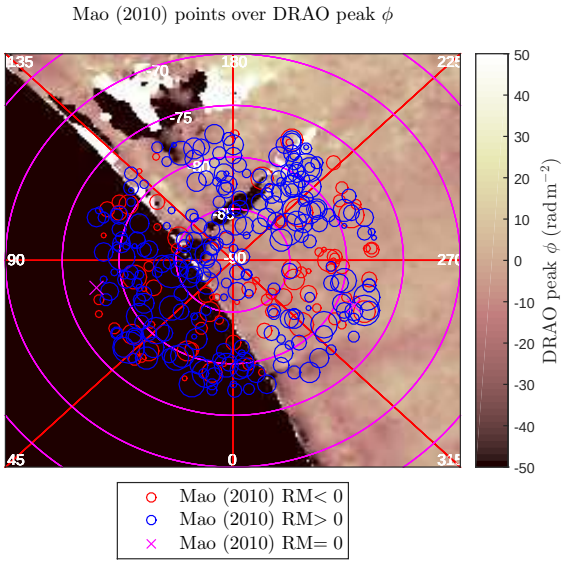

Figure 3.30: Map of Faraday depth in the SGP with *all* Mao et al. (2010) *RM*s overlaid.

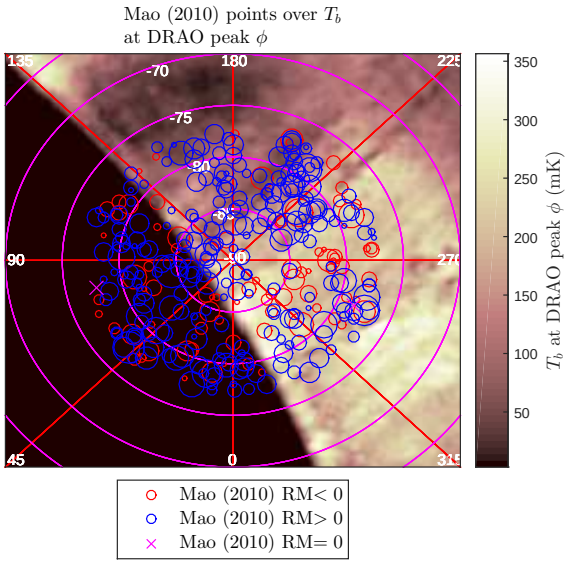

Figure 3.31: Map of polarised brightness temperature in the SGP with *all* Mao et al. (2010) *RM*s overlaid.

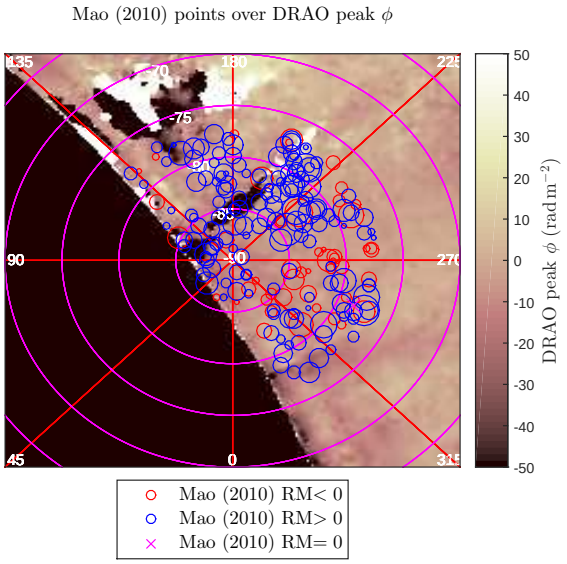

Figure 3.32: Map of Faraday depth in the SGP with Mao et al. (2010) *RM*s overlaid.

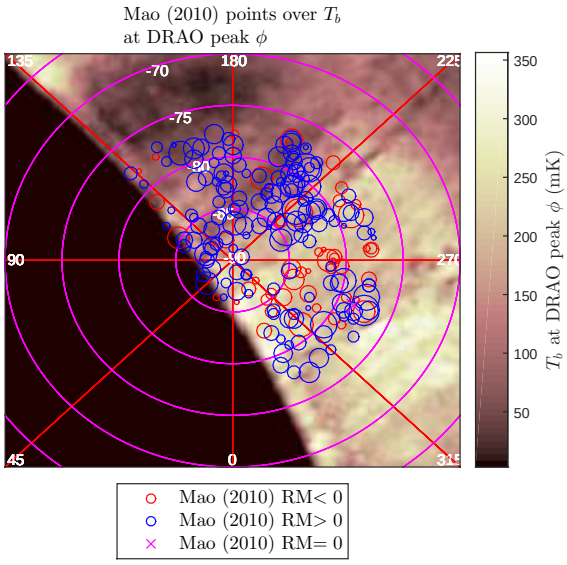

Figure 3.33: Map of polarised brightness temperature in the SGP with Mao et al. (2010) *RM*s overlaid.

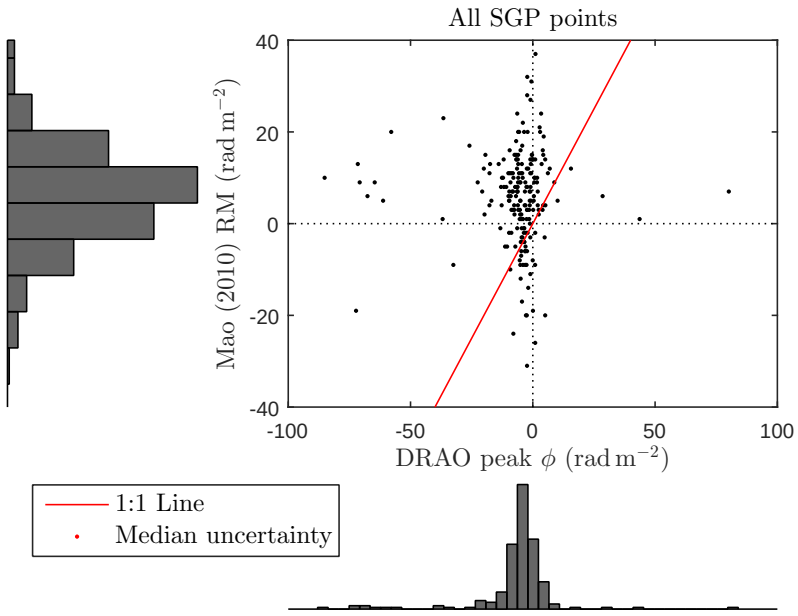

Figure 3.34: Scatter/histogram plot of Mao et al. (2010) *RM*s in the SGP against their corresponding ϕ value from DRAO Faraday depth map.

3.2.3.1 South Galactic Pole - Masked

Masking the obvious scanning effects in the SGP has a significant effect on the comparison with the *RM* data. Firstly, the number of points being compared has been significantly reduced; as is shown in Figures 3.35 and 3.36. Secondly, but perhaps more importantly, the scatter in Figure 3.37 shows considerable improvement. The tails have almost been completely removed in the DRAO histogram.

Thresholding by $\Delta\phi < 10\,\mathrm{rad\,m^{-2}}$ does not appear to make an improvement to the distribution shown in Figure 3.40. This is not the fault of the technique, however. Inspecting Figures 3.38 and 3.39 reveals that the threshold, by coincidence, only removed data above the $l = -77°$ boundary of the Mao et al. (2010) data.

Applying the stronger threshold of $\Delta\phi < 5\,\mathrm{rad\,m^{-2}}$, it can be seen in Figures 3.41 and 3.42 that the threshold is now having an effect. Thus, in Figure 3.43 it is clear the majority of spurious data has been removed from comparison.

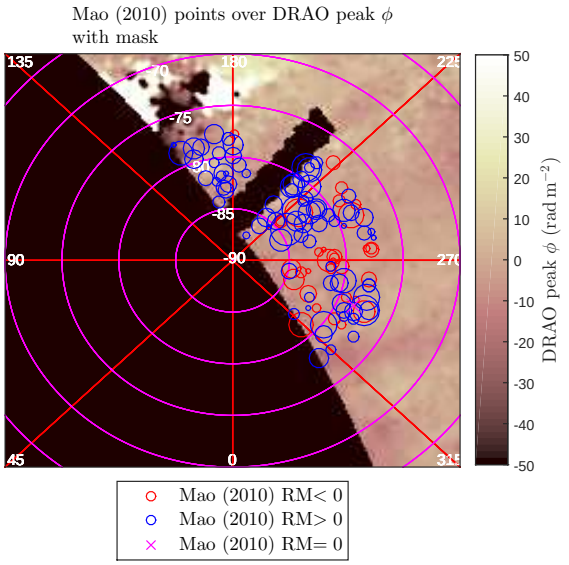

Figure 3.35: Map of Faraday depth in the SGP with masking and Mao et al. (2010) RMs overlaid.

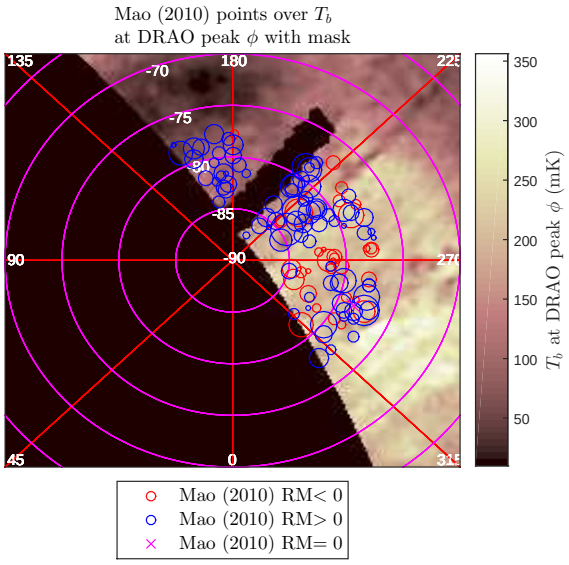

Figure 3.36: Map of polarised brightness temperature in the SGP with masking and Mao et al. (2010) RMs overlaid.

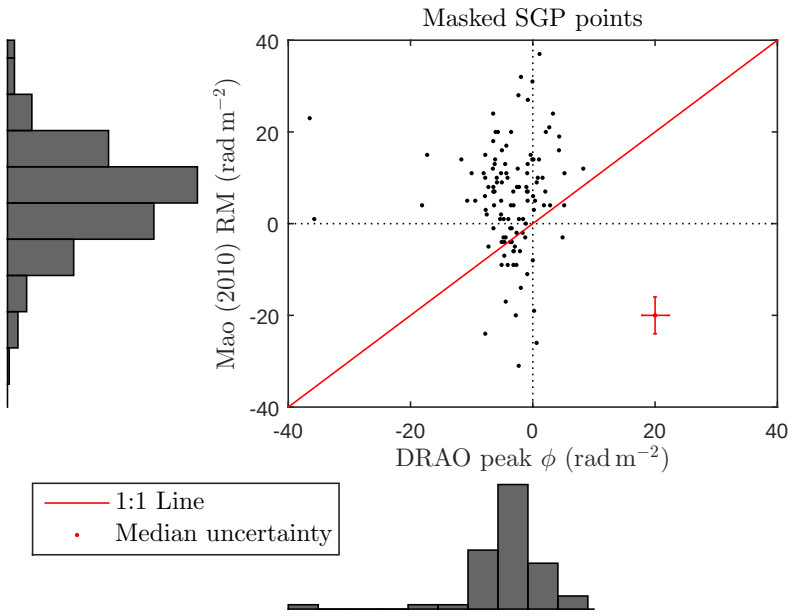

Figure 3.37: Scatter/histogram plot of Mao et al. (2010) *RM*s in the SGP against their corresponding ϕ value from DRAO Faraday depth map with masking.

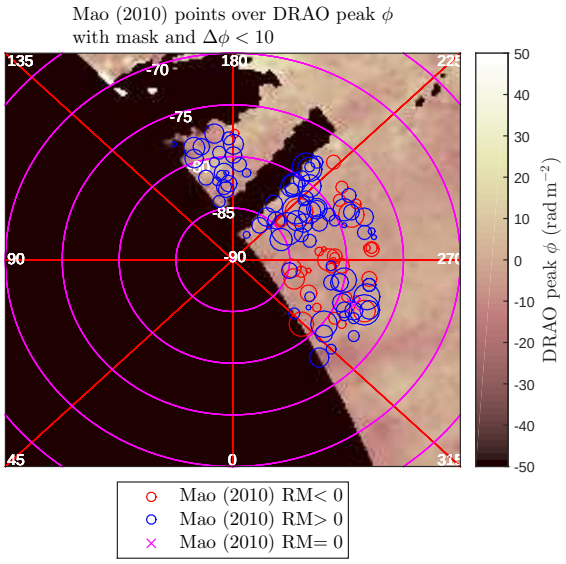

Figure 3.38: Map of Faraday depth in the SGP with masking, $\Delta\phi < 10\,\mathrm{rad\,m^{-2}}$ and Mao et al. (2010) *RM*s overlaid.

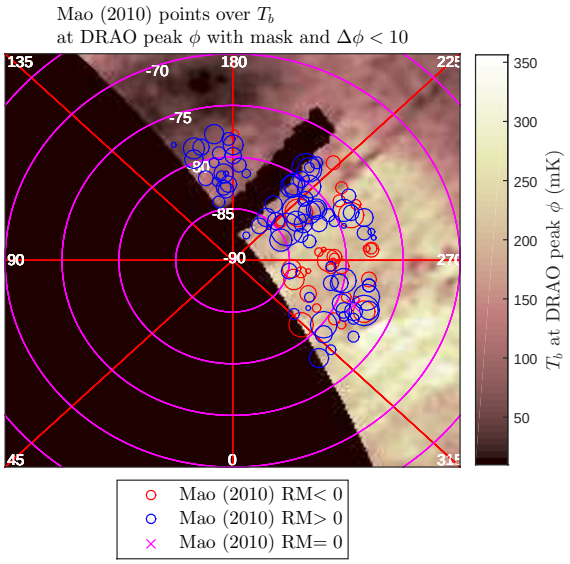

Figure 3.39: Map of polarised brightness temperature in the SGP with masking, $\Delta\phi < 10\,\mathrm{rad\,m^{-2}}$ and Mao et al. (2010) *RM*s overlaid.

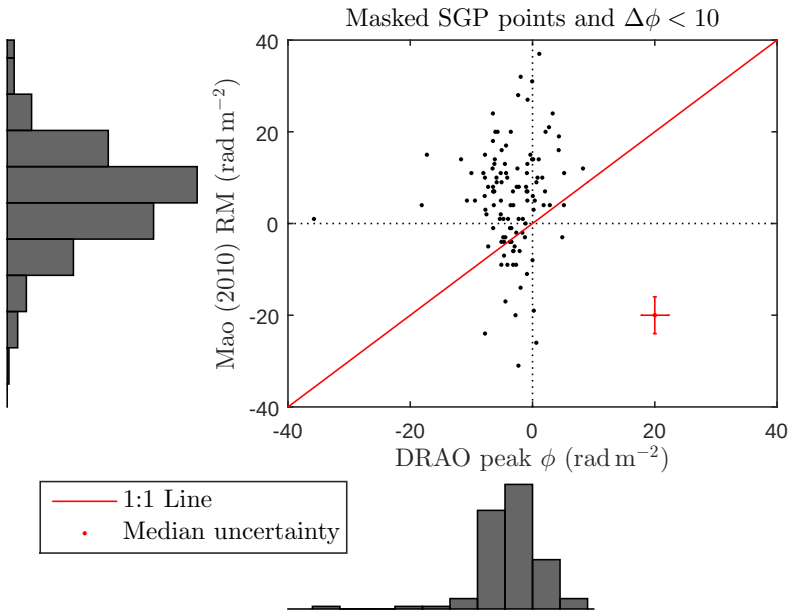

Figure 3.40: Scatter/histogram plot of Mao et al. (2010) *RM*s in the SGP against their corresponding ϕ value from DRAO Faraday depth map with $\Delta\phi < 10\,\mathrm{rad\,m^{-2}}$.

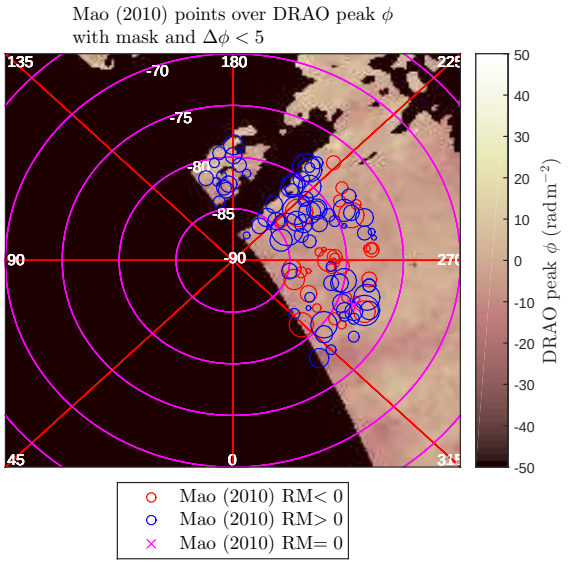

Figure 3.41: Map of Faraday depth in the SGP with $\Delta\phi < 5\,\mathrm{rad\,m^{-2}}$ and Mao et al. (2010) *RM*s overlaid.

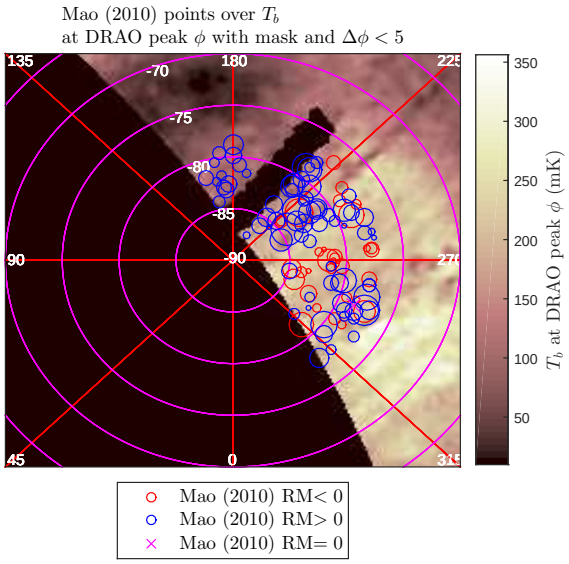

Figure 3.42: Map of polarised brightness temperature in the SGP with $\Delta\phi < 5\,\mathrm{rad\,m^{-2}}$ and Mao et al. (2010) *RM*s overlaid.

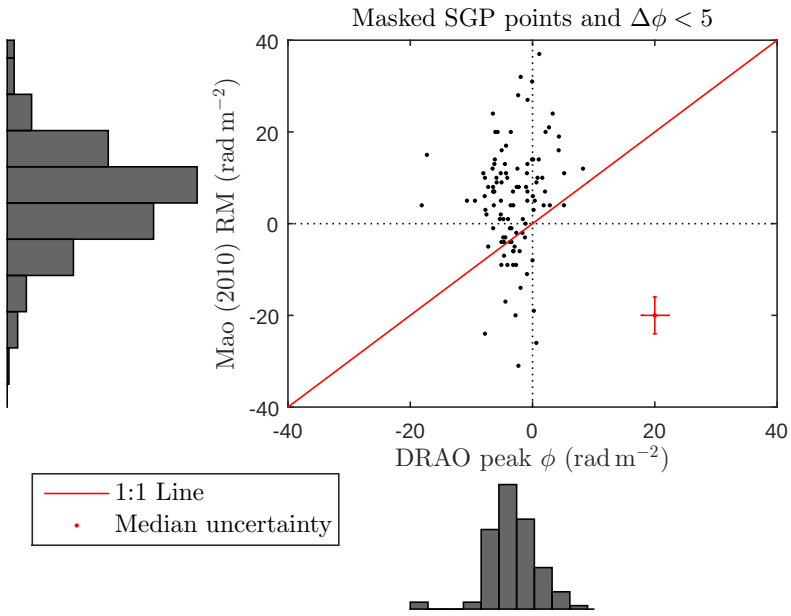

Figure 3.43: Scatter/histogram plot of Mao et al. (2010) *RM*s in the SGP against their corresponding ϕ value from DRAO Faraday depth map with $\Delta\phi < 5\,\mathrm{rad\,m^{-2}}$.

The scatter shown in Figure 3.43 reveals a very interesting result. Again, the data is not correlated, but, as before, these two data sets are not expected to correlate point-for-point. Instead, a scatter around the value detected in each region is shown. As the errors in the thresholded DRAO data are less on average than the errors in *RM* data, the distribution in the Mao et al. (2010) data is more broad by comparison. This causes the scatter to appear more vertical in Figure 3.43. Finally, the peak in each distribution is now around a different point. This is reflected in the mean values for each data set. Mao et al. (2010) found for the SGP a mean rotation measure of $+6.3 \pm 0.7\,\mathrm{rad\,m^{-2}}$, whereas the method of weighted averaging on the DRAO data gave a Faraday depth of $-3.1 \pm 0.2\,\mathrm{rad\,m^{-2}}$.

Bear in mind that that Mao et al. (2010) used extra-Galactic point sources to compute rotation measures. That method computes the rotation measure along the *entire* line of sight out to the extra-Galactic source. It is then assumed that the intrinsic variation from source to source will average out given enough measurements in a given region. The DRAO 26 m survey, however, measured diffuse polarised emission. In such a survey the telescope will measure polarised emission out as far as the brightest emission for a line of sight. As such, if the two surveys give a different value for a given region that necessarily means that the the diffuse polarised emission is local. That is, there must be additional magneto-ionic medium in the interstellar medium behind what was detected in the DRAO survey. By 'local', it is meant that the emission must be between the position of the Sun

and the Southern edge of the Galactic Halo.

Despite the fact that the DRAO survey does not provide an entire view of the SGP region two important factors have been determined. First, the emission detected is certainly local; this will have important ramifications when considering the magnetic field in this region. Second, the data that is provided in this region is overall of high polarised intensity. This has allowed for the computation of a mean Faraday depth in the portion of the SGP present and thus magnetic field information can be determined.

Chapter 4

Magnetic Fields

4.1 Magnetic Fields - Introduction

As discussed in Section 1.3, computation of the vertical magnetic field in each pole is possible using the method outlined in Mao et al. (2010). This method, in particular Equation 1.56, required that the Faraday depth should be averaged around evenly in Galactic longitude. In the DRAO survey, however, it is not possible to sample evenly in longitude in both regions. In both the NGP and SGP there are areas where the polarised emission is low enough that spurious values in Faraday depth are produced. In the SGP, the location of the telescope in the Northern Hemisphere resulted in approximately half of the region not being observed. Additionally, the required masking of the scanning effects further reduced the amount of available data. The result of all of these factors is that the method of Mao et al. (2010) to compute the vertical magnetic field cannot be applied to these data.

Whilst this is unfortunate, this does not mean that magnetic field information cannot be evaluated. Recall from Equation 1.48 that dispersion measure (DM) gives the integral of electron density along the line of sight. Combining Equations 1.20 and 1.48 the average magnetic field magnitude ($\langle B \rangle$) can be found from the average Faraday depth:

$$\langle B \rangle = \frac{|\phi_{\rm av}|}{0.81 DM} \tag{4.1}$$

Where $B = |\mathbf{B}|$ in μG and dispersion measure is in $\mathrm{pc\,cm^{-3}}$. What is needed to implement this equation is a model of electron density distribution out from the Galactic plane. Such a model is presented in Gaensler et al. (2008). They provide fit parameters to the model as found by combining both emission measure (see Section 1.3) and dispersion measure observations. The model used is the same exponential distribution as used by Mao et al. (2010), shown in Equation 1.54. The parameters given by Gaensler et al. (2008) are as follows: the mid-plane electron density $n_{e0} = 0.014 \pm 0.001\,\mathrm{cm^{-3}}$ and the scale height of free electrons is $H_0 = 1830^{+120}_{-250}\,\mathrm{pc}$. This model and its parameters can be substituted into Equation 1.48:

$$\begin{aligned} DM &= \int_0^{z_0} n_e dz \\ &= \int_0^{z_0} n_{e0} \exp\left(\frac{-z}{H_0}\right) dz \\ &= n_{e0} \left[-H_0 \exp\left(\frac{-z}{H_0}\right) \right]_0^{z_0} \end{aligned}$$

$$\therefore DM = n_{e0} H_0 \left[1 - \exp\left(\frac{-z_0}{H_0}\right) \right] \tag{4.2}$$

Where z is the distance along the line of sight towards each pole and z_0 is the distance to the observed polarised emission, both of which are in pc. This equation

will hold so long as it is applied to observations near the Galactic poles. Observations away from the poles have an increased distance factor of $1/\sin b$, whereas near the poles if $\theta = 90° - b$ then the distance factor becomes $1/\cos\theta \approx 1$.

Thus, by combining Equations 4.1 and 4.2 the magnetic field can be evaluated. There is a limitation to this method, however. The distance to the observed emission (z_0) is not known. In the absence of additional data, only reasonable estimates can be made of this parameter. Vertical distances between 100 pc and 2 kpc are used here to obtain a magnetic field strength. The scale height of free electrons was taken to be $H_0 \approx 1.8$ kpc and the mid-plane electron density used was $n_{e0} \approx 0.014\,\mathrm{cm}^{-3}$.

4.2 Magnetic Fields - North Galactic Pole

The average Faraday depths in the NGP were found to be $1.2 \pm 0.3\,\mathrm{rad\,m}^{-2}$ and $0.1 \pm 0.6\,\mathrm{rad\,m}^{-2}$ with and without the NPS respectively. The magnetic field magnitudes shown in Figures 4.1 and 4.2 show a significant difference. It is possible to conclude from this that away from the NPS there is no detected mean radial magnetic field in the NGP. This is also shown in Table 4.1, where a few select distances and the associated magnetic field magnitudes are given for the NGP.

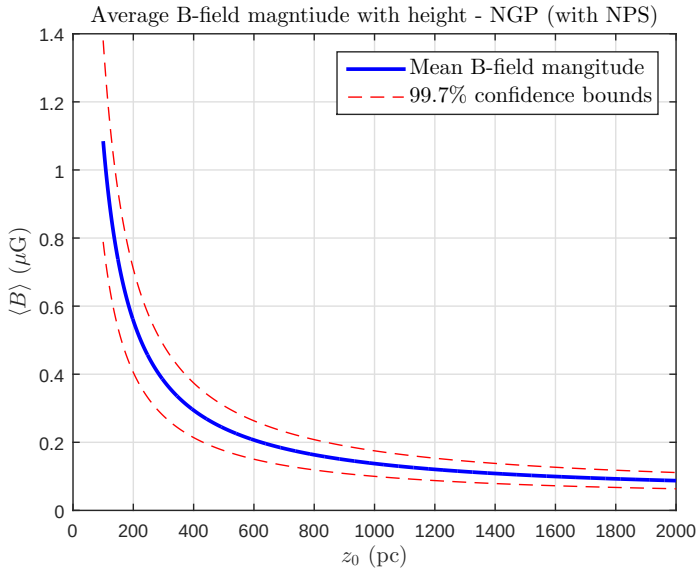

Figure 4.1: Magnetic field magnitude (μG) as a function of distance to the emission averaged over the entire NGP.

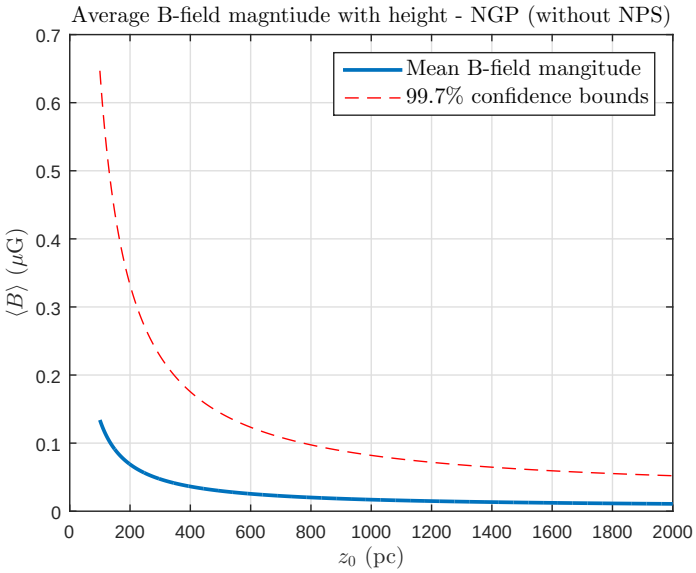

Figure 4.2: Magnetic field magnitude (μG) as a function of distance to the emission source averaged over the NGP with the NPS excluded.

z_0 (pc)	B (μG) - NGP	B (μG) - NGP (no NPS)
100	1.1 ± 0.3	0.1 ± 0.5
300	0.4 ± 0.1	0.0 ± 0.2
500	0.24 ± 0.07	0.0 ± 0.1
1000	0.14 ± 0.04	0.02 ± 0.07

Table 4.1: Mean Faraday depth as found in the North Galactic Pole

4.2.1 Trend in Faraday Depth

Along with having a mean magnetic field magnitude near $B \approx 0\,\mu$G, the error range in Figure 4.2 is very large. Recall from Section 3.1.2 that a trend was found in the distribution of Faraday depth across the NGP region. This trend can again be seen in Figure 4.3. In this map the three primary contributing regions that produce this trend have been identified. Maps that focus on each of these regions are given in Figures 4.4, 4.5 and 4.6. The mean Faraday depth for regions A, B and C are $\phi_{\mathrm{A}} = 6 \pm 1\,\mathrm{rad\,m^{-2}}$, $\phi_{\mathrm{B}} = -2.0 \pm 0.8\,\mathrm{rad\,m^{-2}}$ and $\phi_{\mathrm{C}} = -14 \pm 3\,\mathrm{rad\,m^{-2}}$ respectively.

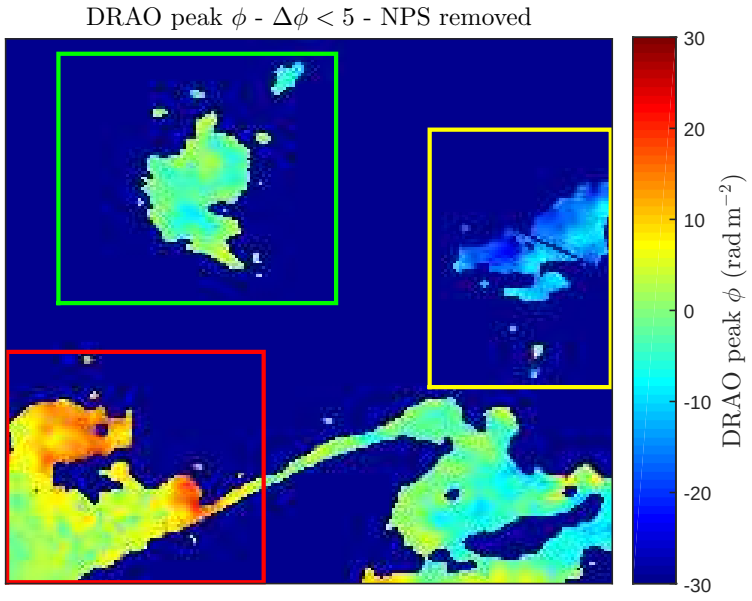

Figure 4.3: Map of Faraday depth in the NGP with $\Delta\phi < 5\,\mathrm{rad\,m^{-2}}$. Three sub-regions are identified; region A - red, region B - Green, region C - yellow.

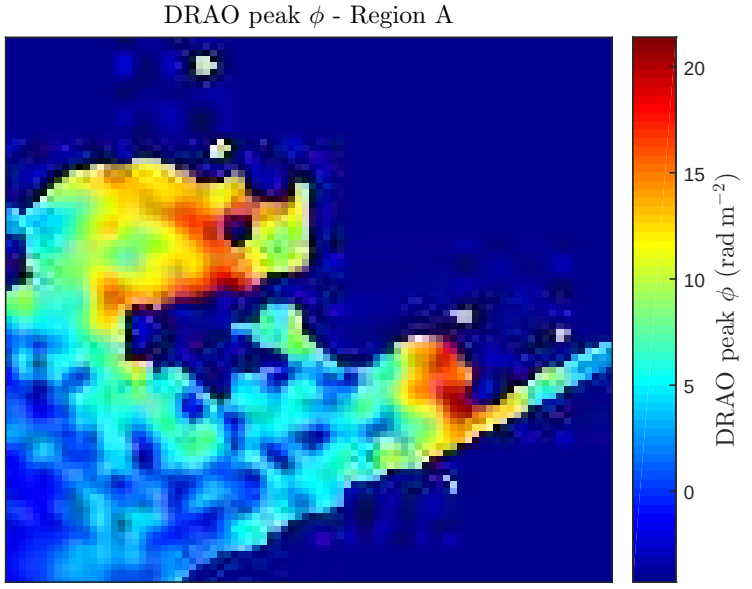

Figure 4.4: Map of Faraday depth in region A.

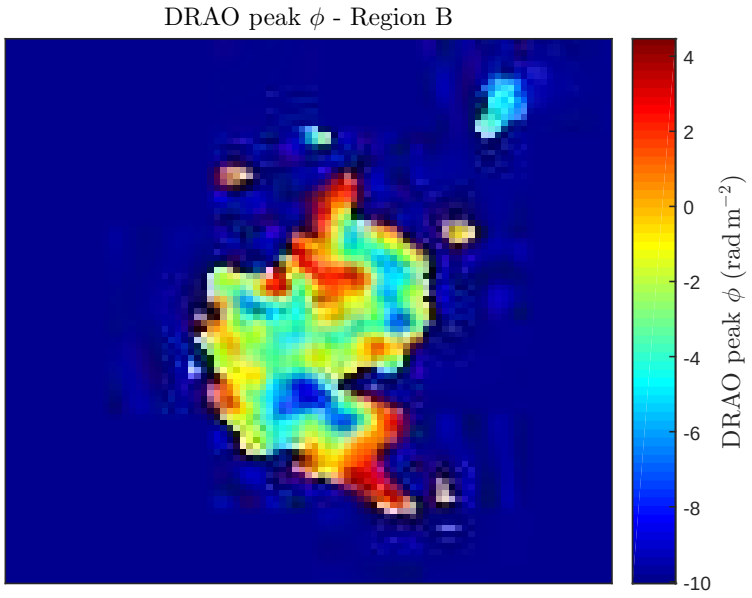

Figure 4.5: Map of Faraday depth in region B.

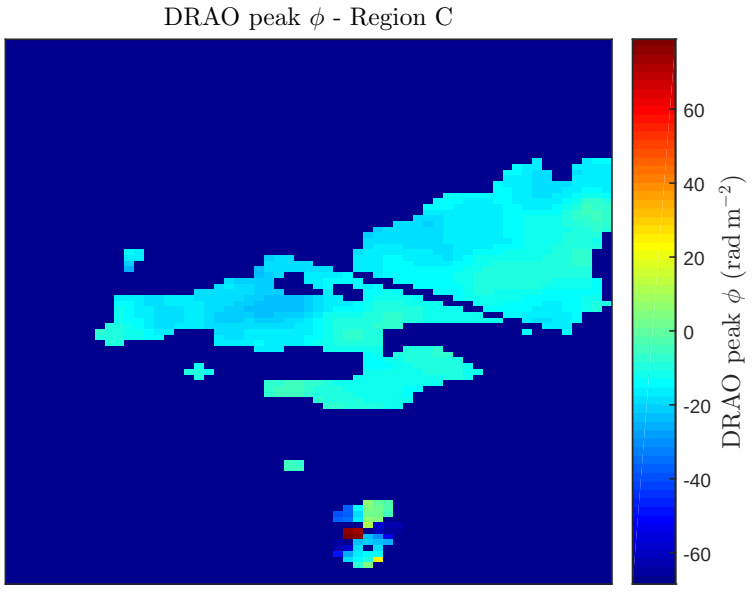

Figure 4.6: Map of Faraday depth in region C.

As before, magnetic field magnitudes can be computed for each region as a function of distance to the emission. These magnitudes are shown in Figures 4.7, 4.8 and 4.9, for regions A, B and C respectively. Additionally, select values of magnetic field magnitudes are given in Table 4.2 for these regions. It is important to bear in mind that a field reversal occurs from region A to region B and C. Without additional analysis it is not possible to discern whether this reversal occurs in the horizontal or vertical field component.

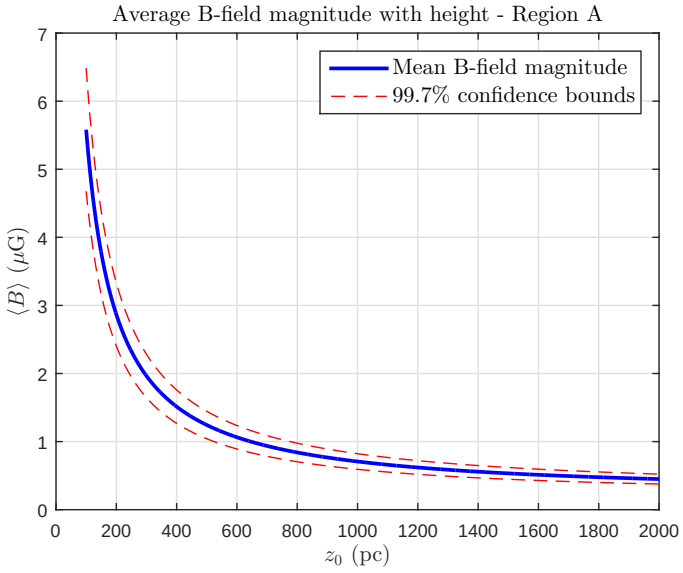

Figure 4.7: Magnetic field magnitude (μG) as a function of distance to the emission averaged over region A.

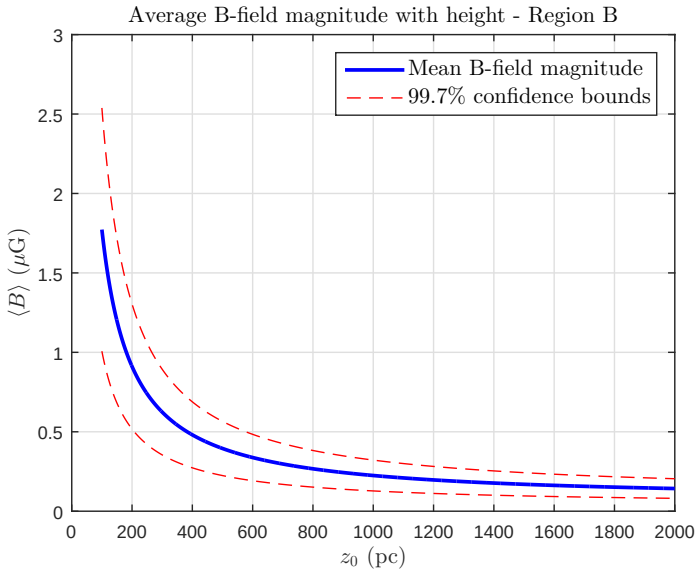

Figure 4.8: Magnetic field magnitude (μG) as a function of distance to the emission averaged over region B.

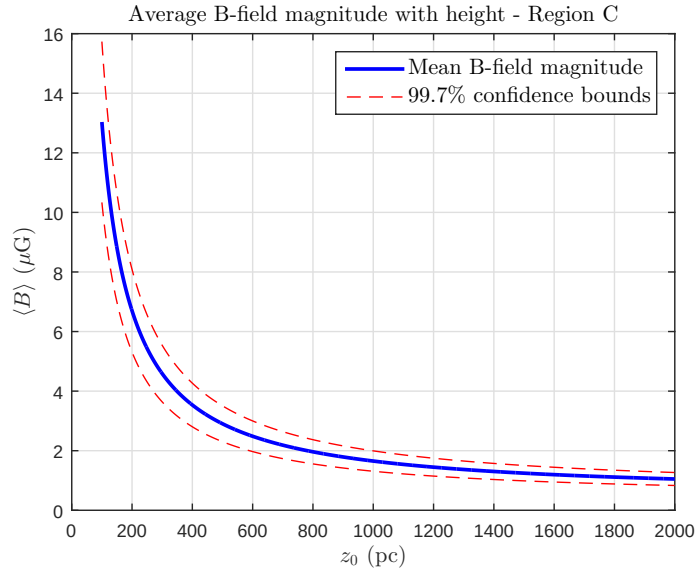

Figure 4.9: Magnetic field magnitude (μG) as a function of distance to the emission averaged over region C.

z_0 (pc)	B (μG) - A	B (μG) - B	B (μG) - C
100	5.6 ± 0.9	1.8 ± 0.8	13 ± 3
300	2.0 ± 0.3	0.6 ± 0.3	5 ± 1
500	1.2 ± 0.2	0.4 ± 0.2	2.9 ± 0.6
1000	0.7 ± 0.1	0.2 ± 0.1	1.7 ± 0.3

Table 4.2: Mean Faraday depth as found in regions of the North Galactic Pole

As direction information has not yet been found for the magnetic fields in these regions it not possible to confirm whether the field pattern matches a theoretical model; such as a dipole or quadrupole (Figure 1.5). Thus, if the vertical and horizontal field can be differentiated, this data can be used to gain information on the large scale Galactic magnetic field in the North Galactic Polar region at least.

4.3 Magnetic Fields - South Galactic Pole

Recall that the average Faraday depth in the SGP was found to be $3.1 \pm 0.2\,\mathrm{rad\,m^{-2}}$. For the area of the SGP above a declination of $\delta = -30°$ the mean magnetic field magnitude has been found. Figure 4.10 shows the magnetic field magnitude as a function of distance to the emission.

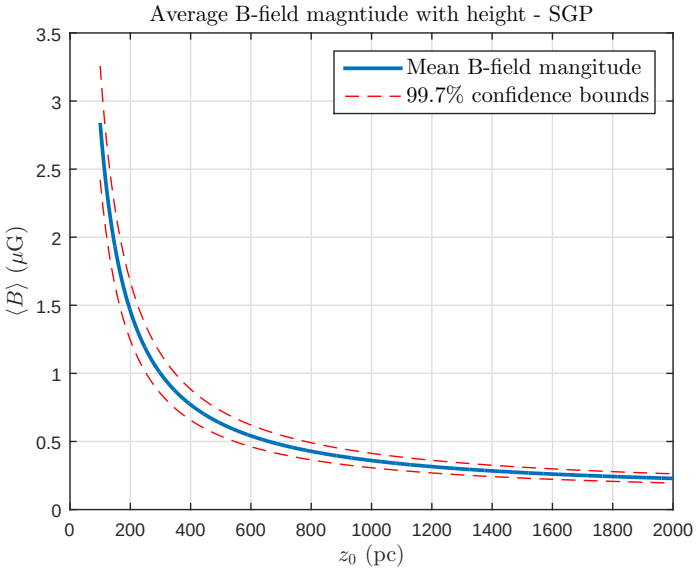

Figure 4.10: Magnetic field magnitude (μG) as a function of distance to the emission averaged over region the SGP.

z_0 (pc)	B (μG) - NGP
100	2.8 ± 0.4
300	1.0 ± 0.1
500	0.63 ± 0.09
1000	0.36 ± 0.05

Table 4.3: Mean Faraday depth as found in the South Galactic Pole

The magnitude found here is much higher than what is found in the NGP on average, but not as high as the individual regions in the NGP at the same height intervals. The SGP emission, however, has been determined to be local. There is no reason to suppose that the regions in the NGP are the same distance away as the emission observed in the SGP. If the NGP regions are further away two factors should be considered when comparing values between the NGP and SGP. First as per Equations 4.1 and 4.2, a greater distance to the emission corresponds to a weaker magnetic field value. Second, a greater distance to an emission region means that more of the magneto-ionic medium in front of the emission has contributed to the Faraday depth detection.

With the current data available it is not possible to compare the magnetic field information to a theoretical structure. To do this the following additional information is required:

1. A full view of both poles
2. Distance to the emission regions
3. Separation of vertical and horizontal magnetic field components

Items 1. and 2. and 3. would require additional data to obtain and additionally item 3. could not be completed within time constraints of this project.

Chapter 5

Angular Structure

5.1 Two-dimensional Autocorrelation

For a given $(X \times Y)$ array, such as an image, the discrete two-dimensional autocorrelation function (ACF) is defined as follows:

$$\mathrm{ACF}(\Delta x, \Delta y) = \sum_{x=0}^{X-1} \sum_{y=0}^{Y-1} f(x,y)\bar{f}(x+\Delta x, y+\Delta y) \tag{5.1}$$

Where (x, y) is a given coordinate on the image f and the 'lag' $(\Delta x, \Delta y)$ samples the image space:

$$\begin{aligned} -(X-1) \leq \Delta x \leq (X-1) \\ -(Y-1) \leq \Delta y \leq (Y-1) \end{aligned} \tag{5.2}$$

The resultant ACF is another array of size $((2X-1) \times (2Y-1))$. Qualitatively, this function gives the correlation between point (x, y) and point $(x+\Delta x, y+\Delta y)$ on the image. The ACF will always have a peak around $(\Delta x, \Delta y) = (0, 0)$, as any given point will always be maximally correlated with itself. How the ACF decays away from the peak is dependent on the structure of the image. The rate at which the function decays can be used to ascertain the typical structure in the image. This is done by consideration of decorrelation.

If the ACF at some point $(\Delta x_i, \Delta y_j)$ has a value of half the peak, then that point will be considered in this analysis as no longer correlated. In images with complex structure, the ACF will not be azimuthally symmetric. To find a mean decorrelation distance in such cases a useful approach is to average the ACF in circular annuli. First, convert to polar coordinates:

$$r = \sqrt{\Delta x_i^2 + \Delta y_i^2} \tag{5.3}$$

$$\langle \mathrm{ACF}(r) \rangle = \frac{1}{N} \sum_{\theta=0}^{2\pi} \mathrm{ACF}(r\cos\theta, r\sin\theta) \tag{5.4}$$

Where N is the number of samples taken in θ space. Here r is sampled in 1 pixel steps. This reduces the order of ACF to one dimension and allows the computation of the 'decorrelation radius' (r_{DC}). Where:

$$\langle \mathrm{ACF}(r_{\mathrm{DC}}) \rangle = 0.5 \times \max\langle \mathrm{ACF} \rangle = 0.5 \times \langle \mathrm{ACF}(0) \rangle \tag{5.5}$$

In the case of the maps of the DRAO survey data the image coordinates are angular positions on the sky. The 'decorrelation radius' now becomes the 'decorrelation angle'. This quantity is indicative of the typical angular size of the structure present in a given map.

5.2 Intermediate Latitude Maps

To analyse the angular structure in the DRAO survey additional maps have been generated. All these maps have the same projection as the NGP and SGP maps and the same angular size. Each of these additional maps in centred on $b = 50°$, with the centre longitude being sampled in steps of 45°. The result is 8 maps that surround the NGP, with each map extending in latitude between $b = 70°$ and $b = 30°$. These maps have been produced for the polarised intensity and the Faraday depth data. Figures 5.1 and 5.2 show a mosaic of all these maps along with the NGP map in polarised brightness temperature and Faraday depth respectively. The dominant feature once again is the NPS, which can be seen in the lower half of Figure 5.1.

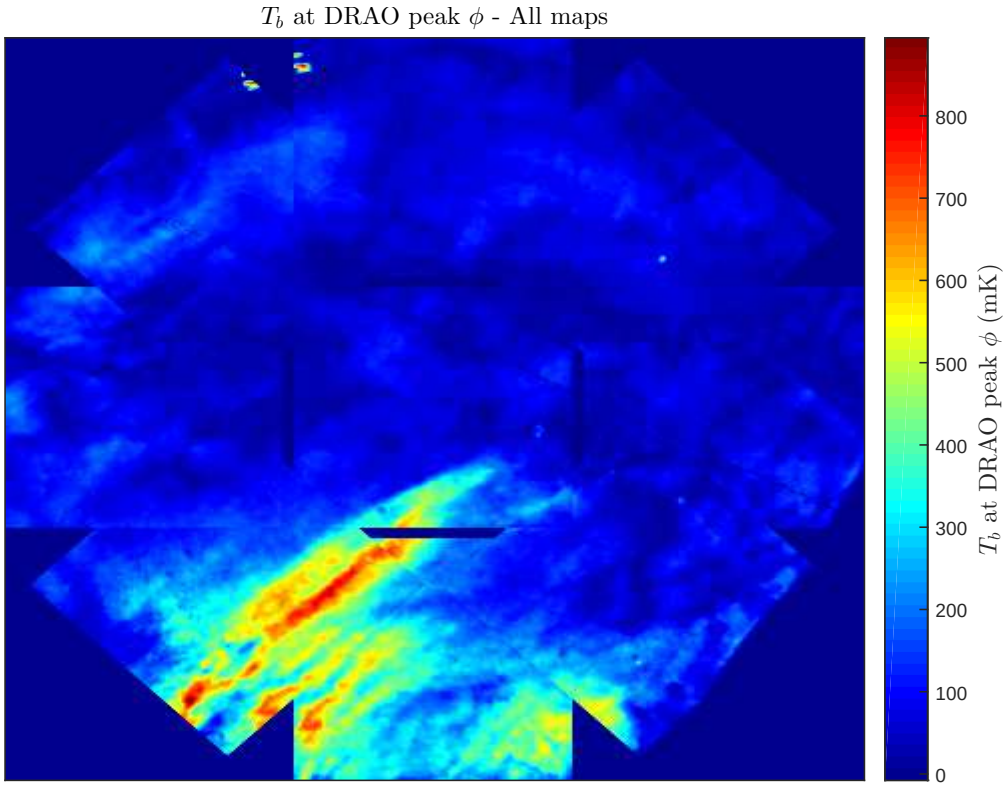

Figure 5.1: Mosaic map of polarised brightness temperature in intermediate latitudes and NGP.

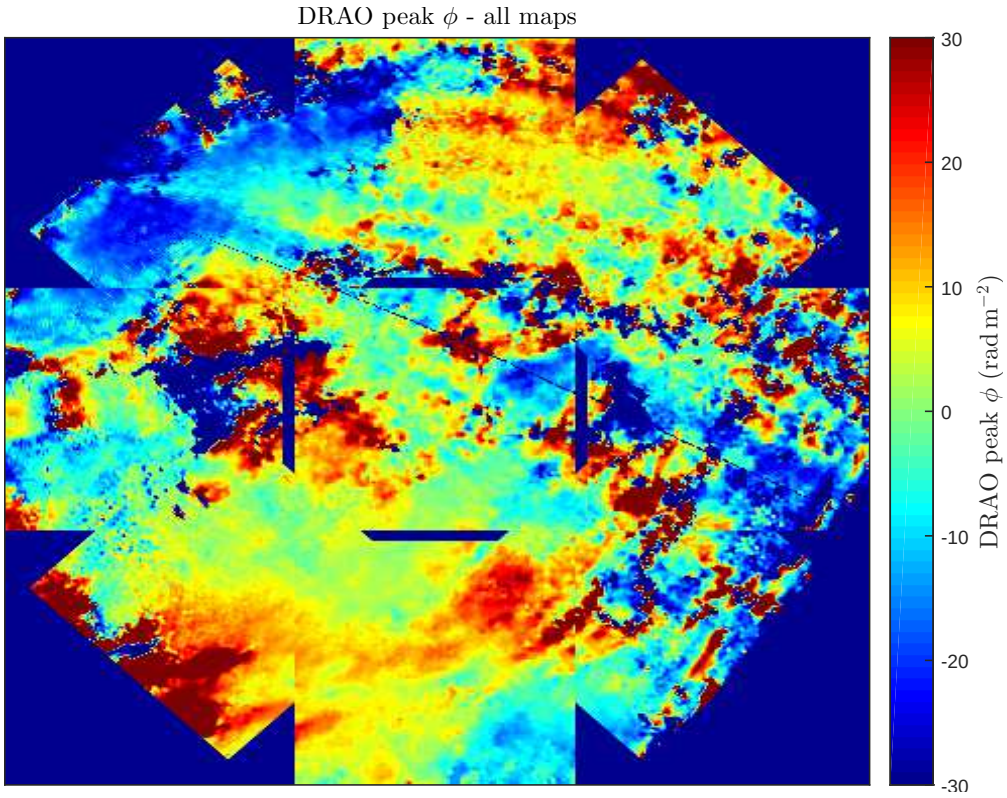

Figure 5.2: Mosaic map of Faraday depth in intermediate latitudes and NGP.

The individual maps of each region are provided in Appendix B.

5.3 Angular Structure in Poles and Intermediate Latitudes

The method outlined in Section 5.1 can now be applied to maps of the NGP, SGP and intermediate latitudes in both polarised intensity and Faraday depth. The purpose of this is to quantify the angular structure present in the DRAO survey. Evaluating the typical angular size of structure in each map has an impact on the error analysis that has been conducted. Previously, the number of independent samples was taken to be the number of beams in a given region. If the beam has averaged over some correlated structure, however, this assumption does not hold. Thus, the number of independent samples can be determined from finding the typical angular size of structure in each map.

The full autocorrelation process will be shown for the NGP only, but the same method was repeated for all the other regions. The additional figures for these

regions are given in Appendix B. First the ACF of the NGP Faraday depth map was found; this is given in Figure 5.3. Next, using Equations 5.3 and 5.4 averages in circular annuli were computed out to a radius of 150 pixels.

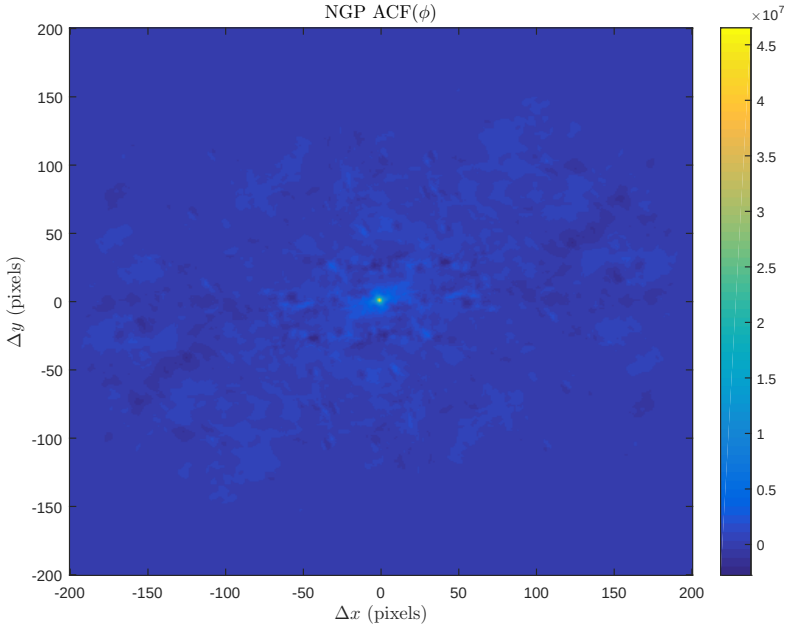

Figure 5.3: ACF of Faraday depth in NGP.

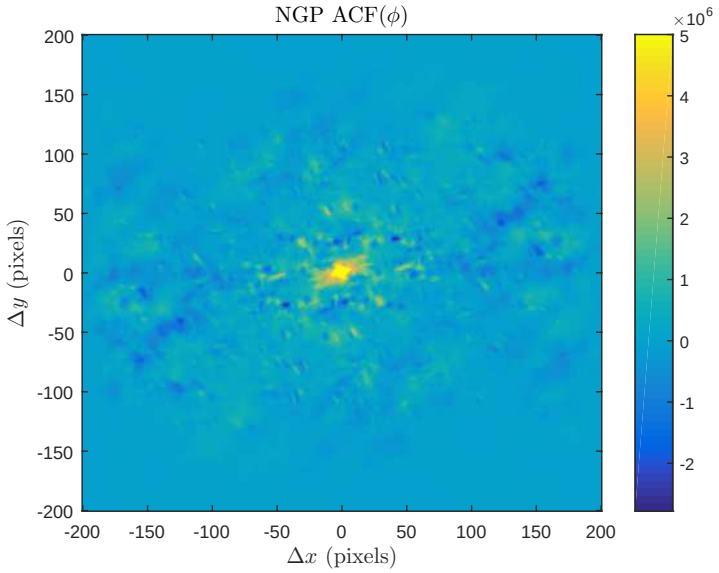

Figure 5.4: ACF of Faraday depth in NGP with range reduced.

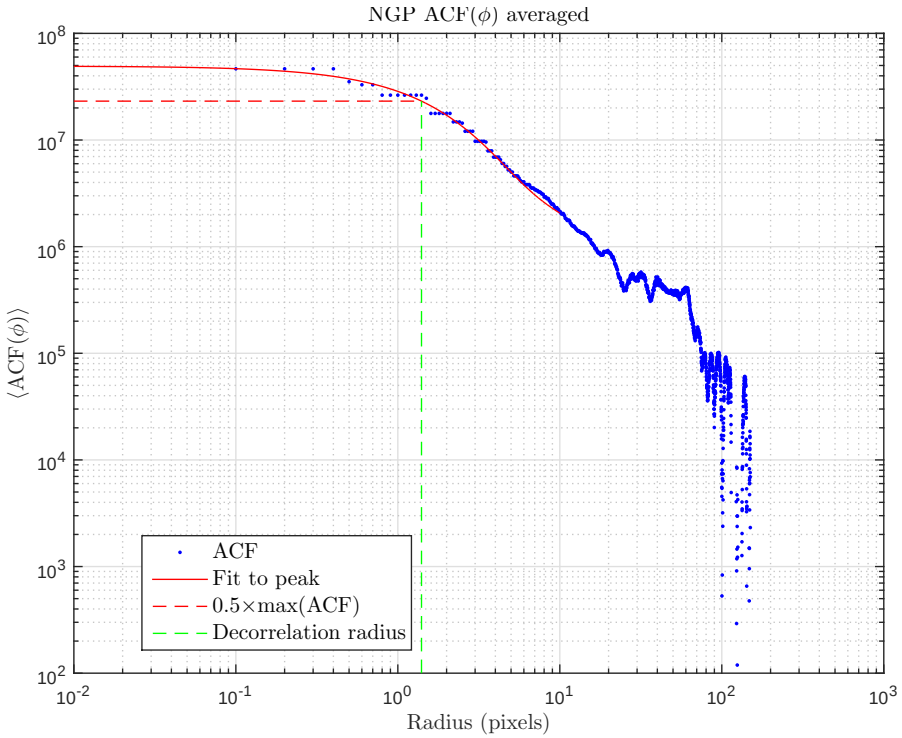

Figure 5.5: Averaged ACF of Faraday depth in the NGP. Note negative values have been exlcuded from 'log-log' plot.

In order to find the decorrelation angle, the radius which corresponded to a drop of 50% from the maximum needed to be found. In the NGP and most of the other maps, the peak of the ACF in Faraday depth drops very quickly, meaning that the ACF map is resolution limited. To overcome this a second order exponential fit was made to the peak of the form:

$$\mathrm{ACF} = a\exp(b \times r) + c\exp(d \times r) \tag{5.6}$$

For the NGP Faraday depth map the fit parameters were $a = (3.7 \pm 0.3) \times 10^6$, $b = -(0.065 \pm 0.005)$, $c = (4.6 \pm 0.0.4) \times 10^6$ and $d = -(0.60 \pm 0.01)$. The averaged ACF along with the fit and the location of the decorrelation radius are given in Figure 5.5. The decorrelation angle is found by using the angular size of a pixel in the map of 0.2° pixel^{-1}. This was repeated for the maps of the SGP and intermediate latitudes for both Faraday depth and polarised intensity.

The results of this analysis in all regions are summarised in Tables 5.1 and 5.2. Comparing the values found, it is immediately obvious that structure is usually larger in the polarised intensity maps. In fact, the difference in angular size is greater than expected, as there is a correlation between the location of polarised emission and the location of Faraday depth. The source of this discrepancy is likely spurious Faraday depth detections due to low polarised emissions. Additionally,

the effect of the NPS has not been accounted for. The solution to this is to take smaller sub-regions within each map, selecting regions only with higher polarised emission. This would entail a similar method of thresholding that was used in Sections 3.1.2 and 3.1.3. Each subregion can then also be marked if it contains a part of the NPS, which will allow for the effect of the NPS on angular structure to be quantified.

Region	DCR (pixels) - ϕ	DCA (deg) - ϕ
NGP	1.4	0.28
SGP	2.8	0.56
SGP (masked)	3.45	0.69
$l = 0°$	26.3	5.26
$l = 45°$	6.1	1.22
$l = 90°$	2.67	0.53
$l = 135°$	2.53	0.506
$l = 180°$	2.54	0.508
$l = 225°$	2.41	0.482
$l = 270°$	2.37	0.474
$l = 315°$	2.66	0.532

Table 5.1: Decorrelation radius (DCR) and decorrelation angle (DCA) for all regions in Faraday depth.

Region	DCR (pixels) - T_b	DCA (deg) - T_b
NGP	38.0	7.60
SGP	55.8	11.16
SGP (masked)	45.7	9.14
$l = 0°$	66.8	13.36
$l = 45°$	67.4	13.5
$l = 90°$	51.4	10.3
$l = 135°$	62.6	12.5
$l = 180°$	58.2	11.6
$l = 225°$	74.1	14.8
$l = 270°$	57.6	11.5
$l = 315°$	43.0	8.60

Table 5.2: Decorrelation radius (DCR) and decorrelation angle (DCA) for all regions in polarised intensity.

Within the time constraints of this project, however, this subregion analysis has

not been completed. Although, the correlation data that has been found per map can be used to update the error analysis of Faraday depth.

5.4 Updated Error Analysis

In the error analysis conducted previously (see Section 3.1.1) the number of independent samples (n) was taken to be the number of beam areas included in a given average. This is not necessarily a correct assumption, as a beam area may average over a correlated region. As such, with the correlation data that has been computed the number of independent samples can be more reliably determined. Here correlated structure will be assumed to take the form of a circular Gaussian on the sky. This way Equation 3.2 can be used to estimate the average angular size of correlated structure for a given map. Now, the half-power beam width will be taken to be twice the decorrelation angle:

$$HPBW = 2 \times \text{DCA} \tag{5.7}$$

Using Equation 3.4 the number of pixels per 'correlation beam' can be found. From this value the errors in the average Faraday depth for the North and South Galactic Poles have been updated. In the NGP the number of pixels per 'correlation beam' was found to be $m \approx 8.9$ pixels. Similarly, in the SGP $m \approx 54$ pixels. The results of this updated analysis are given in Tables 5.3 and 5.4.

Method	ϕ_{av} with NPS ($\text{rad}\,\text{m}^{-2}$)	ϕ_{av} without NPS ($\text{rad}\,\text{m}^{-2}$)
No threshold	2 ± 2	3 ± 2
$\Delta\phi < 10\,\text{rad}\,\text{m}^{-2}$	1.4 ± 0.5	1.4 ± 0.6
$\Delta\phi < 5\,\text{rad}\,\text{m}^{-2}$	-0.2 ± 0.6	-0.9 ± 0.8
Weighted average	1.2 ± 0.3	0.1 ± 0.5

Table 5.3: Mean Faraday depth as found in the North Galactic Pole with updated errors.

Method	ϕ_{av} with mask ($\text{rad}\,\text{m}^{-2}$)	ϕ_{av} without mask ($\text{rad}\,\text{m}^{-2}$)
No threshold	-1 ± 4	-4 ± 4
$\Delta\phi < 10\,\text{rad}\,\text{m}^{-2}$	-2 ± 1	-4 ± 2
$\Delta\phi < 5\,\text{rad}\,\text{m}^{-2}$	-2.6 ± 0.8	-5 ± 1
Weighted average	-3 ± 1	-5 ± 1

Table 5.4: Mean Faraday depth as found in the South Galactic Pole with updated errors.

Clearly this analysis has had a far greater impact on the error of the averages in the SGP, with a much greater change in the number of independent samples. Interestingly, this is likely due to the SGP being far less noise dominated. This meant the SGP was more correlated in angular structure. In the NGP far more spurious detections in Faraday depth were found, which caused the data to be less correlated in angular structure. This in turn caused the peak of the ACFs in the NGP and surrounding regions to be far steeper, which is why they became resolution limited near the peak when averaged. This being the case, it will be still be necessary to conduct the subregion structure analysis, as discussed previously. This will ensure that the structure being quantified is not spurious in origin. Additionally, it can be seen in the ACF maps (such as Figure B.33) that the peaks are not always circularly symmetric. As such, the annular averages should be taken in ellipses not circles. This would also mean the correlation beam would become an elliptical Gaussian, rather than circular. If work is continued on this project in the future, this will be very important to bear in mind.

Chapter 6

Conclusion and Discussion

6.1 Conclusion

Presented here is an analysis of the DRAO 26 m rotation measure synthesis survey, restricted to the North and South Galactic Poles. The purpose of this analysis was to ascertain Faraday depth information in the Galactic poles which in turn allows the study of the magneto-ionic medium of the Galaxy at the position of the sun. Analysis was restricted to the Galactic poles to avoid the depolarisation effects that are present near the Galactic plane and to enable the study of the vertical Galactic magnetic field at the position of the sun.

The Faraday depth for each line of sight was determined from the location of the peak in the Faraday spectrum produced by rotation measure synthesis. Maps of both Faraday depth and polarised brightness temperature were produced in a $1600\,\mathrm{deg}^2$ square area centred on each pole. New analysis of error in the Faraday depth was obtained from Sun et al. (2015), who showed that the error found in observed Faraday depth is much higher than simple analysis indicates. The relationship between polarised brightness temperature and error in Faraday depth determined by Sun et al. (2015) was used to average the Faraday depth of the North and South Galactic poles.

In the North Galactic Pole thresholding by an uncertainty $\Delta\phi < 5\,\mathrm{rad\,m^{-2}}$ gave a mean Faraday depth of $-0.2\pm0.7\,\mathrm{rad\,m^{-2}}$ and $-1\pm1\,\mathrm{rad\,m^{-2}}$, with and without the North Polar spur respectively. Using a method of a weighted average produced a more reliable result, however, by weighting by the error squared. The average Faraday depth determined by this method was $1.2\pm0.3\,\mathrm{rad\,m^{-2}}$ and $0.1\pm0.6\,\mathrm{rad\,m^{-2}}$, with and without the North Polar Spur respectively. This result was compared to the extra-Galactic survey presented in Mao et al. (2010), who obtained an average rotation measure of $0.0\pm0.5\,\mathrm{rad\,m^{-2}}$. There is an agreement between these two surveys that the average Faraday depth in the North Galactic Pole is near $0\,\mathrm{rad\,m^{-2}}$. This in turn implies no detection of a mean vertical magnetic field in the North Galactic Pole. A trend was found across the North Galactic Pole region, however. This trend implies a field reversal near the pole itself, with the magnitude of the magnetic field being in the order of $\sim 1\,\mu$G. Whether the field reversal occurs in the vertical or horizontal field has not been determined. It is possible to conclude, however, that strict dipole or quadrupole models have been ruled out. Both models predict a vertical magnetic field in the North Polar region, which has not been detected in this survey, nor in extra-Galactic surveys.

The same analysis was carried out in the South Galactic Pole, despite the DRAO survey not covering below a declination of $\delta = -30°$. Strong scanning effects were identified in this region and were subsequently masked out from analysis. Thresholding by an uncertainty $\Delta\phi < 5\,\mathrm{rad\,m^{-2}}$ gave a mean Faraday depth of $-2.3\pm0.4\,\mathrm{rad\,m^{-2}}$. Again the method of weighted averaging provided a more reliable result $-3.1\pm0.2\,\mathrm{rad\,m^{-2}}$. Comparing to the average value obtained by Mao et al. (2010) of $-6.3\pm0.7\,\mathrm{rad\,m^{-2}}$, as well as point-for-point, reveals strong disagreement in the value of Faraday depth for this region. This implies necessarily

that the diffuse polarised emission observed in the South Galactic Pole is local. For the region that was included in the survey this corresponds to a magnetic field magnitude in the order of $\sim 1\,\mu$G. A trend in the magnetic field could not be determined, as approximately 55% of the region was either not observed or excluded due to scanning effects.

The angular structure of both polarised brightness temperature and Faraday depth was quantified in the South Galactic Pole, North Galactic Pole and surrounding Northern Galactic intermediate latitudes. This was completed using the two-dimensional autocorrelation function, which enabled the calculation of the decorrelation angle to be determined for each region. The decorrelation angle was taken to be the angular distance at which the autocorrelation function reduced to half of its maximum. Assuming that correlated structure could be approximated by a circular Gaussian the number of independent samples in each map was updated from previous analysis. Using updated analysis the average Faraday depth in the North and South Galactic Poles was found to be $0.1 \pm 0.5\,\mathrm{rad\,m^{-2}}$ and $-3.1 \pm 1\,\mathrm{rad\,m^{-2}}$ respectively.

6.2 Discussion

The recent finding of Sun et al. (2015), that errors in Faraday depth are far larger than expected from Gaussian fitting, became a vital result for this analysis. Through this result it was shown that the large magnitude detections in Faraday depth found in the polar regions were, in fact, spurious. The reason for this was because they were associated with low levels of polarised emission. This has a strong impact on the analysis of Faraday depth the North Galactic Pole, where much of the emission away from the North Polar Spur was of very low magnitude. Ultimately, this resulted in data needing to be discarded from analysis, which in turn made analysis of the magnetic field more difficult. The simplifying assumption that the Faraday depth in the poles was averaged evenly in longitude could not be used in the computation of the vertical magnetic field. As such, only mean magnetic field magnitudes could be evaluated, without discerning whether the contribution came from the horizontal or vertical field. In future work, however, it may be possible to use the trend found in the North Galactic Pole to determine these field components. Additionally, as the distance was not known to the emission regions, a single value for the magnetic field magnitude could not be determined. If such distances could be found then a value for the magnetic field magnitude could be given with much more certainty.

Such work in the South Galactic Pole, however, simply requires more data. The next GMIMS survey is being conducted by the Parkes 64 m Telescope, and is expected to be completed in 2016. As this survey is being conducted in the Southern Hemisphere it will feature full coverage of the South Galactic Pole. This survey and subsequent new surveys will provide an excellent means of extending the re-

sults found in this analysis. Particularly, full sky coverage will enable complete magnetic field information to be found. This will then allow comparison with theoretical Galactic magnetic field models.

Finally the error analysis of each region does require additional work. The work conducted using the two-dimensional autocorrelation function can be continued; taking greater care to consider both the distribution of the autocorrelation function and the presence of spurious Faraday depth detections. Subregions could be taken of each map presented here where only sufficiently high polarised brightness temperature is present. This should avoid the inclusion of spurious Faraday depth regions in the angular structure analysis. The distribution of the autocorrelation function was often non-circular. Thus, to average autocorrelation function elliptical annuli should be taken which will in turn produce elliptical 'correlation beams' for each map.

Appendix A

Additional Formulas and Concepts

A.1 Inverse of a Fourier Transform

For some Fourier transform in general form with arbitrary f, F, x and t:

$$f(x) = \int_{-\infty}^{+\infty} F(t)e^{-2\pi ixt}dt \tag{A.1}$$

The inverse of the transform is:

$$F(t) = \int_{-\infty}^{+\infty} f(x)e^{2\pi ixt}dx \tag{A.2}$$

A.2 Convolution Theorem

Given two functions $f(t)$ and $g(t)$, the convolution of these two functions is defined as:

$$f * g \equiv \int_{-\infty}^{+\infty} f(\tau)g(t-\tau)d\tau = \int_{-\infty}^{+\infty} f(t-\tau)g(\tau)d\tau \tag{A.3}$$

Qualitatively, convolution gives the area of overlap between the two functions as one function is translated across the other. There is a useful theorem relating convolution and the Fourier transform called the Convolution Theorem. The theorem states Fourier transform of two convolved functions is equal to the product of the Fourier transform of each function:

$$\mathcal{F}(f * g) = \mathcal{F}(f)\mathcal{F}(g) \tag{A.4}$$

Where $\mathcal{F}$ denotes the Fourier transform. Taking the inverse Fourier transform gives the form:

$$\mathcal{F}^{-1}(\mathcal{F}(f)\mathcal{F}(g)) = f * g \tag{A.5}$$

A.3 Stereographic Projection

The stereographic projection maps a point (P) from a sphere onto a point (P') on a plane tangent to the sphere's south pole. The point is projected from the sphere's north pole, through P and then onto the plane as shown in Figure A.1. This is the method of stereographic projection used by the FITS World Coordinate System (WCS) (Calabretta and Greisen, 2002).

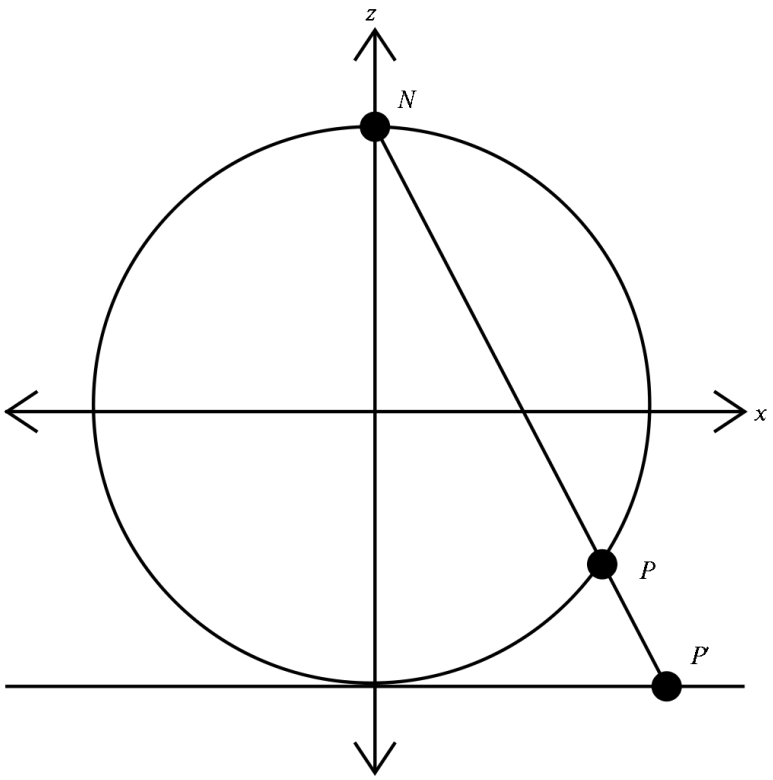

Figure A.1: Visual representation of stereographic projections (Commons, 2007).

Appendix B

Additional Figures

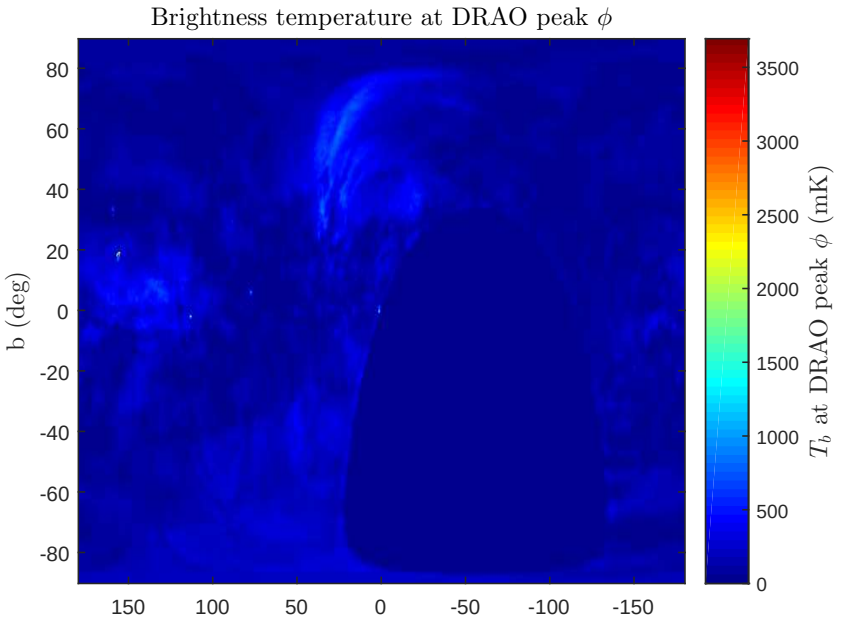

Figure B.1: Polarised brightness temperature at peak in Faraday spectrum.

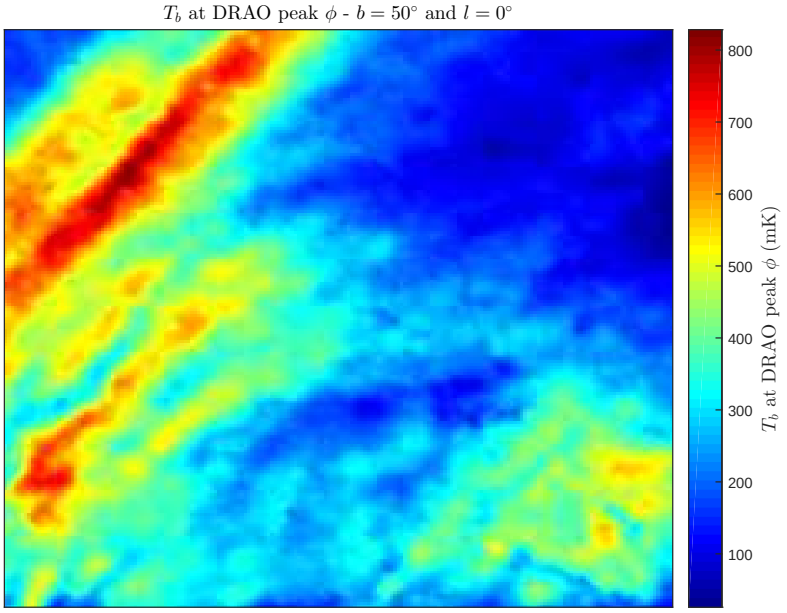

Figure B.2: Map of polarised brightness temperature centred in $l = 0°$, $b = 50°$.

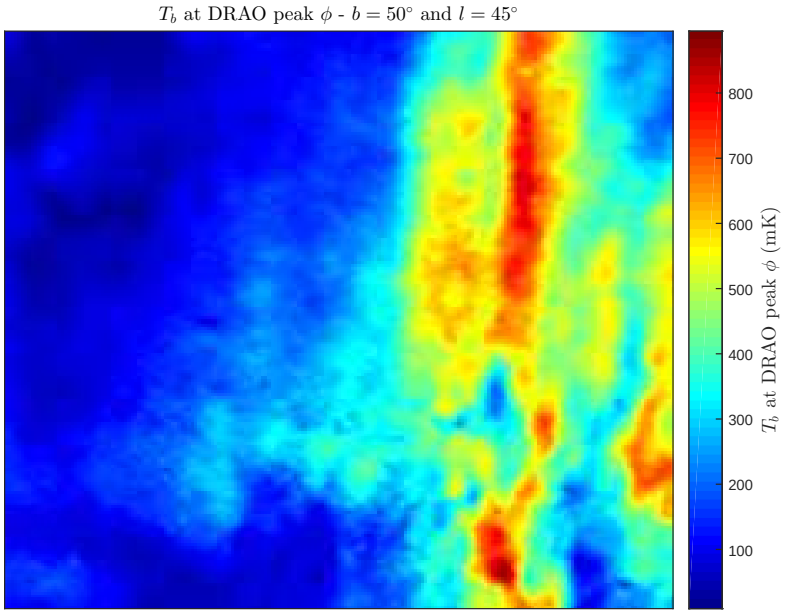

Figure B.3: Map of polarised brightness temperature centred in $l = 45°$, $b = 50°$.

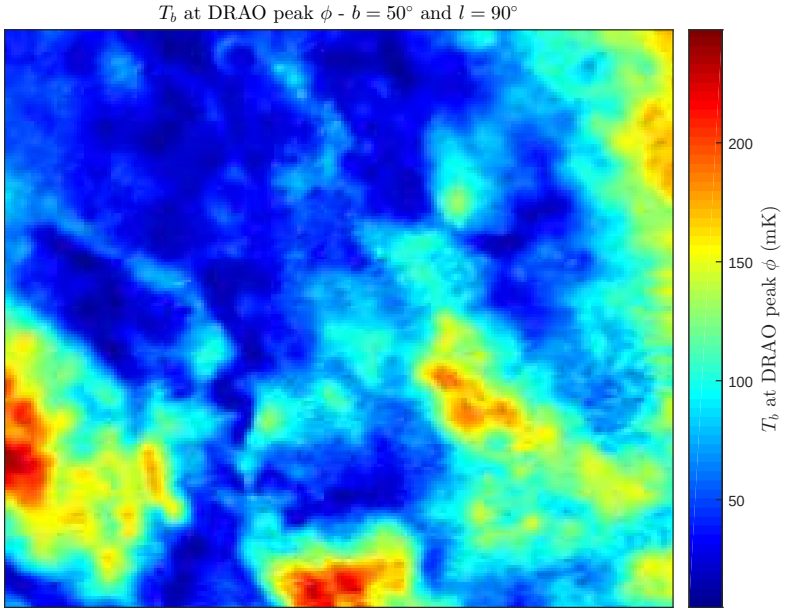

Figure B.4: Map of polarised brightness temperature centred in $l = 90°$, $b = 50°$.

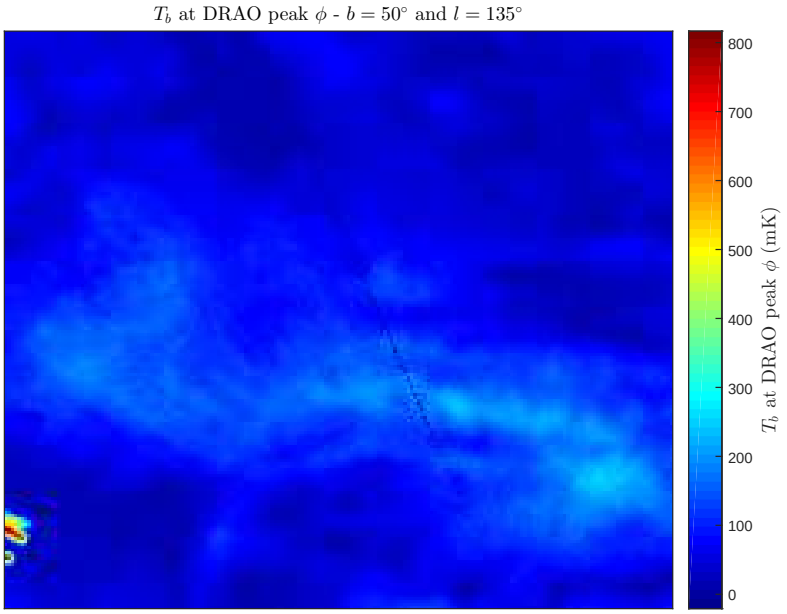

Figure B.5: Map of polarised brightness temperature centred in $l = 135°$, $b = 50°$.

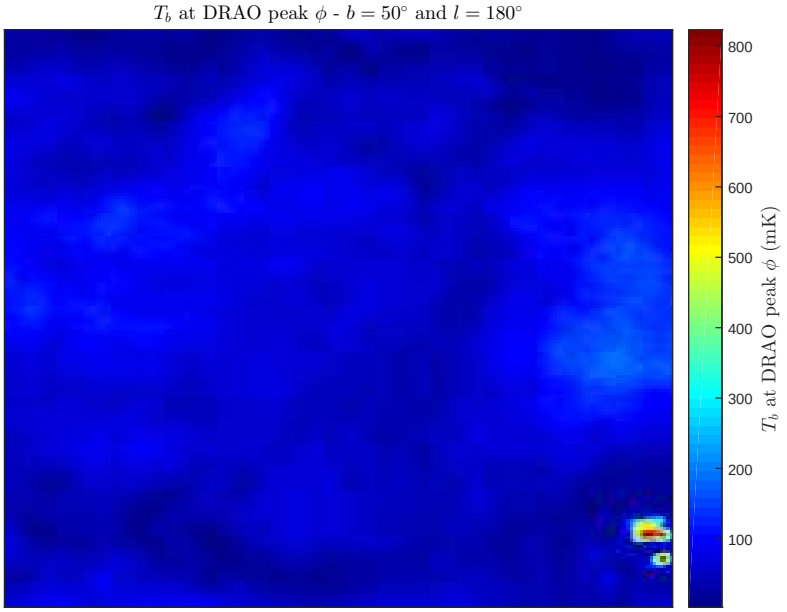

Figure B.6: Map of polarised brightness temperature centred in $l = 180°$, $b = 50°$.

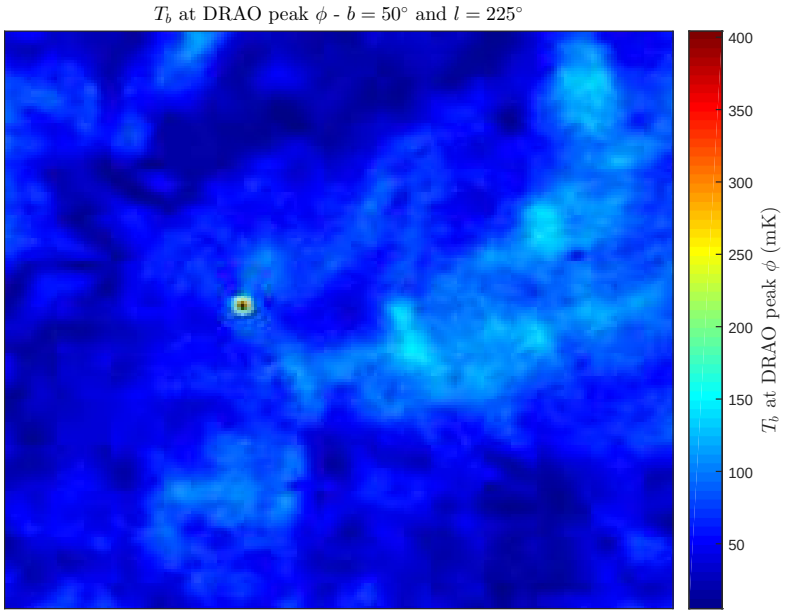

Figure B.7: Map of polarised brightness temperature centred in $l = 225°$, $b = 50°$.

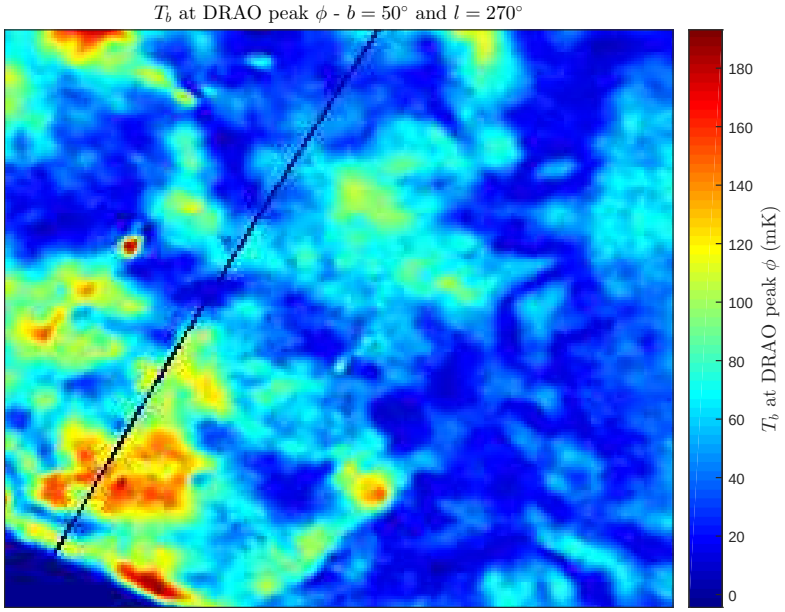

Figure B.8: Map of polarised brightness temperature centred in $l = 270°$, $b = 50°$.

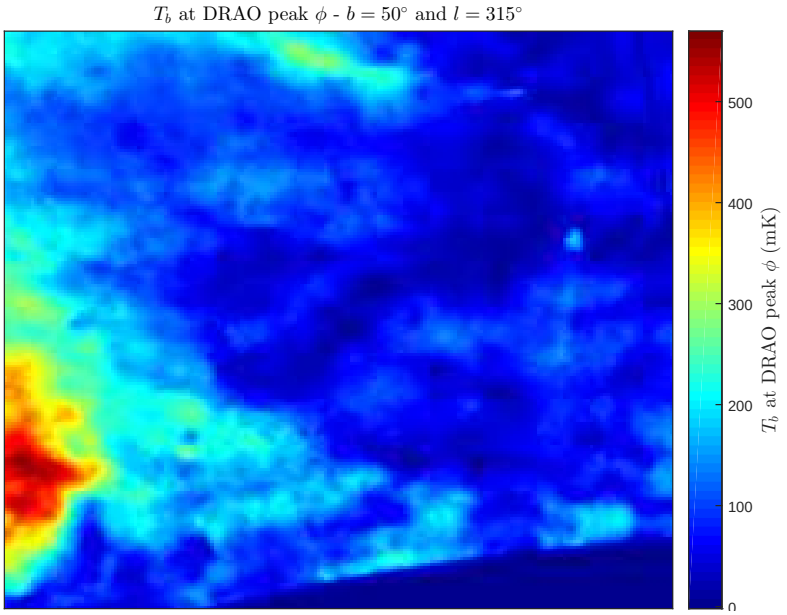

Figure B.9: Map of polarised brightness temperature centred in $l = 315°$, $b = 50°$.

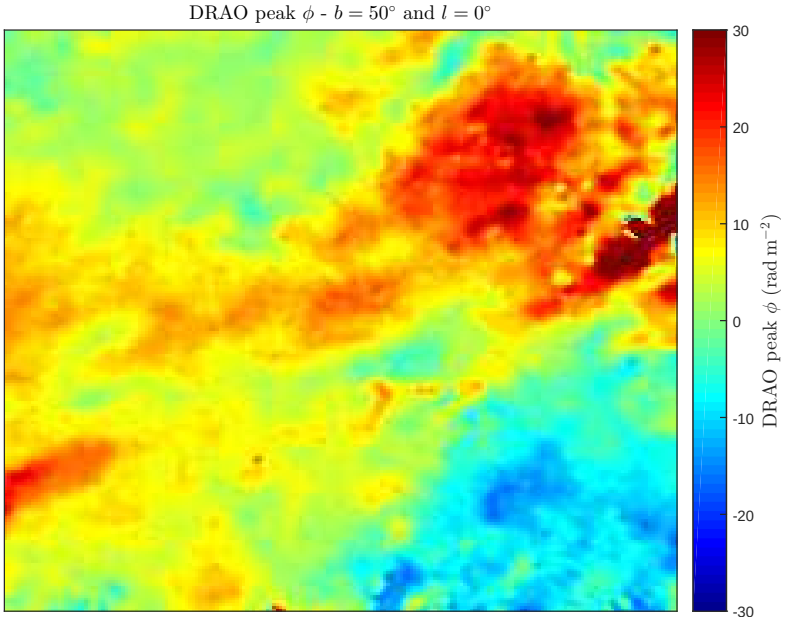

Figure B.10: Map of Faraday depth centred in $l = 0°$, $b = 50°$.

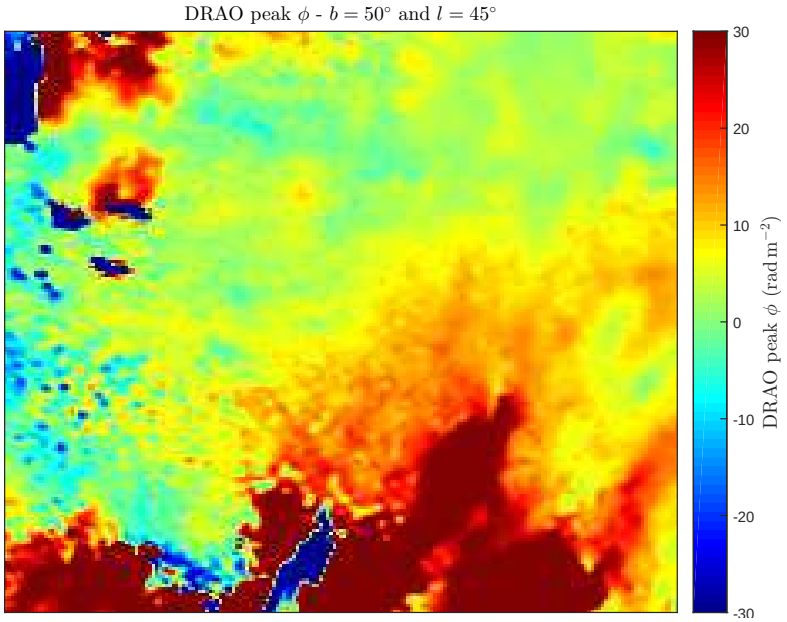

Figure B.11: Map of Faraday depth centred in $l = 45°$, $b = 50°$.

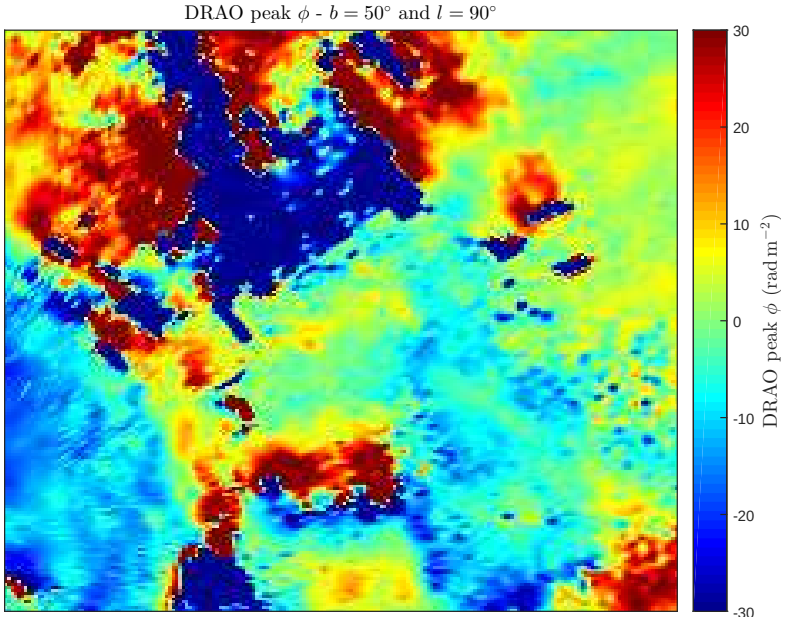

Figure B.12: Map of Faraday depth centred in $l = 90°$, $b = 50°$.

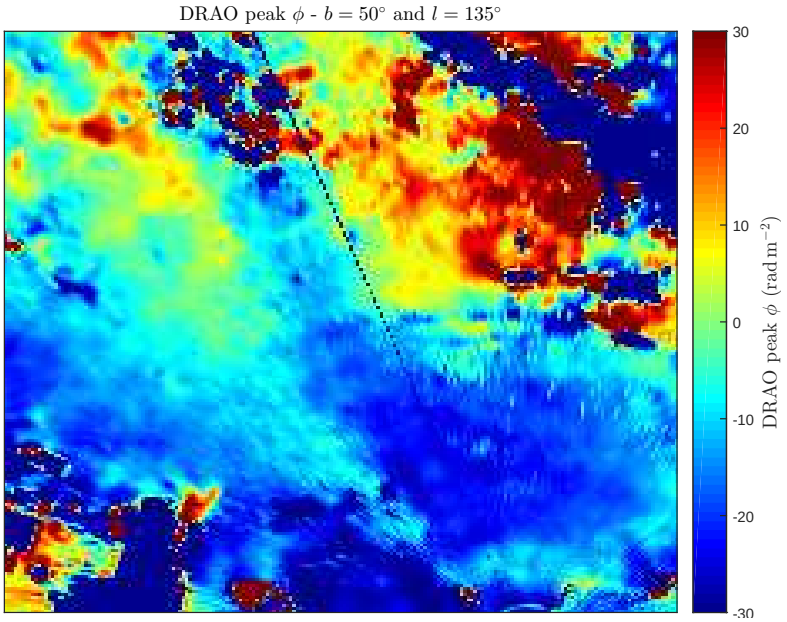

Figure B.13: Map of Faraday depth centred in $l = 135°$, $b = 50°$.

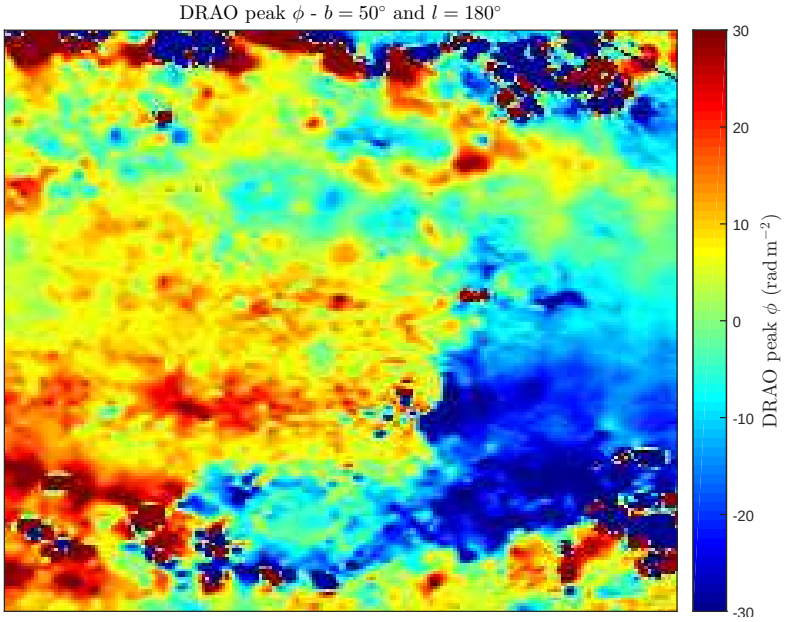

Figure B.14: Map of Faraday depth centred in $l = 180°$, $b = 50°$.

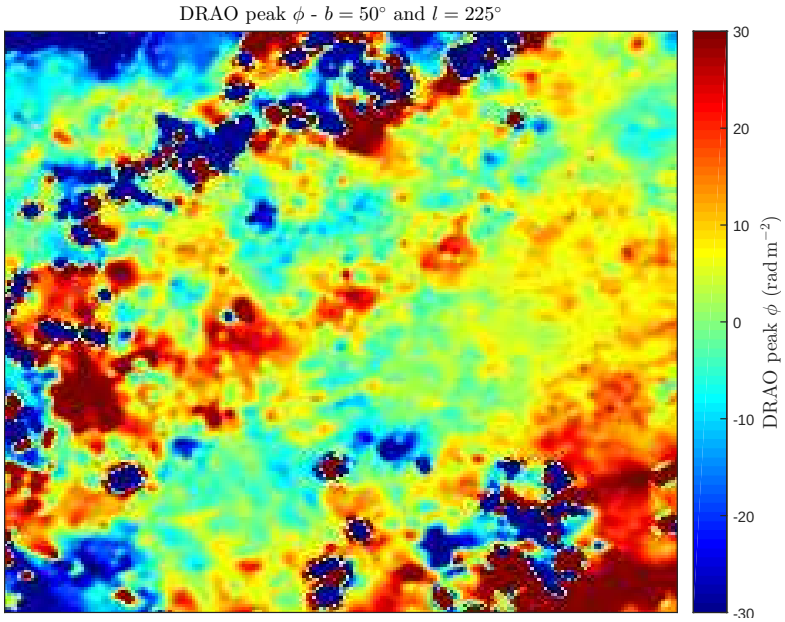

Figure B.15: Map of Faraday depth centred in $l = 225°$, $b = 50°$.

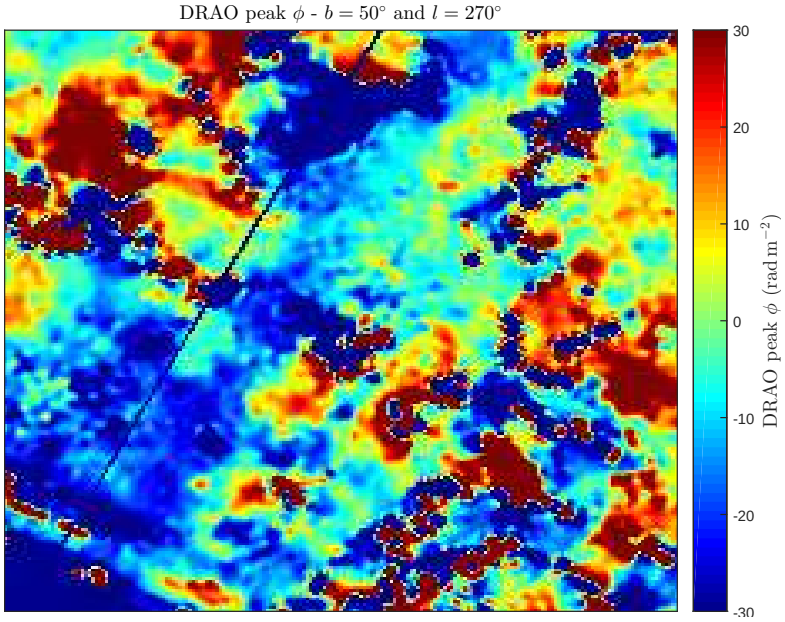

Figure B.16: Map of Faraday depth centred in $l = 270°$, $b = 50°$.

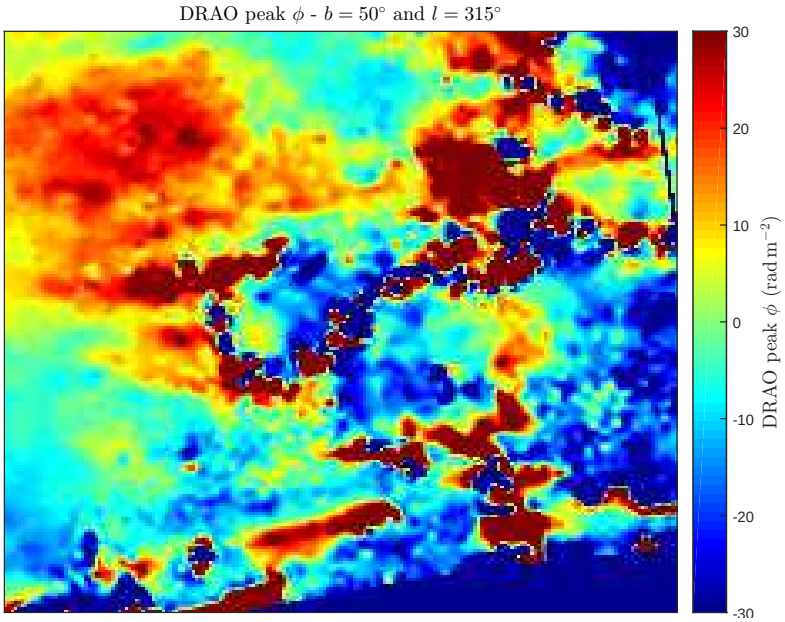

Figure B.17: Map of Faraday depth centred in $l = 315°$, $b = 50°$.

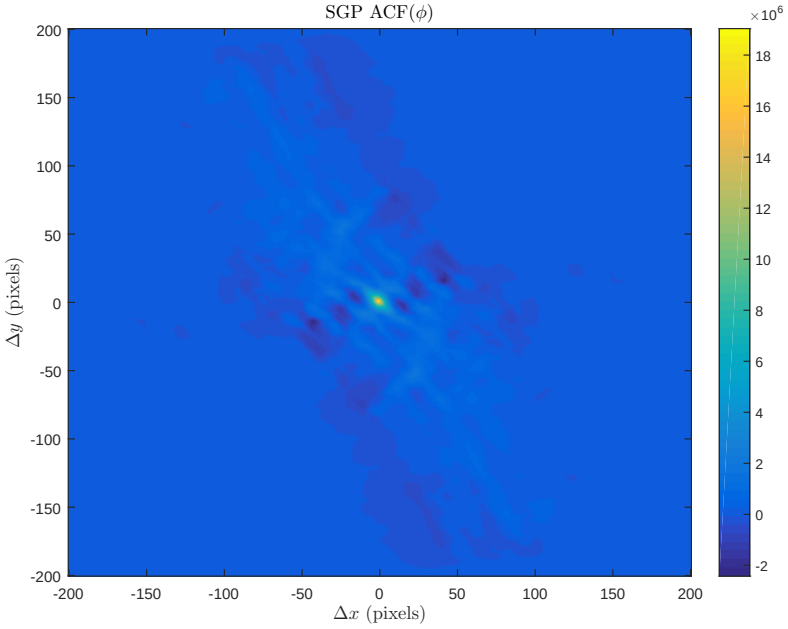

Figure B.18: ACF of Faraday depth in the SGP.

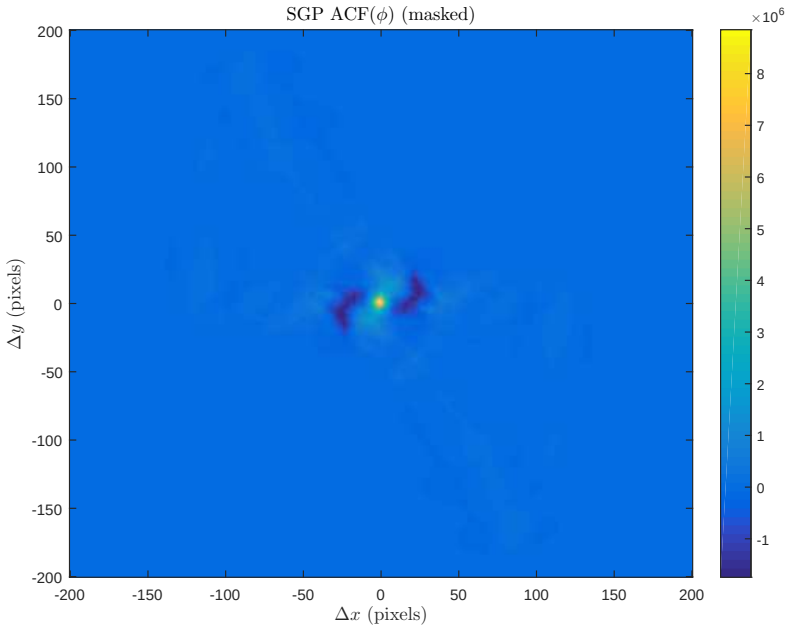

Figure B.19: ACF of Faraday depth in the SGP (masked).

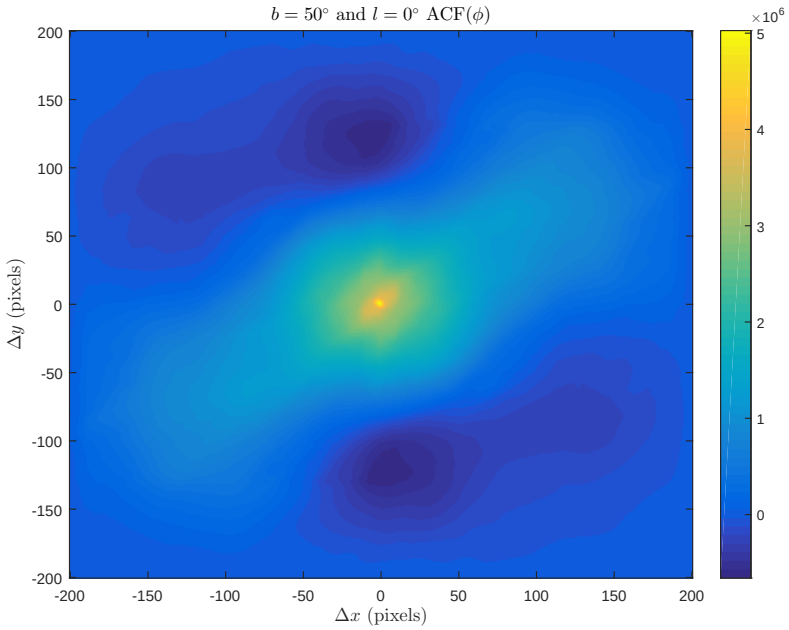

Figure B.20: ACF of Faraday depth at $b = 50°$, $l = 0°$.

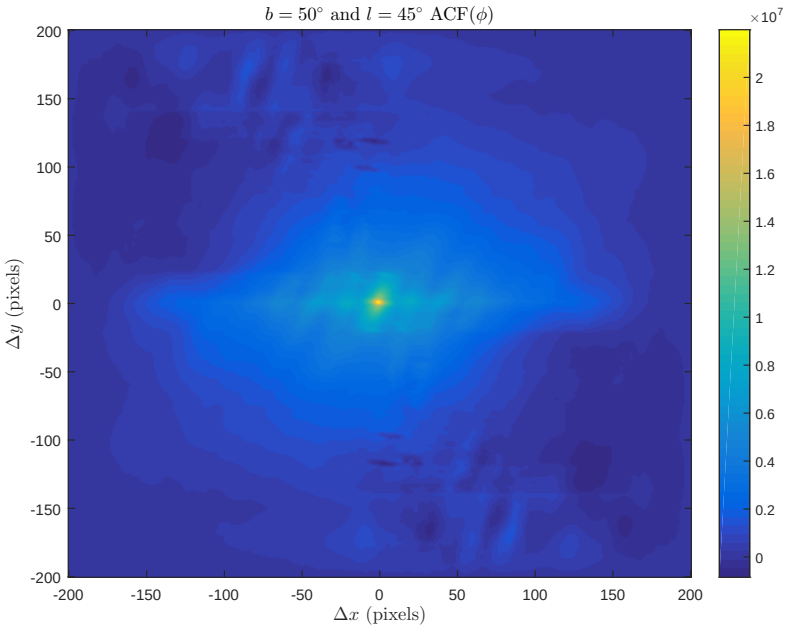

Figure B.21: ACF of Faraday depth at $b = 50°$, $l = 45°$.

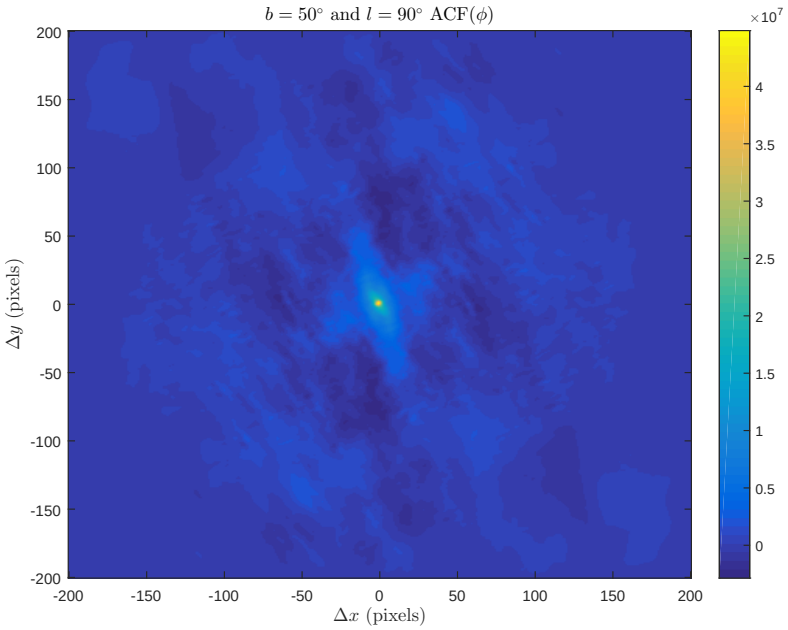

Figure B.22: ACF of Faraday depth at $b = 50°$, $l = 90°$.

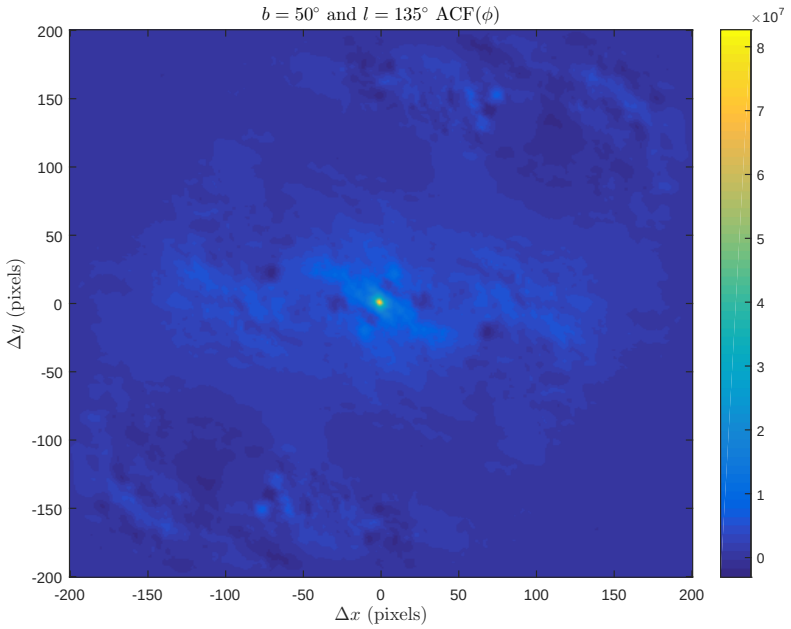

Figure B.23: ACF of Faraday depth at $b = 50°$, $l = 135°$.

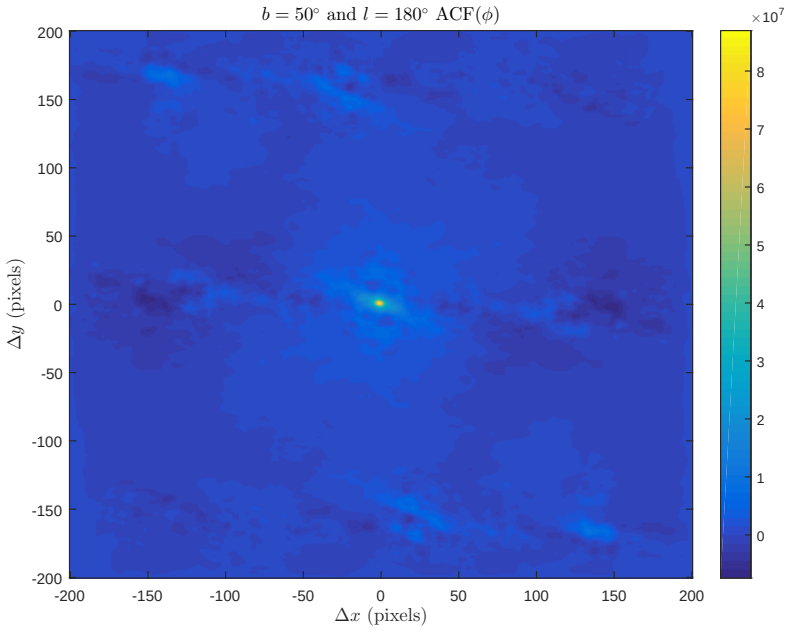

Figure B.24: ACF of Faraday depth at $b = 50°$, $l = 180°$.

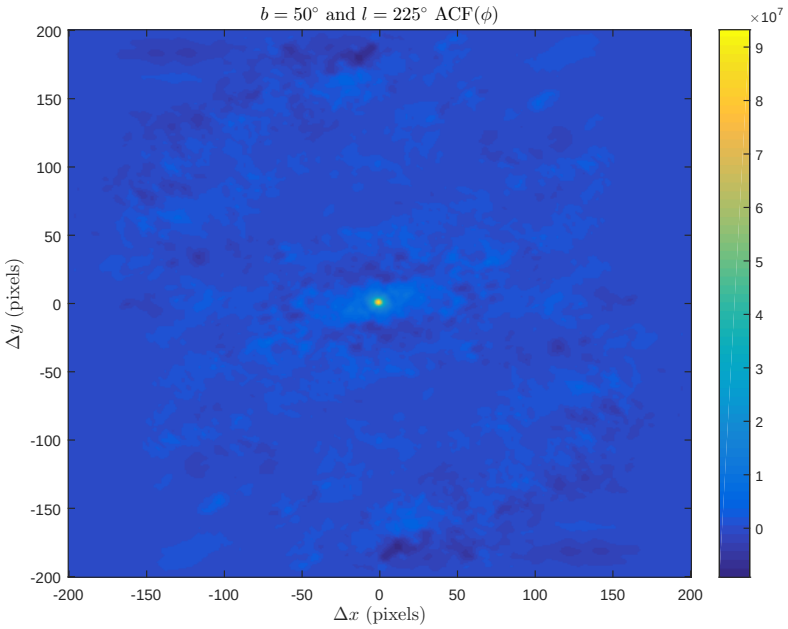

Figure B.25: ACF of Faraday depth at $b = 50°$, $l = 225°$.

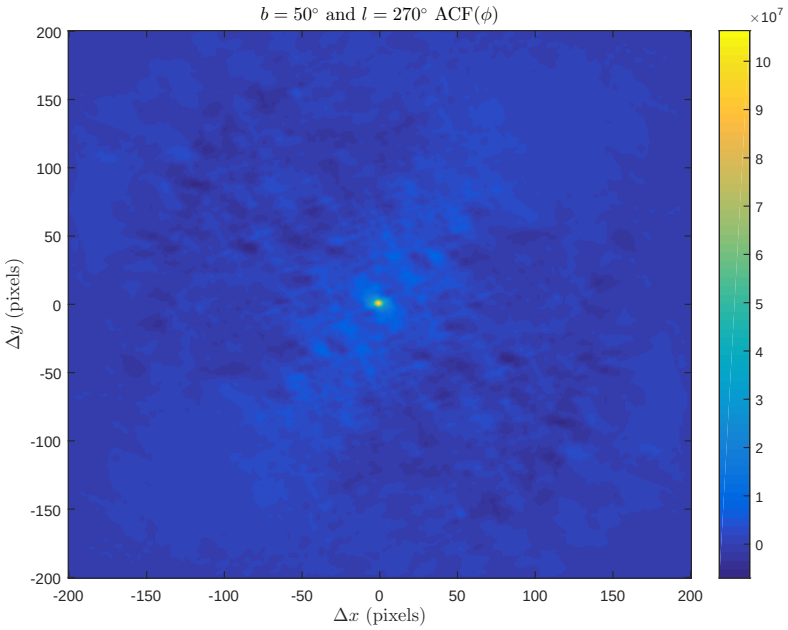

Figure B.26: ACF of Faraday depth at $b = 50°$, $l = 270°$.

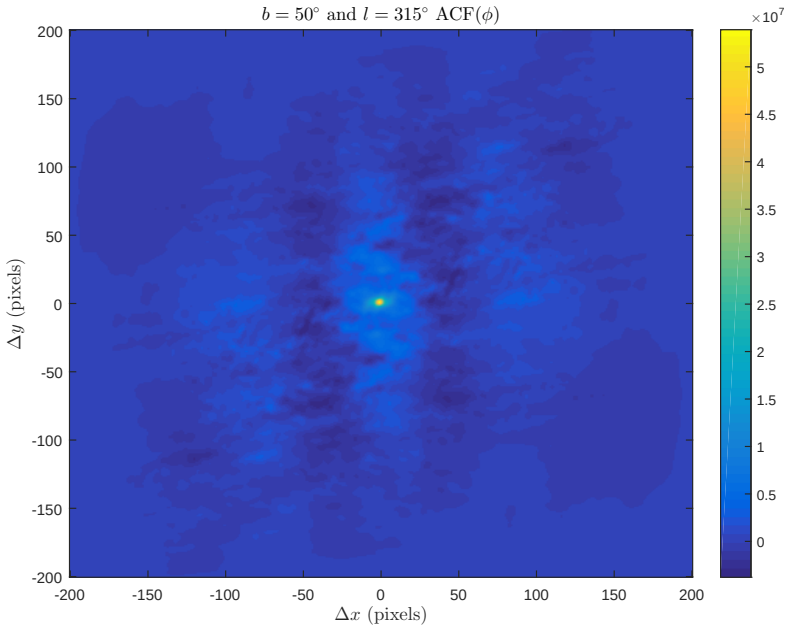

Figure B.27: ACF of Faraday depth at $b = 50°$, $l = 315°$.

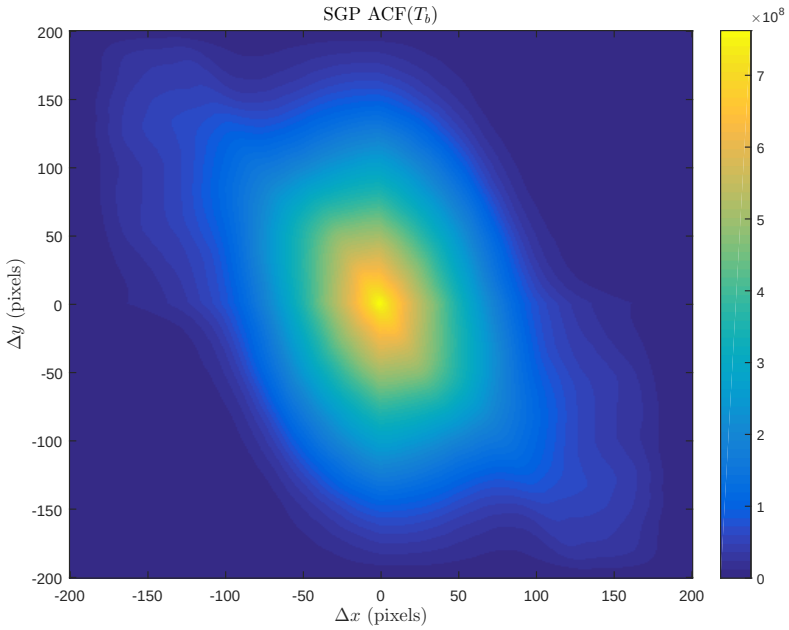

Figure B.28: ACF of T_b in the SGP.

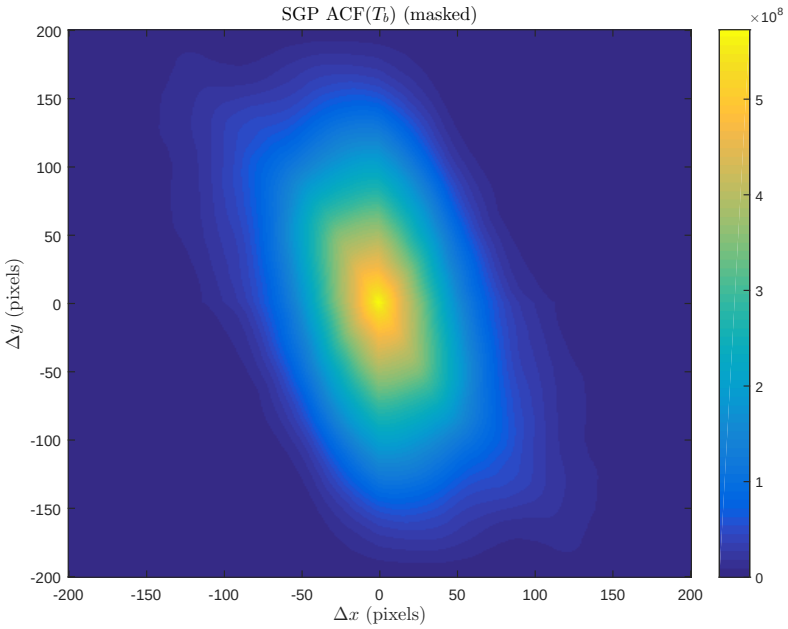

Figure B.29: ACF of T_b in the SGP (masked).

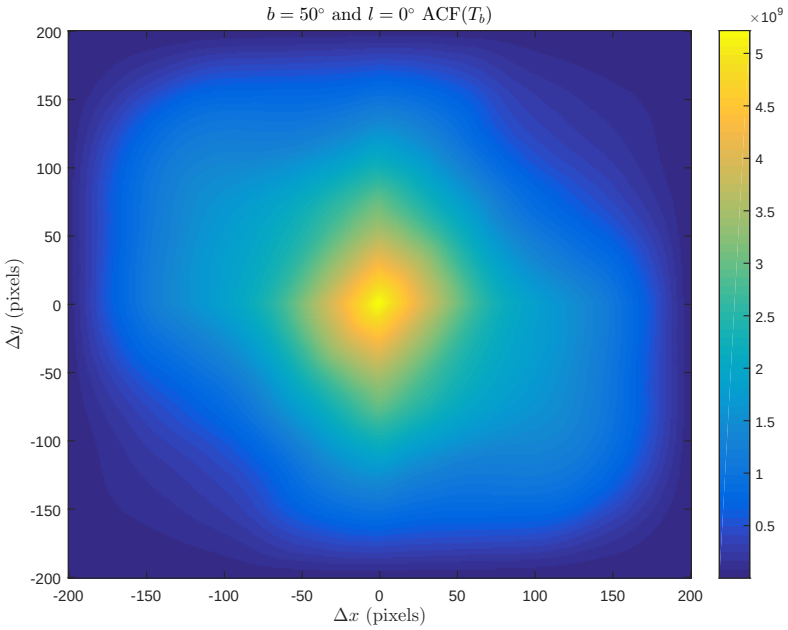

Figure B.30: ACF of T_b at $b = 50°$, $l = 0°$.

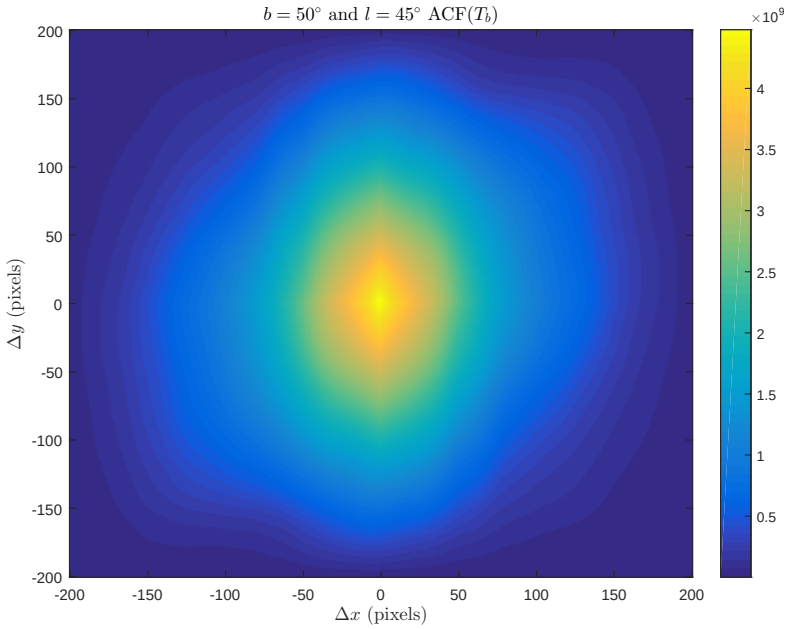

Figure B.31: ACF of T_b at $b = 50^\circ$, $l = 45^\circ$.

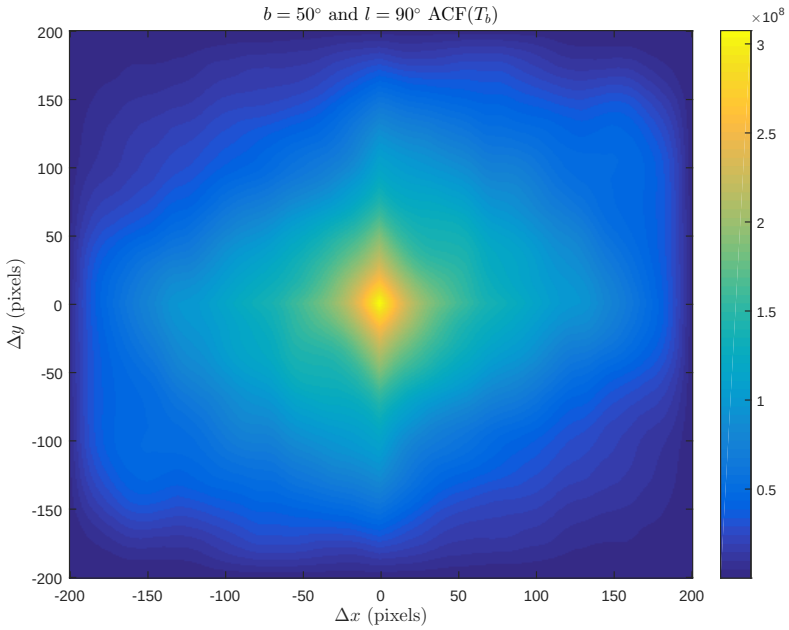

Figure B.32: ACF of T_b at $b = 50^\circ$, $l = 90^\circ$.

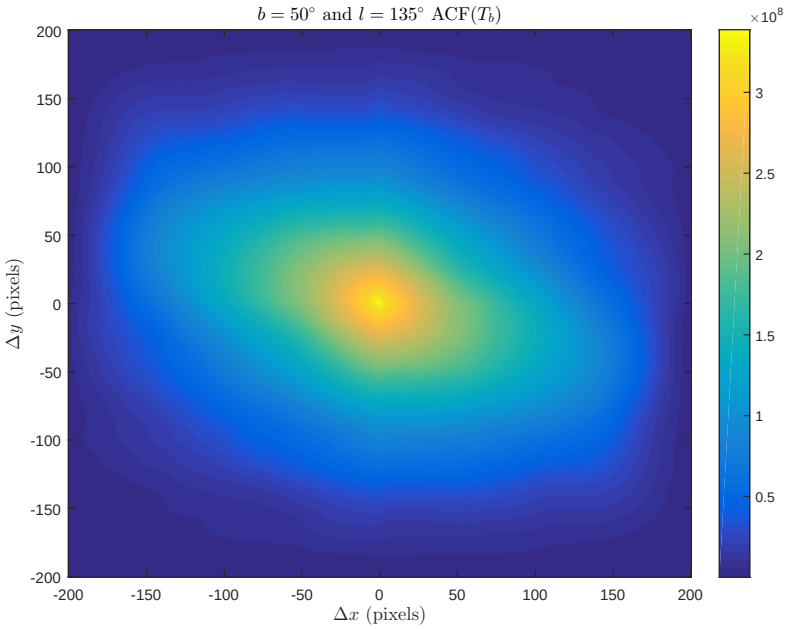

Figure B.33: ACF of T_b at $b = 50°$, $l = 135°$.

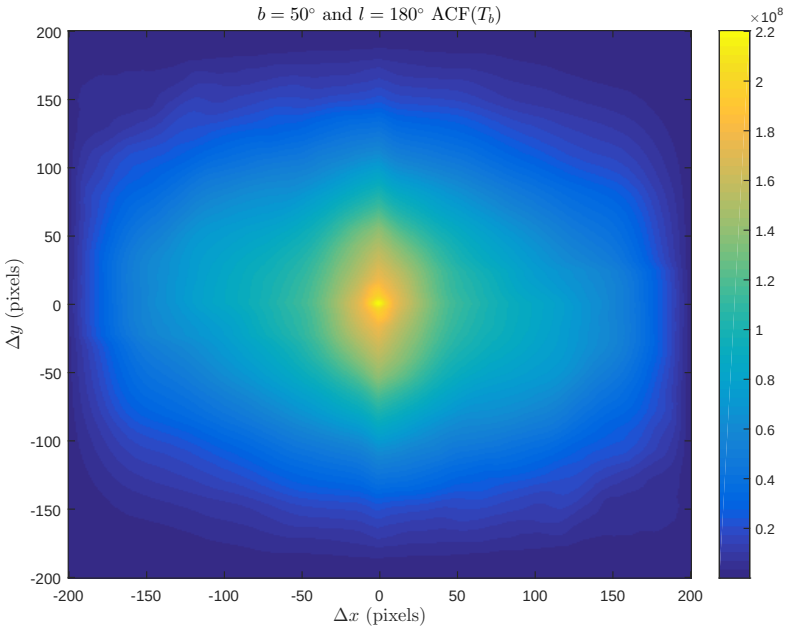

Figure B.34: ACF of T_b at $b = 50°$, $l = 180°$.

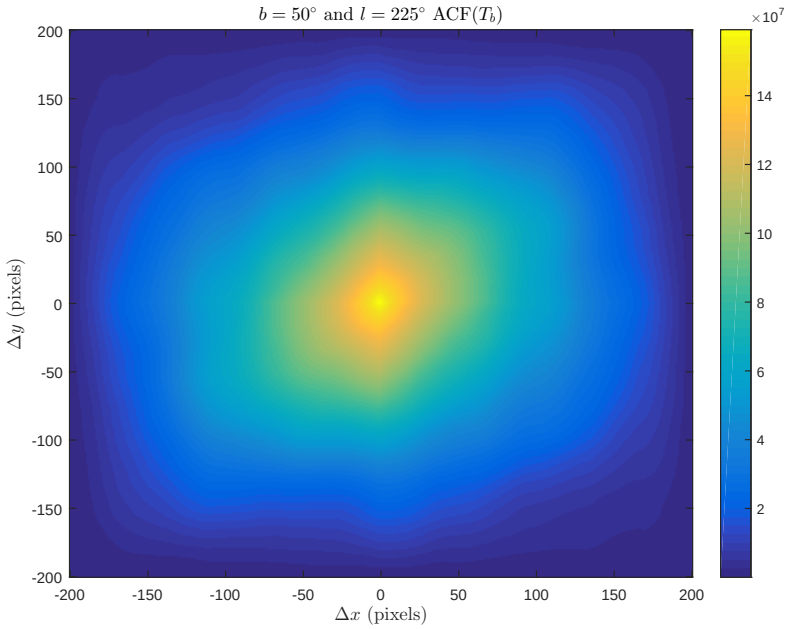

Figure B.35: ACF of T_b at $b = 50°$, $l = 225°$.

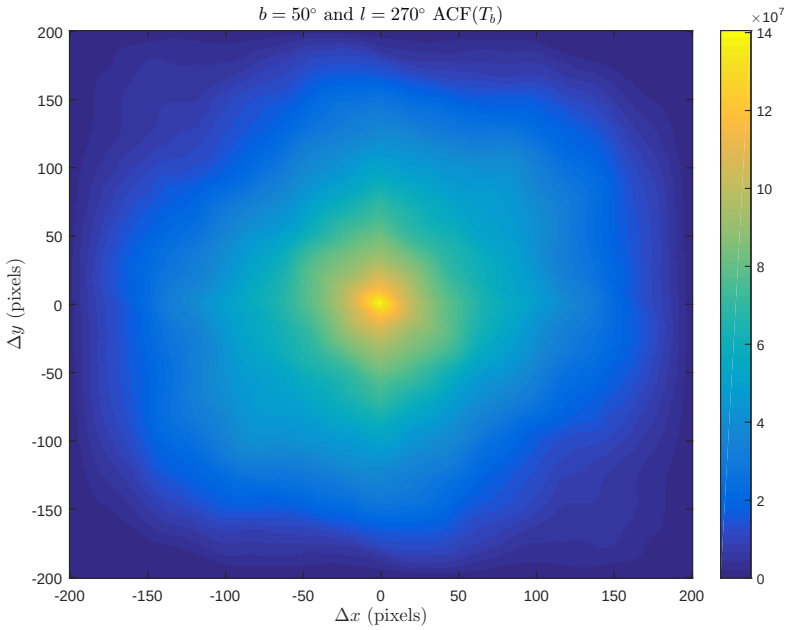

Figure B.36: ACF of T_b at $b = 50°$, $l = 270°$.

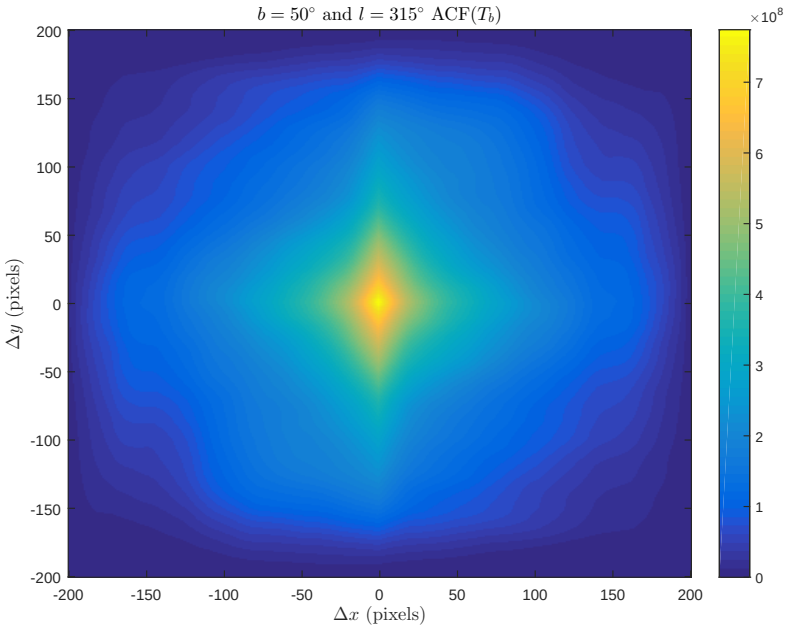

Figure B.37: ACF of T_b at $b = 50°$, $l = 315°$.

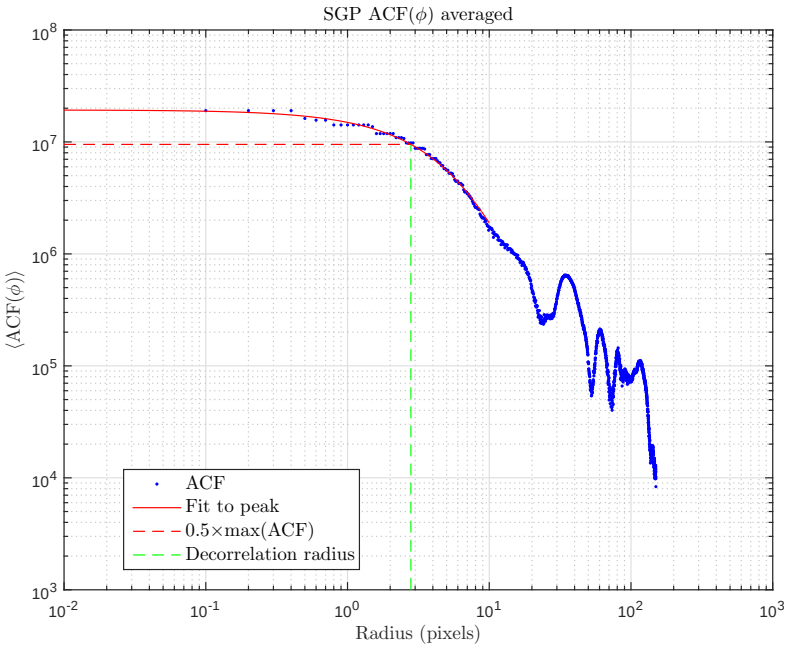

Figure B.38: Averaged ACF of Faraday depth in the SGP. Note negative values have been exlcuded from 'log-log' plot.

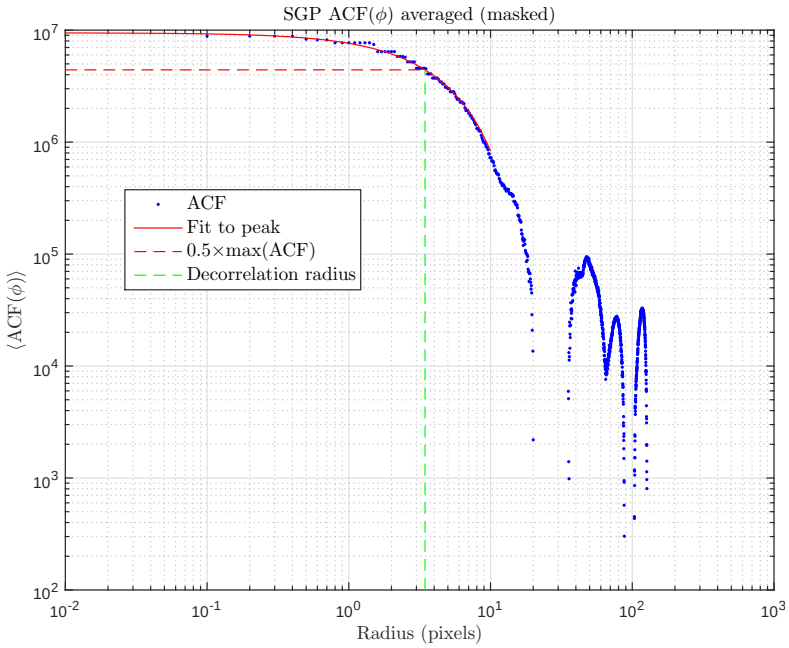

Figure B.39: Averaged ACF of Faraday depth in the SGP (masked). Note negative values have been exlcuded from 'log-log' plot.

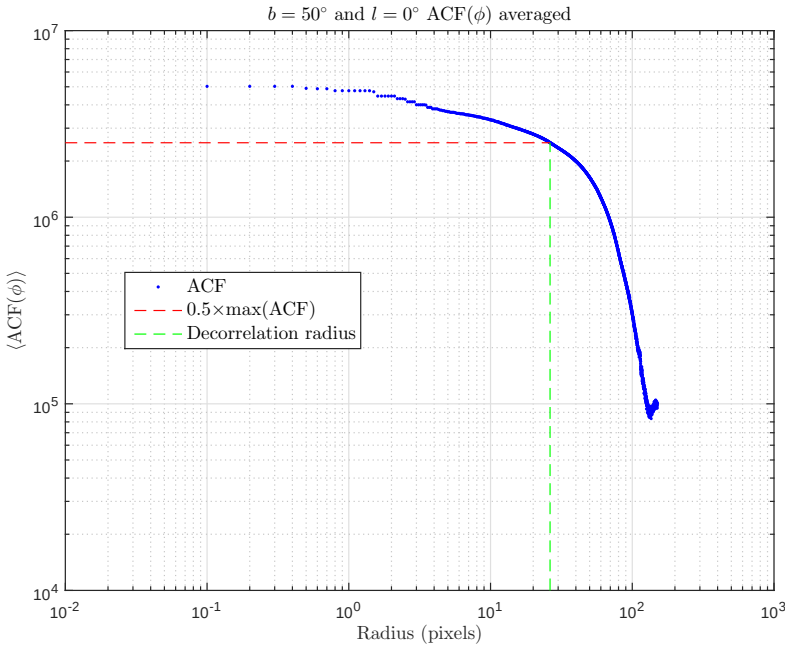

Figure B.40: Averaged ACF of Faraday depth at $b = 50°$, $l = 0°$. Note negative values have been exlcuded from 'log-log' plot.

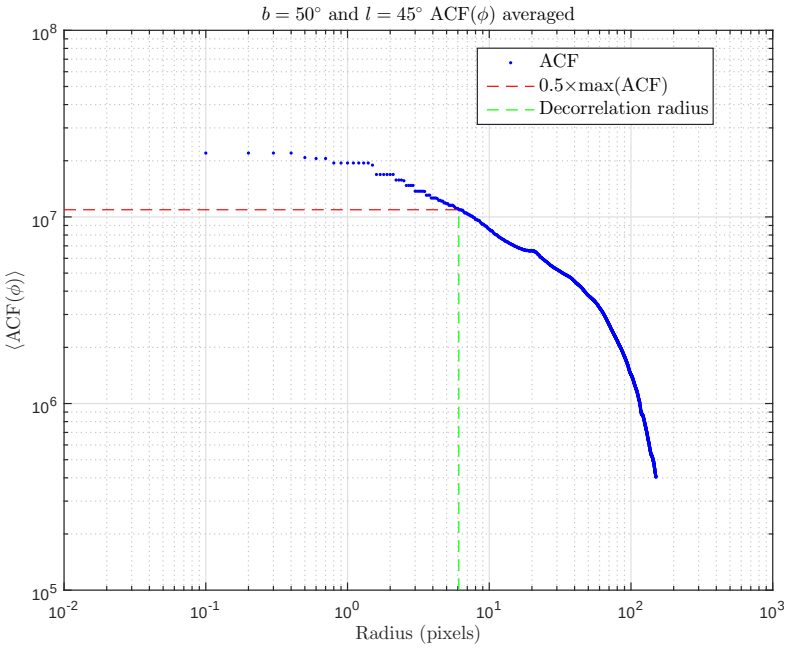

Figure B.41: Averaged ACF of Faraday depth at $b = 50°$, $l = 45°$. Note negative values have been exlcuded from 'log-log' plot.

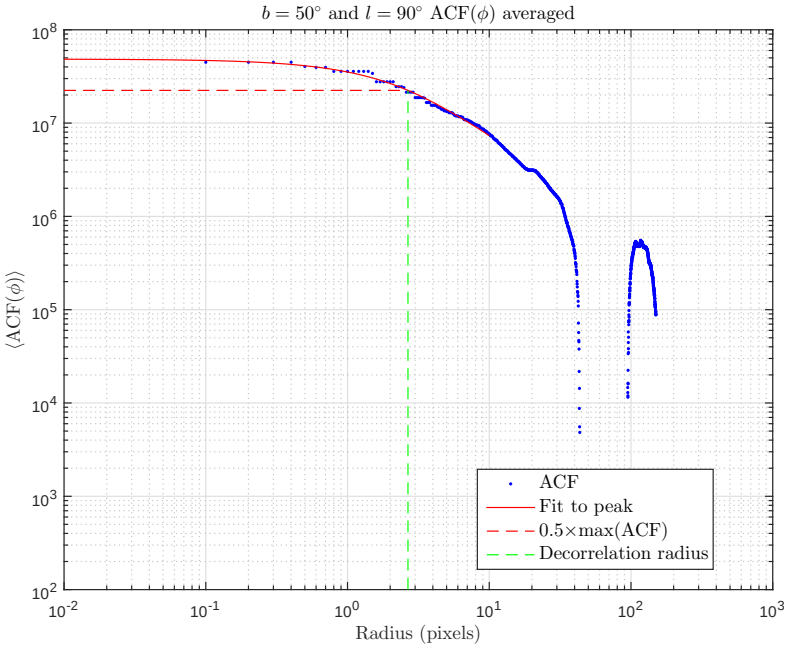

Figure B.42: Averaged ACF of Faraday depth at $b = 50°$, $l = 90°$. Note negative values have been exlcuded from 'log-log' plot.

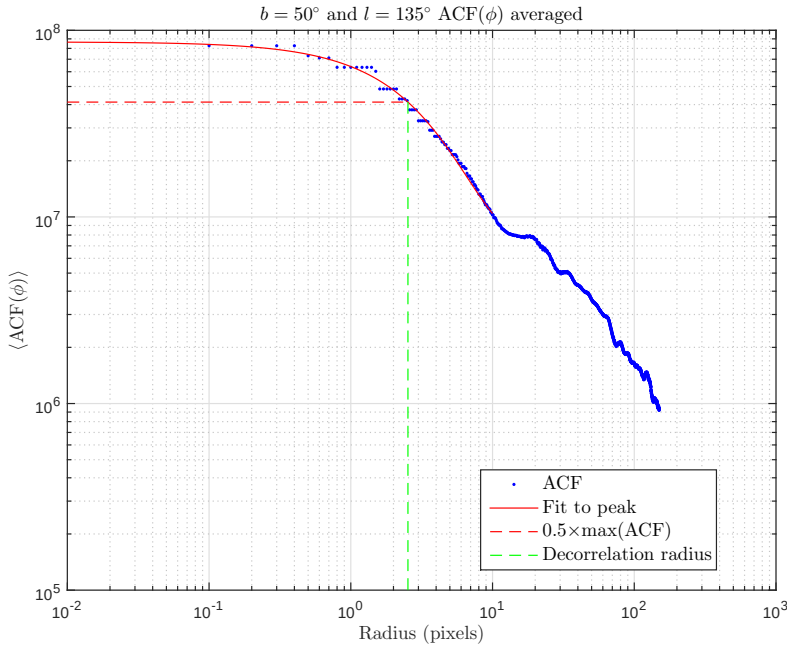

Figure B.43: Averaged ACF of Faraday depth at $b = 50°$, $l = 135°$. Note negative values have been exlcuded from 'log-log' plot.

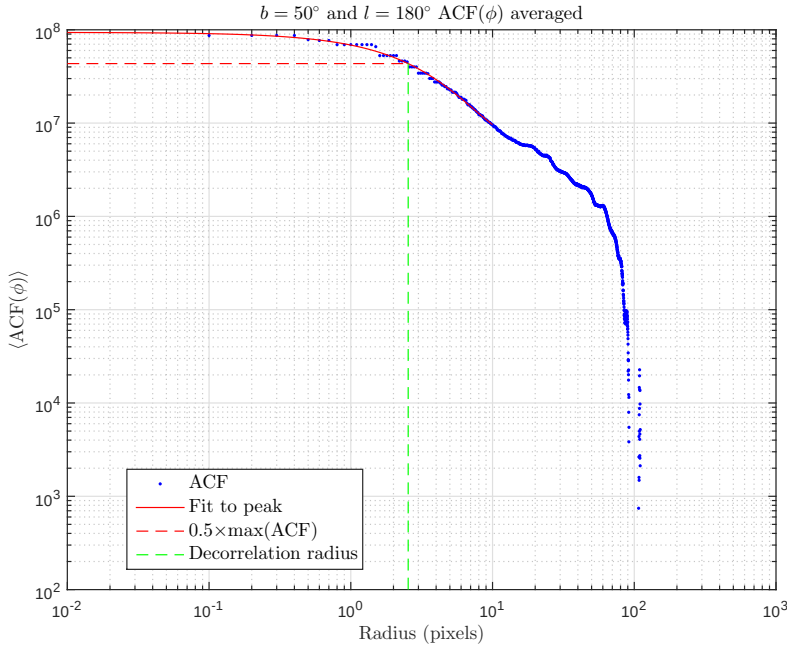

Figure B.44: Averaged ACF of Faraday depth at $b = 50°$, $l = 180°$. Note negative values have been exlcuded from 'log-log' plot.

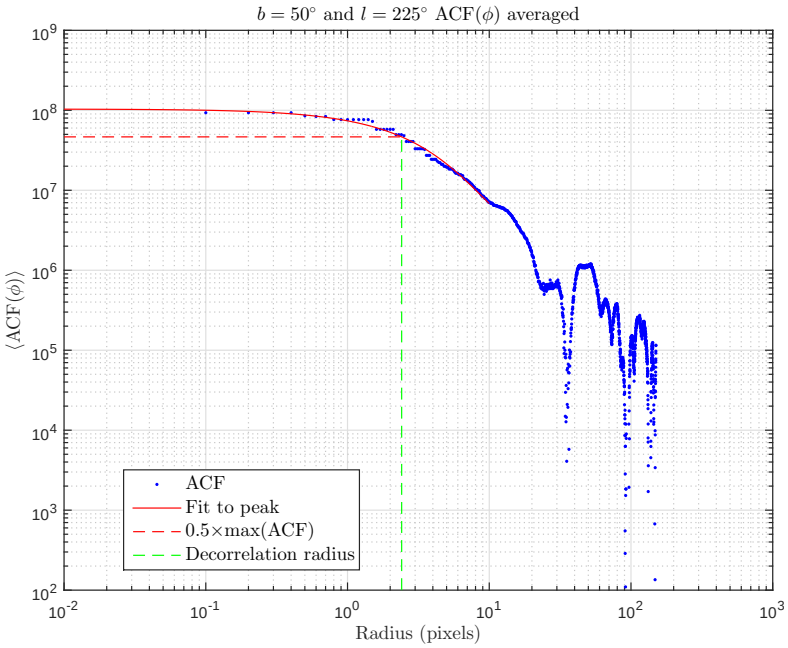

Figure B.45: Averaged ACF of Faraday depth at $b = 50°$, $l = 225°$. Note negative values have been exlcuded from 'log-log' plot.

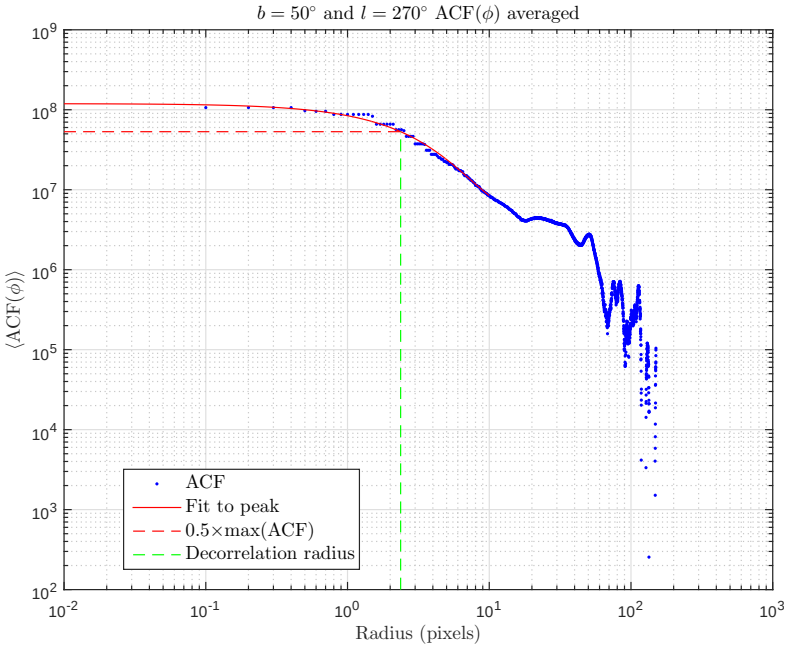

Figure B.46: Averaged ACF of Faraday depth at $b = 50°$, $l = 270°$. Note negative values have been exlcuded from 'log-log' plot.

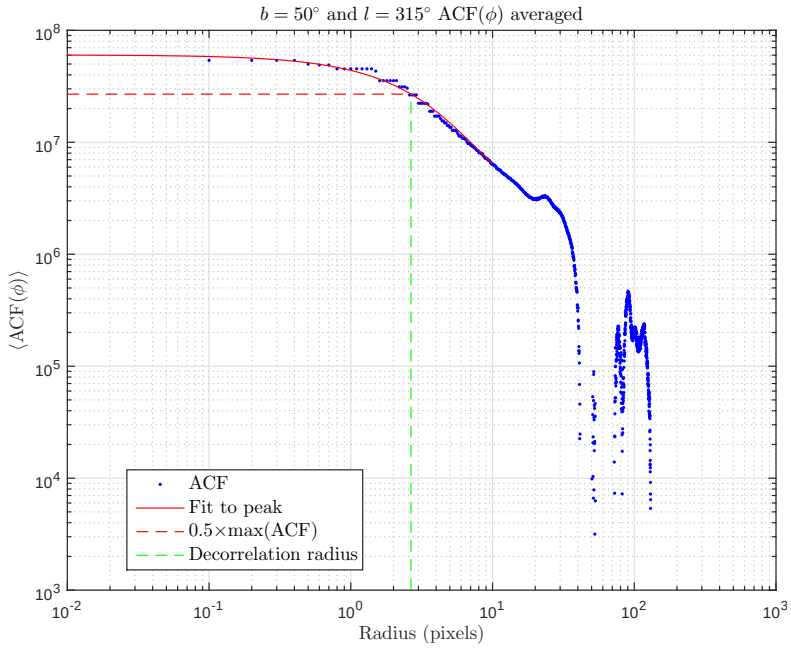

Figure B.47: Averaged ACF of Faraday depth at $b = 50°$, $l = 315°$. Note negative values have been exlcuded from 'log-log' plot.

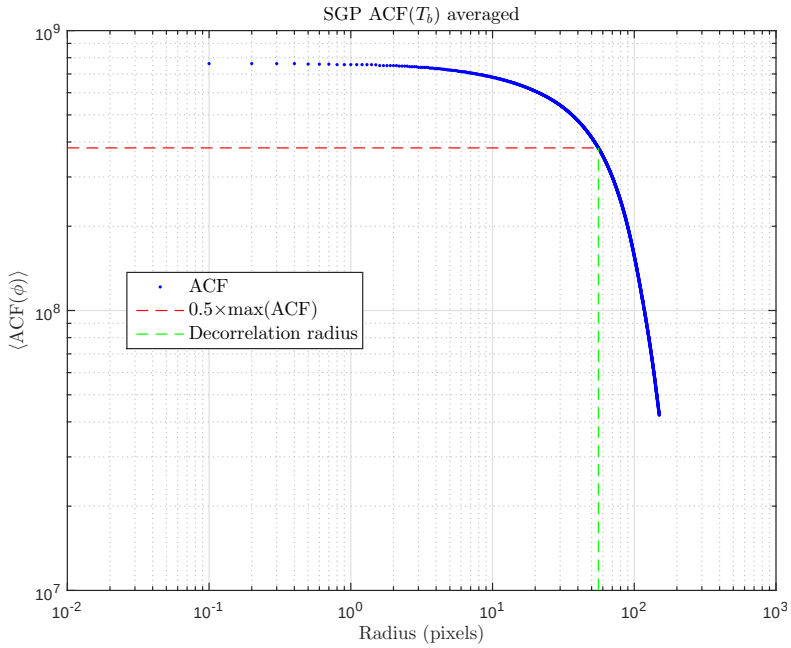

Figure B.48: Averaged ACF of polarised brightness temperature in the SGP. Note negative values have been exlcuded from 'log-log' plot.

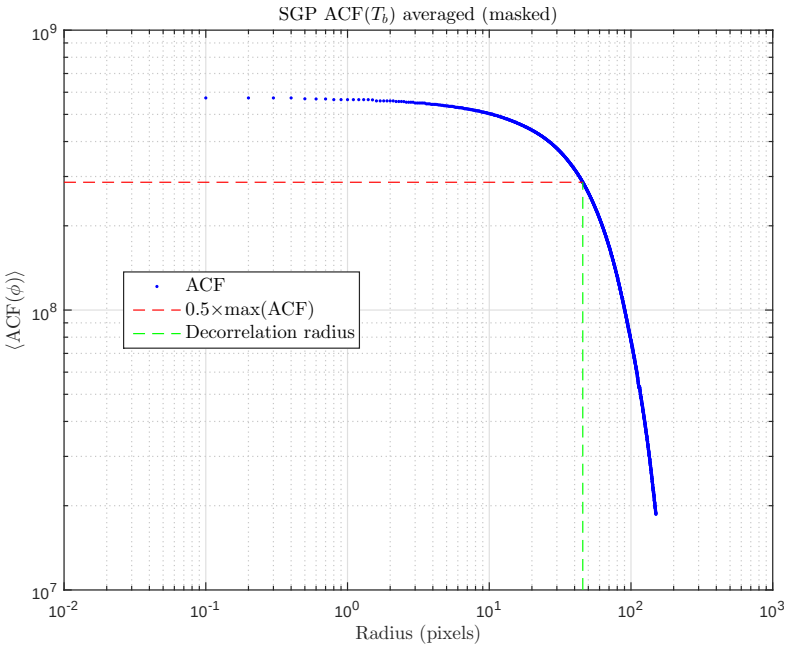

Figure B.49: Averaged ACF of polarised brightness temperature in the SGP (masked). Note negative values have been exlcuded from 'log-log' plot.

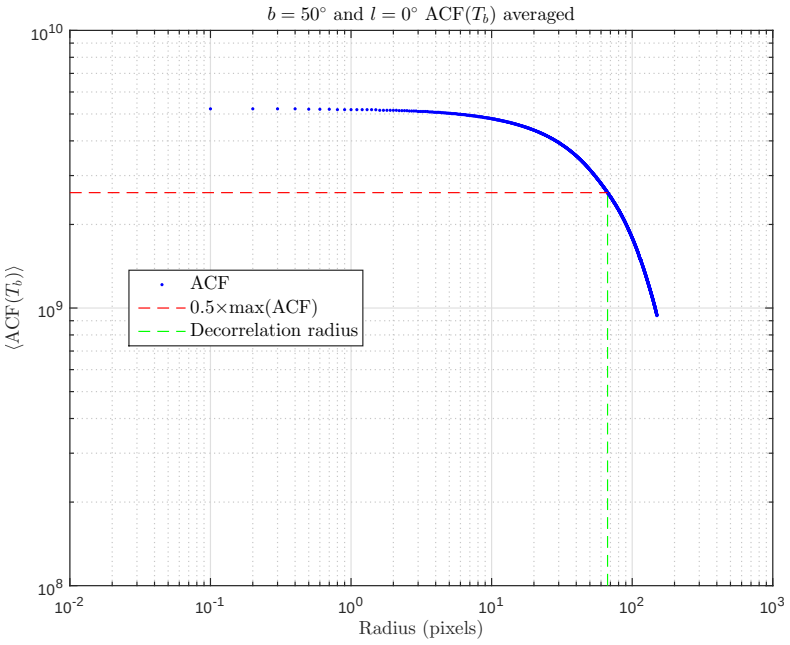

Figure B.50: Averaged ACF of T_b at $b = 50°$, $l = 0°$. Note negative values have been exlcuded from 'log-log' plot.

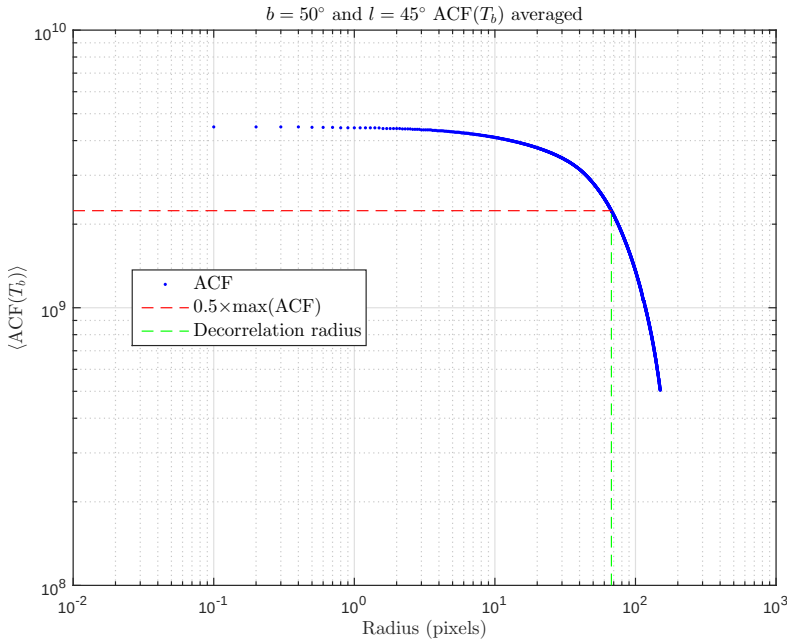

Figure B.51: Averaged ACF of T_b at $b = 50°$, $l = 45°$. Note negative values have been exlcuded from 'log-log' plot.

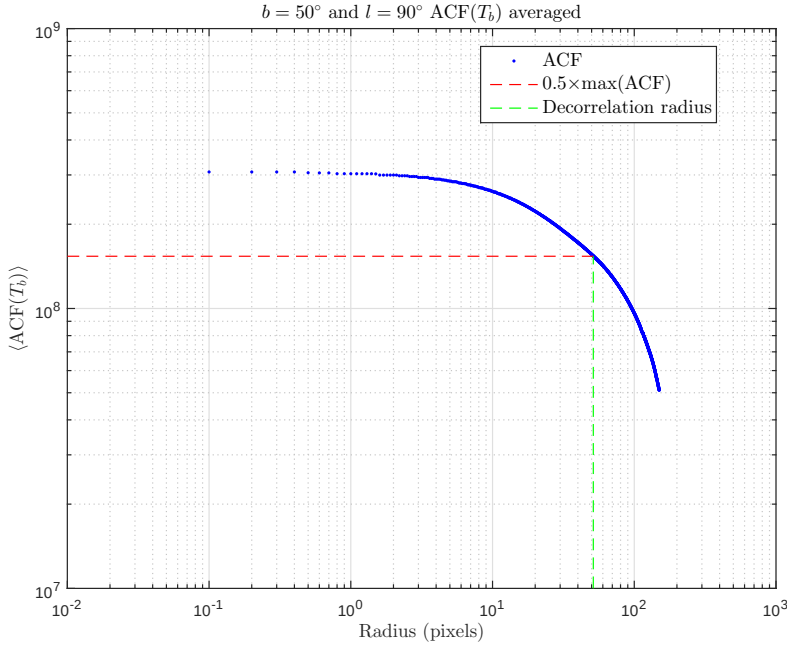

Figure B.52: Averaged ACF of T_b at $b = 50°$, $l = 90°$. Note negative values have been exlcuded from 'log-log' plot.

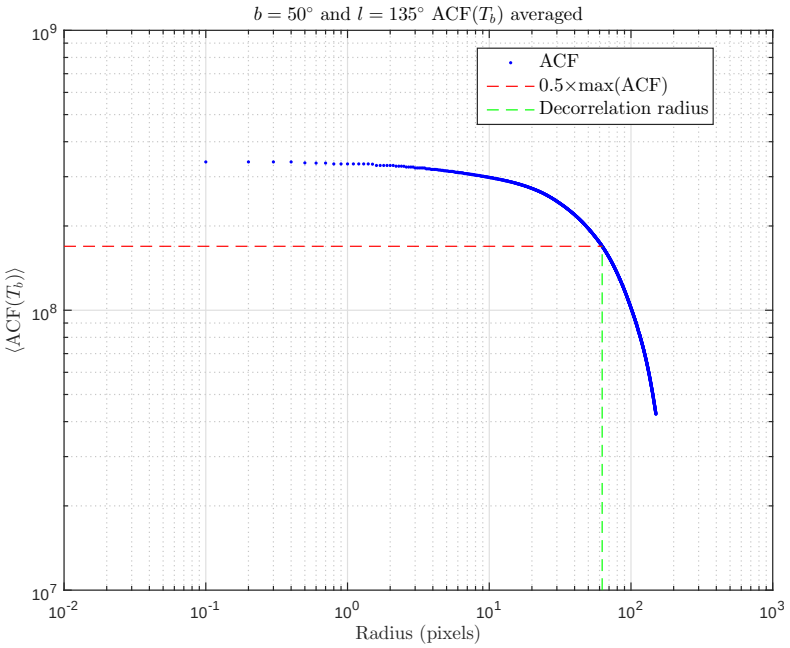

Figure B.53: Averaged ACF of T_b at $b = 50°$, $l = 135°$. Note negative values have been exlcuded from 'log-log' plot.

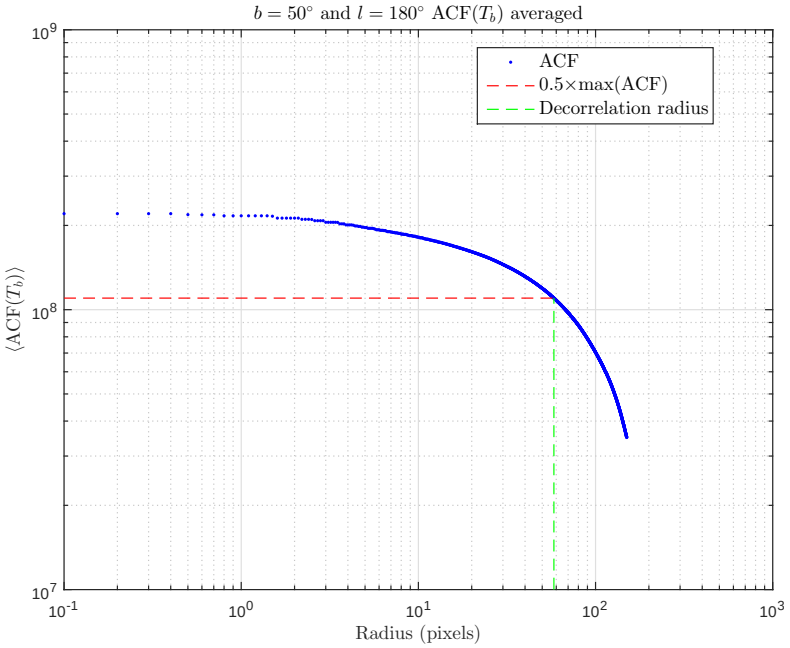

Figure B.54: Averaged ACF of T_b at $b = 50°$, $l = 180°$. Note negative values have been exlcuded from 'log-log' plot.

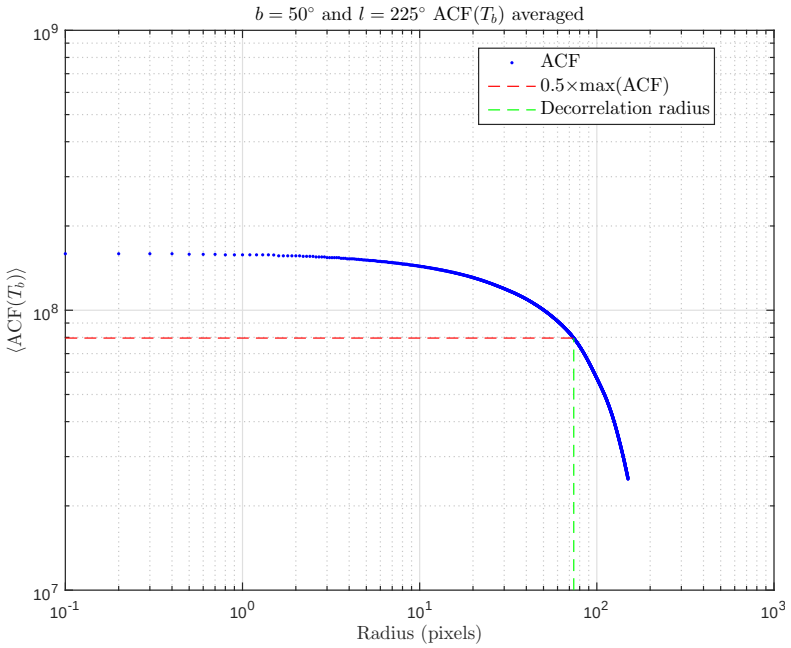

Figure B.55: Averaged ACF of T_b at $b = 50°$, $l = 225°$. Note negative values have been exlcuded from 'log-log' plot.

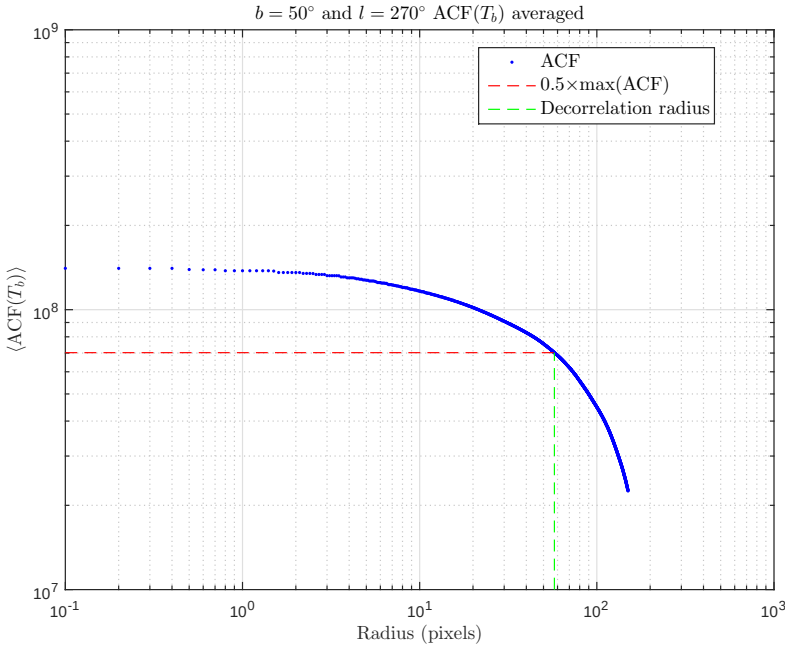

Figure B.56: Averaged ACF of T_b at $b = 50°$, $l = 270°$. Note negative values have been exlcuded from 'log-log' plot.

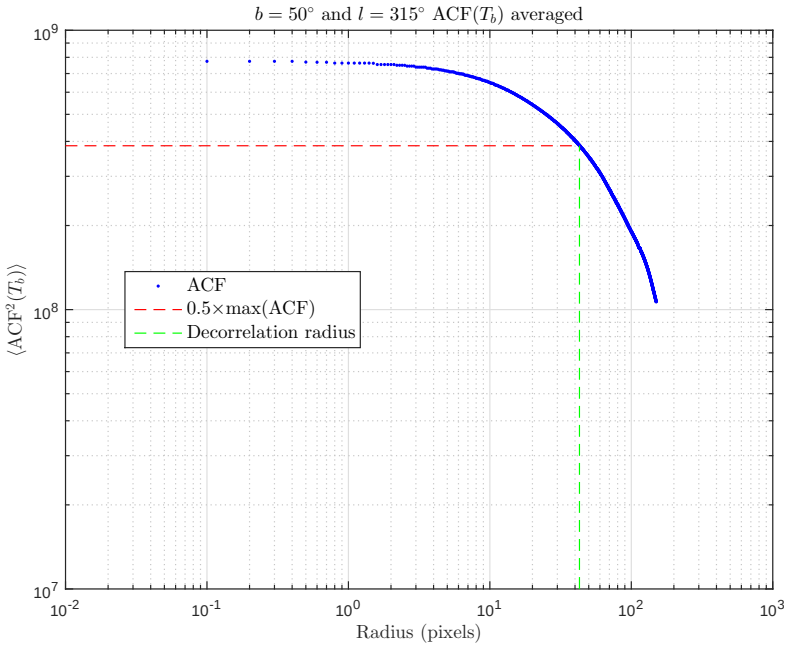

Figure B.57: Averaged ACF of T_b at $b = 50°$, $l = 315°$. Note negative values have been exlcuded from 'log-log' plot.

BIBLIOGRAPHY

R. Beck and R. Wielebinski. *Magnetic Fields in Galaxies*, page 641. 2013. doi: 10.1007/978-94-007-5612-0_13.

M. A. Brentjens and A. G. de Bruyn. Faraday rotation measure synthesis. *Astronomy and Astrophysics*, 441:1217–1228, October 2005. doi: 10.1051/0004-6361:20052990.

B. J. Burn. On the depolarization of discrete radio sources by Faraday dispersion. *Monthly Notices of the Royal Astronomical Society*, 133:67, 1966.

M. R. Calabretta and E. W. Greisen. Representations of celestial coordinates in FITS. *Astronomy and Astrophysics*, 395:1077–1122, December 2002. doi: 10.1051/0004-6361:20021327.

Wikimedia Commons. Diagram of stereographic projection onto the plane z=-1, drawn in inkscape, 2007. URL `https://en.wikipedia.org/wiki/File:Stereoprojnegone.svg`. File: *Stereoprojnegone.svg*.

J. J. Condon. Errors in Elliptical Gaussian FITS. *Publications of the Astronomical Society of the Pacific*, 109:166–172, February 1997. doi: 10.1086/133871.

J.J. Condon and S.M. Ransom. *Essential Radio Astronomy*. National Radio Astronomy Observatory, 2007.

A. Fletcher, R. Beck, A. Shukurov, E. M. Berkhuijsen, and C. Horellou. Magnetic fields and spiral arms in the galaxy M51. *Monthly Notices of the Royal Astronomical Society*, 412:2396–2416, April 2011. doi: 10.1111/j.1365-2966.2010.18065.x.

B. M. Gaensler, G. J. Madsen, S. Chatterjee, and S. A. Mao. The Vertical Structure of Warm Ionised Gas in the Milky Way. *Publications of the Astronomical Society of Australia*, 25:184–200, November 2008. doi: 10.1071/AS08004.

G Gbur. Faraday brings light and magnetism together (1845), 2009. URL `ttp://skullsinthestars.scientopia.org/2009/03/02/Faraday-brings-light-and-magnetism-together-1845/`.

Lisa Germany, Rob Proctor, Christopher Fluke, Amaya Gaztelu, Glen Mackie, Sarah Maddison, Alfred Lagos, Virginia Kilborn, and Matthew Bailes. Pulsar dispersion measure, 2015. URL `http://astronomy.swin.edu.au/cosmos/P/Pulsar+Dispersion+Measure`.

L. M. Haffner, R. J. Reynolds, G. J. Madsen, S. L. Tufte, K. P. Jaehnig, J. P. Percival, and N. R. Hausen. The Wisconsin Hα Mapper Northern Sky Survey. In *American Astronomical Society Meeting Abstracts*, volume 33 of *Bulletin of the American Astronomical Society*, page 1389, December 2001.

Martin Harwit. *Astrophysical Concepts*. Springer-Verlag New York, 4 edition, 2006.

M. Haverkorn and V. Heesen. Magnetic Fields in Galactic Haloes. *Space Science Reviews*, 166:133–144, May 2012. doi: 10.1007/s11214-011-9757-0.

A. S. Hill, T. L. Landecker, E. Carretti, K. A. Douglas, X. Sun, B. M. Gaensler, S. A. Mao, N. M. McClure-Griffiths, M. Wolleben, M. Haverkorn, and D. Schnitzeler. New perspective on the Fan Region: Polarized synchrotron emission tracing Galactic structure beyond the Perseus Arm. In *American Astronomical Society Meeting Abstracts*, volume 225 of *American Astronomical Society Meeting Abstracts*, page 127.05, January 2015.

G. Johnson. *The Ten Most Beautiful Experiments*. New York: Alfred A. Knopf, 2008.

J.D. Kraus. *Radio Astronomy*. McGraw-Hill, 1 edition, 1966.

Petar Maksimovic. Introduction to error analysis. Lecture Notes, February 2003.

S. A. Mao, B. M. Gaensler, M. Haverkorn, E. G. Zweibel, G. J. Madsen, N. M. McClure-Griffiths, A. Shukurov, and P. P. Kronberg. A Survey of Extragalactic Faraday Rotation at High Galactic Latitude: The Vertical Magnetic Field of the Milky Way Toward the Galactic Poles. *The Astrophysical Journal*, 714:1170–1186, May 2010. doi: 10.1088/0004-637X/714/2/1170.

S. A. Mao, N. M. McClure-Griffiths, B. M. Gaensler, J. C. Brown, C. L. van Eck, M. Haverkorn, P. P. Kronberg, J. M. Stil, A. Shukurov, and A. R. Taylor. New Constraints on the Galactic Halo Magnetic Field Using Rotation Measures of Extragalactic Sources toward the Outer Galaxy. *The Astrophysical Journal*, 755:21, August 2012. doi: 10.1088/0004-637X/755/1/21.

Pratap Misra and Per Enge. *Global Positioning System: Signals, Measurements and Performance Second Edition*. Ganga-Jumuna Press, 2011.

N. Oppermann, H. Junklewitz, M. Greiner, T. A. Enßlin, T. Akahori, E. Carretti, B. M. Gaensler, A. Goobar, L. Harvey-Smith, M. Johnston-Hollitt, L. Pratley, D. H. F. M. Schnitzeler, J. M. Stil, and V. Vacca. Estimating extragalactic Faraday rotation. *Astronomy and Astrophysics*, 575:A118, March 2015. doi: 10.1051/0004-6361/201423995.

R. J. Reynolds. Line integrals of N_E and $(n_{E)-squared}$ at high Galactic latitude. *Astrophysical Journal, Letters*, 372:L17–L20, May 1991. doi: 10.1086/186013.

X. H. Sun, T. L. Landecker, B. M. Gaensler, E. Carretti, W. Reich, J. P. Leahy, N. M. McClure-Griffiths, R. M. Crocker, M. Wolleben, M. Haverkorn, K. A. Douglas, and A. D. Gray. Faraday Tomography of the North Polar Spur: Constraints on the Distance to the Spur and on the Magnetic Field of the Galaxy. *The Astrophysical Journal*, 811:40, September 2015. doi: 10.1088/0004-637X/811/1/40.

Xiahui Sun. Possum report #61: Extraction of polarisation parameters from a "simple" faraday spectrum. Technical report, The University of Sydney, 2013.

A. R. Taylor, J. M. Stil, and C. Sunstrum. A rotation measure image of the sky. *The Astrophysical Journal*, 702(2):1230, 2009. URL `http://stacks.iop.org/0004-637X/702/i=2/a=1230`.

M. Wolleben, T. L. Landecker, E. Carretti, J. M. Dickey, A. Fletcher, B. M. Gaensler, J. L. Han, M. Haverkorn, J. P. Leahy, N. M. McClure-Griffiths, D. McConnell, W. Reich, and A. R. Taylor. GMIMS: the Global Magneto-Ionic Medium Survey. In K. G. Strassmeier, A. G. Kosovichev, and J. E. Beckman, editors, *IAU Symposium*, volume 259 of *IAU Symposium*, pages 89–90, April 2009. doi: 10.1017/S1743921309030117.

M. Wolleben, T. L. Landecker, G. J. Hovey, R. Messing, O. S. Davison, N. L. House, K. H. M. S. Somaratne, and I. Tashev. Rotation Measure Synthesis of Galactic Polarized Emission with the DRAO 26-m Telescope. *The Astronomical Journal*, 139: 1681–1690, April 2010. doi: 10.1088/0004-6256/139/4/1681.